NANOSTRUCTURED SEMICONDUCTORS FOR THERMOELECTRIC ENERGY CONVERSION: SYNTHESIS AND TRANSPORT PROPERTIES

by

Pranati Sahoo

A dissertation submitted in partial fulfillment
of the requirements for the degree of
Doctor of Philosophy
(Materials Science and Engineering)
in The University of Michigan
2013

Doctoral Committee:

Assistant Professor Pierre Ferdinand Poudeu-Poudeu, Chair
Professor John W. Halloran
Assistant Professor Emmanouil Kioupakis
Professor Ctirad Uher

© Pranati Sahoo 2013
All rights reserved

To my family
For their love and support

ACKNOWLEDGEMENTS

I would like to thank my advisor, Prof. Ferdinand Poudeu for his guidance and support throughout my studies at the University of Michigan and University of New Orleans. It would not have been possible without his constant encouragement, enthusiasm, patience, motivation, and immense knowledge. His guidance helped me in all the time of research. I could not have imagined having a better advisor and mentor for my PhD study. I would also like to thank Prof. Ctirad Uher, Prof. John W. Halloran and Prof. Emmanouil Kioupakis for their valuable discussions and insightful suggestions.

I am fortunate to avail the opportunity of collaborations with Prof. Uher and his group for allowing me to use his lab equipment and helping me with measurements. His suggestions and ideas greatly influenced the way I think about the innovative approaches for thermoelectric material development. I am also thankful to Prof. Xiaoqing Pan and his group for assisting me with the microscopic measurements. My sincere thanks also go to Prof. Kevin Stokes and Prof John Wiley from University of New Orleans for enlightening me with the first glance of research.

I would remiss if I did not thank all my fellow students in Prof. Poudeu's research group for their help and cooperation. In particular, I would like to thank the past post doctoral fellows in our group , Dr Nathan Takas, Dr Julien Makongo , Dr Sanjaya Ranmohotti and Dr Dinesh Misra for helping me with designing the experiments and analyzing the results. I would also like to thank my group members Yuanfeng Liu, Honore Djieutedjeu, Alan Olvera , Erica Chen ,Juan Lopez for their constant encouragement and eagerness to help me through these

years. Finally, my deepest gratitude to my family for their understanding, inspiration & endless love throughout my life, without whom it wouldn't have been possible.

TABLE OF CONTENTS

LIST OF FIGURES

LIST OF TABLES

ABSTRACT

Increasing energy demands and decreasing natural energy resources have sparked search for alternative clean and renewable energy sources. For instance, currently there is a tremendous interest in thermoelectric and photovoltaic solar energy production technologies. Half-Heusler (HH) alloys are among the most popular material systems presently under widespread investigations for high temperature thermoelectric energy conversion. Approaches to increase the thermoelectric figure of merit (ZT) of HH range from (1) chemical substitution of atoms with different masses within the same atomic position in the crystal structure to optimize carrier concentration and enhance phonon scattering via mass fluctuation and (2) embedding secondary phonon scattering centers in the matrix (nanostructuring) to further reduce thermal conductivity.

This work focuses on three material systems. The first part describes the synthesis and properties (thermal conductivity, electrical conductivity, magnetic) of various oxide nanostructures (NiO, Co_3O_4) which were subsequently used as inclusion phases in a HH matrix to reduce the thermal conductivity. Detailed reviews of the past efforts along with the current effort to optimize synthetic routes are presented. The effects of the synthesis conditions on the thermoelectric properties of compacted pellets of NiO and Co_3O_4 are also discussed. The second part of the work discusses the development of synthetic strategies for the fabrication of p-type and n-type bulk nanostructured thermoelectric materials made of a half-Heusler matrix based on (Ti,Hf)CoSb, containing nanostructures with full-Heusler (FH) compositions and structures coherently embedded inside the half-Heusler matrix. The role of the nanostructures in the

regulation of phonon and charge carrier transports within the half-heusler matrix is extensively discussed by combining transport data and electron microscopy images. It was found that the FH nanoinclusions form staggered heterojunctions with a valence band (VB) offset energy at the HH/FH phase boundaries. The resulting energy barrier discriminates existing holes with respect to their energy by trapping low energy holes, while promoting the transport of high energy holes through the VB of the FH-quantum dots. This "carrier culling" results in surprisingly large increase in the mobility and the effective mass of high energy holes contributing to electronic conduction. The simultaneous reduction in the density and the increase in the effective mass of holes resulted in large enhancements of the thermopower, whereas the increase in the mobility minimizes the drop in the electrical conductivity. In the third part, the application of this concept of nanostructuring on the copper selenide material system is described. Various synthetic approaches such as liquid assisted solid-state reaction and mechanical alloying are utilized for the fabrication of copper selenide compositions. We found that the mechanical alloying clearly decreases the thermal conductivity of the composition as well increases the Seebeck due to decrease in carrier concentrations.

Chapter 1

INTRODUCTION

1.1 Motivation and outline of the thesis

The current research is focused on the development of various novel thermoelectric materials which can have a high potential for a large scale energy conversion application. The concept of "nanostructuring" used in this research could open plenty of opportunities to tailor the thermal and electronic transport behavior of the f base materials resulting in the enhancement of the thermoelectric performances. An efficient thermoelectric device mostly relies on the materials with high electrical conductivity (σ), high Seebeck coefficient (S) and low lattice thermal conductivity (κ) for a steady solid state energy conversion. Simultaneous optimization of all these properties to have a high thermoelectric figure of merit ($ZT = TS^2\sigma/\kappa$) has proven to be a real challenge.

Several conventional methods have been used to synthesize thermoelectric materials with control over the thermal transport properties (lattice thermal conductivity, $\kappa_{lattice}$) and the electronic transport properties (thermopower, S; electrical conductivity, σ) of the bulk semiconductors. There are also interest in developing new strategies to address these issues by tuning the phonon scattering via nanostructuring, and optimizing the concentration (n) and

mobility (μ) of charge carriers via doping and/or substitutional chemistry. Although, the exploration of these approaches helped to improve the ZT significantly, these improvements mostly result from large reductions in κ rather than an enhancement in the PF. Understanding how to enhance the power factor using nanostructuring needs further exploration. In the current research, the concept of quantum confinement and the mechanism by which nanostructuring can be used to enhance the PF of thermoelectric materials along with the reduction in the thermal conductivity, has been studied extensively using different class of compounds.

The subsequent sections in chapter 1 give a brief introduction about various concepts and factors affecting the material's thermoelectric performances. This also includes a brief literature review about the advances in half- Heusler alloy as a high temperature thermoelectric material. The last section reflects the application of the technique of nanostructuring on Cu-Se based low temperature thermoelectric materials.

Chapter 2 opens with the study large scale synthesis of high purity; nanometer sized surfactant-free nickel oxide (NiO) particles using a solution combustion method. The aim was to use these nanostructures as additional phonon scattering centers to further reduce the thermal conductivity of any half-Heusler material.. Furthermore, the effect of the synthesis temperature on the particle size and thermal conductivities are discussed.

Chapter 3 details the importance of mixed valence Cobalt oxide(Co_3O_4), followed by the experimental part explaining the synthesis of surfactant-free Co_3O_4 nanostructures with various particles size ranges via the solution combustion method. Various properties like structural, optical, electronic, magnetic and thermoelectric the resulting products are also investigated.

Chapter 4 reports on the investigation of in situ growth of nanostructure in a bulk semiconducting half-Heusler matrix of the p-type $Ti_{0.5}Hf_{0.5}Co_{1+z}Sb_{09}Sn_{0.1}$ ($0 \leq z \leq 0.1$) and n – type $Ti_{0.5}Hf_{0.5}Ni_{1+z}Sn_{0.975}Sb_{0.025}$ ($0 \leq z \leq 0.1$) phases. The effects of nanostructuring on their thermoelectric properties are discussed.

Chapter 5 explores the effect of mechanical alloying (high energy ball milling) on the thermoelectric properties of an n-type half Heusler alloy. The modifications in the thermal and electronic transport caused by the mechanical alloying are presented.

Chapter 6 introduces the nanostructuring approach in the Copper Selenide (Cu-Se) system which is also a potential Chalcogenides based thermoelectric material. Effects of different synthetic routes on its thermoelectric properties are compared.

Chapter 7 concludes the dissertation with the summary of the current attempts and the possible future studies with emphasis on the exploration of reaction conditions to obtain single phase of the different composites and to optimize the properties of the material in a better way.

1.2 Thermoelectric Effects

1.2.1. Brief history on thermoelectricity

The increased global energy needs, climatic changes and continual depletion of energy resources have the triggered the widespread enthusiasm in researching renewable energy systems. Gradually, the world is coming under the threat of energy scarcity with the continual increase in world's population and subsequent decrease in the fossil fuel supplies. To satisfy the need of energy, technologies and materials which can provide sustainable supply of energy to the world's population must be developed. Thermoelectricity is the phenomenon by virtue of which waste

heat can be converted to electrical energy. Solid state energy conversion devices made of advanced thermoelectric materials are being considered as potential candidate for a wide range of energy applications. Thermoelectric devices can be used as heat pumps using Peltier effect (Refrigeration) or as heat to electricity converter using Seebeck effect (power generation) as shown in Fig.1.1. Both systems need electrons and holes as the charge carrier i.e. n-type and p-type materials respectively to build a working device as indicated in Figure 1.2[2]. In order to create thermoelectric devices with high energy conversion efficiency, both n-type and p-type materials with large dimensionless figure of merit, $ZT=S^2\sigma T/\kappa$, (where S is the thermopower, σ is the electrical conductivity, κ is the thermal conductivity and T is the absolute temperature) within the temperature range of interest must be identified.[3-15]

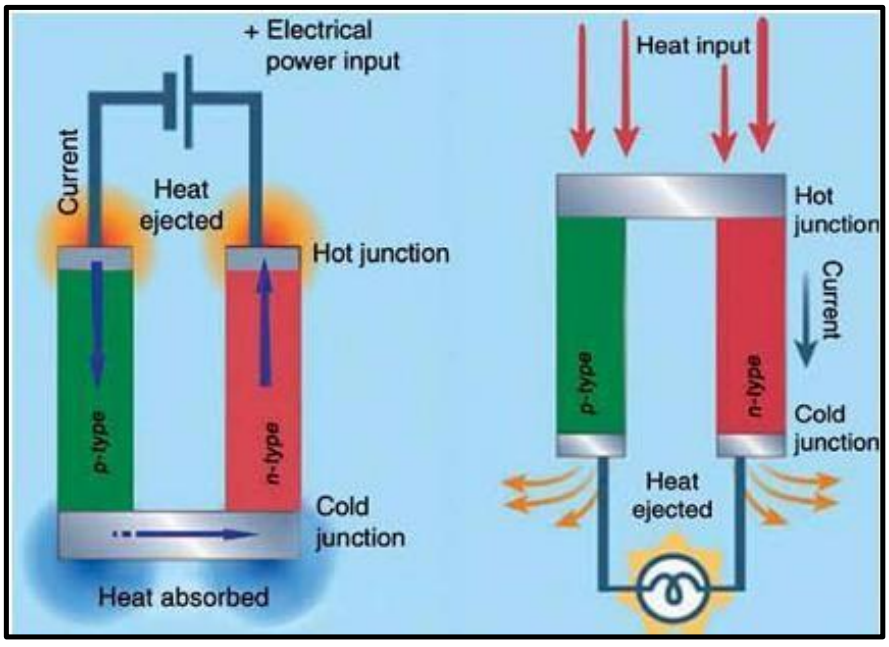

Figure 1 1 : Representation of the Peltier (left) and the Seebeck (right) effect.

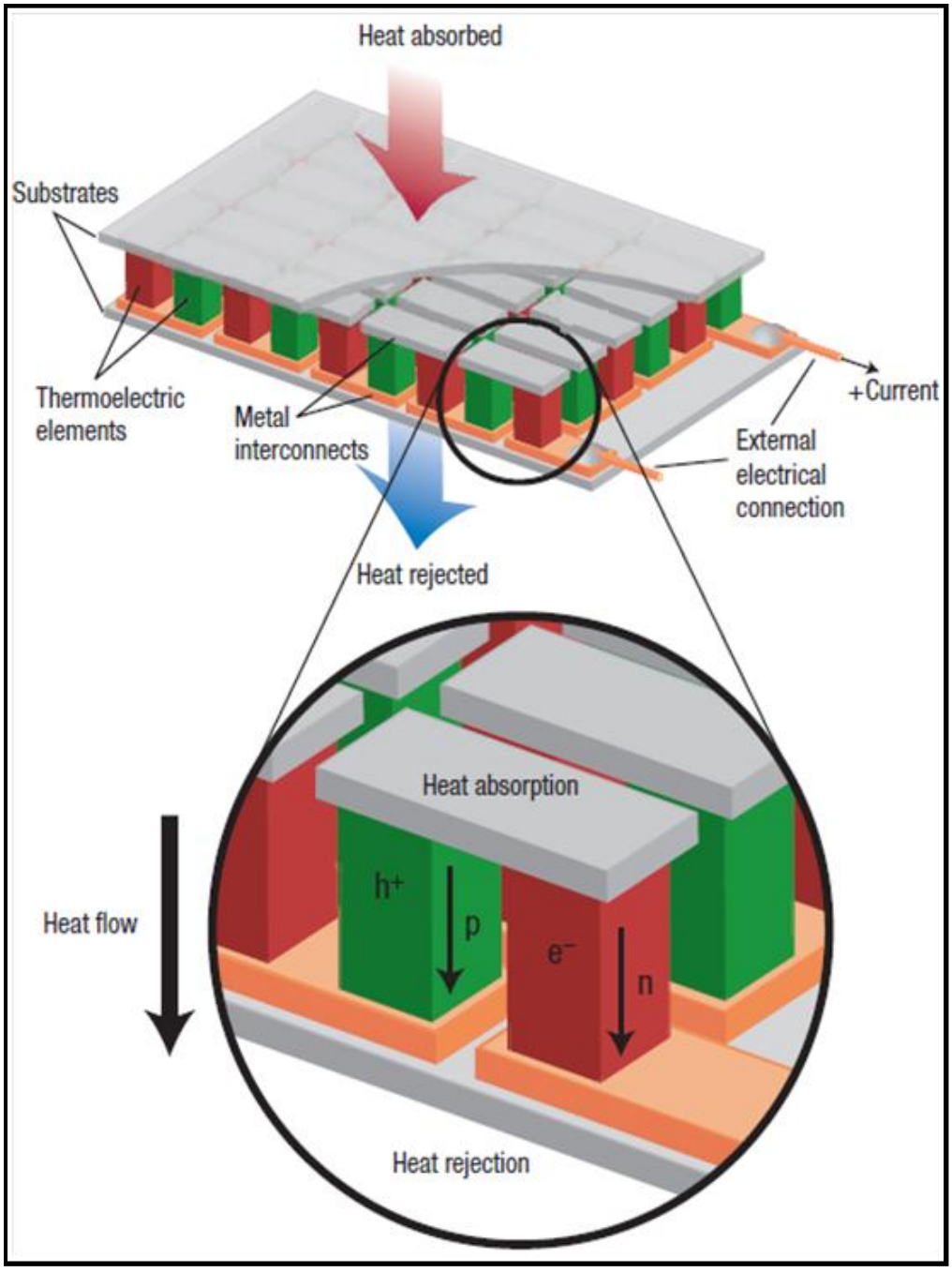

Figure1.2 : A Thermoelectric module[1].

Several thermoelectric materials have already proven themselves as suitable materials which could lead to substantial energy savings in various automobiles[16],electronic devices[17] and photovoltaic cells [18]. However, these materials need to have high performance ($ZT \geq 3$)[19] to be able to replace current mechanical heat engine systems. Several attempts have been made to hit the high performance target. Some of these approaches are currently being used in various devices, while some are still good only at laboratory grade[11,19-21]. As there is a great interdependence between the electronic and thermal parameters of the material, managing them to derive the desirable ZT (figure of merit) is quite difficult. However several approaches have been made to catch up with these inherent material behaviors. As the ZT inversely depends on the thermal conductivity, relatively high κ is one of the major roadblocks. This is typically dealt with by reducing the lattice thermal conduction through phonon scattering. This improved phonon scattering can be achieved by various pathways like substitutions and insertion of nanostructures [5,22-25]. The concept of nanostructuring has shown effective development in this respect as the quantum confinement of charge carriers in low dimensional structures within a given matrix is believed to increase the ZT of the composite drastically not only by reducing the thermal conductivities but also through a large enhancement of the power factor ($PF = \sigma \cdot S^2$) [26-28]. But the basic mechanism behind the nanostructuring effect which can explain how it affects the overall performances is not yet well studied. Several materials such as the skutterudites [29-31], Clathrates [32,33], Complex chalcogenides [34,35] and half Heusler alloys [36-38] are being studied as promising thermoelectric materials.

1.2.1. Recent developments on half-Heusler alloys as a high temperature thermoelectric material

Half-Heusler (HH) alloys with a valence electron count (VEC) of 18 have demonstrated excellent potential as materials for high temperature power generation, mainly because of their large thermopower and moderately high electrical conductivit[12]. HH alloys represent a fascinating large class of intermetallic phases with general composition TMX (T and M are transition metal or rare-earth metals and X is a main-group element) and crystallize in the MgAgAs structure type (space group: F-43m). Their structure can be described as consisting of four interpenetrating fcc (face-centered cubic) sublattices of T, M and X atoms occupying the crystallographic positions (0,0,0), (1/4, 1/4, 1/4) and (1/2, 1/2,1/2), respectively, whereas the fourth (3/4, 3/4, 3/4) position is vacant [39,40]. Upon filling the empty site, (3/4, 3/4, 3/4), within the structure of a HH (TMX) with an additional M atom, one directly generates the related ternary full-Heusler (FH) phase with general composition TM_2X (Fig1.3)[41].

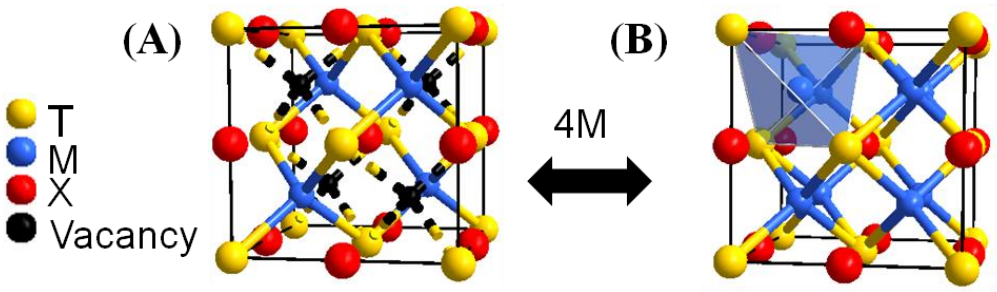

Figure 1. 3 : Comparison of the half-Heusler and full-Heusler crystal structures. (A) half-Heusler alloys (TMX) crystallize in the faced centered cubic (fcc) MgAgAs structure type (space group: F-43m) with half of the tetrahedral position vacant. Upon filling the vacant tetrahedral position with an additional M element, the corresponding full-Heusler phase (TM_2X) crystallizing in the cubic $MnCu_2Al$ structure-type (SG: *Fm*-3*m*) is obtained (B).

This spontaneous and reversible change in the crystal symmetry upon varying the chemical composition makes the HH and FH compounds, two distinct classes of structurally

related materials exhibiting dissimilar physical and chemical properties specific to each class [41-62]. Although, these fascinating two families of compounds have been treated separately over the past several decades, the ability to interchange between the HH and FH structure upon addition or removal of M atoms (at the (3/4, 3/4, 3/4) site) enables the atomic-scale manipulation of the properties (chemical, physical, mechanical, electrical, optical etc.) of one material by the other. Half-Heusler (HH) alloys play an important role in the search for high efficiency thermoelectric materials because of their moderate thermopower and electrical resistivity [47,54]. In addition, half-Heusler phases are chemically and thermally stable (melting above 1470K with almost no sublimation at temperatures below 1270K); they are easy to prepare in large scale quantities using conventional solid state synthesis techniques. They also involve cheap, abundant, lightweight and environmentally friendly elements. These advantages make HH materials suitable for large scale utilization in high temperature energy conversion devices.

1.2.2. Recent developments on Chalcogenides Cu-Se system as a low temperature thermoelectric material

Recently explored $CuSe_{2-x}$ system has shown revolutionary high ZT (figure of merit), which broadens up its scope as a potential thermoelectric material. In spite of their simple chemical formula, they bear quite complex atomic arrangements. The system mostly exhibits two phases, a low temperature α-phase predominantly having a tetragonal or monoclinic structure and a high-temperature β-phase which is having a stable cubic phase[63,64]. Despite of a fixed crystal base

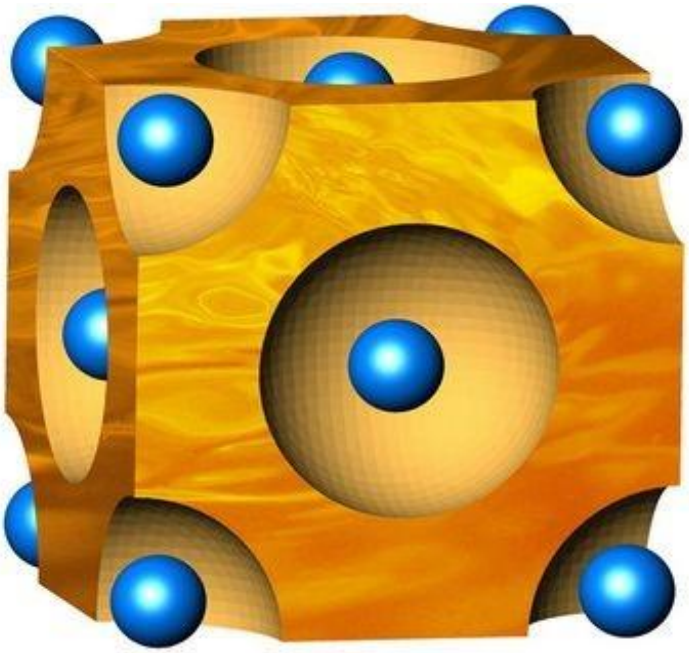

Figure 1.4 : (Copper Selenium);The blue spheres represent selenium atoms forming a crystal lattice, while the orange regions represent the copper atoms that flow through the crystal structure like a liquid

structure, the Cu ions are distributed within the structure with a large extent of disorder [65,66] (Fig.1.4). This unique structural arrangement allows the system to be surprisingly good p-type electrical semiconductor with a high thermopower as well as electrical conductivity. Besides, addition of the nanostructuring technique essentially can reduce its thermal conductivity too due to the increased phonon scattering.

Chapter 2

COMBUSTION SYNTHESIS OF NIO NANOSTRUCTURES: EFFECT OF SYNTHESIS CONDITIONS ON PARTICLES SIZE, MICROSTRUCTURE AND THERMAL TRANSPORT PROPERTIES

2.1. Overview

This chapter describes synthesis of high purity; nanometer sized surfactant-free nickel oxide (NiO) particles in gram scale using a solution combustion method. In the current study efforts were made to achieve control over the crystallinity and the average particle size of the synthesized NiO nanoparticles by varying synthetic parameters such as the combustion temperature and duration. The as-synthesized materials were characterized by X-ray diffraction (XRD), transmission electron microscopy (TEM), gas pycnometry and gas adsorption analysis (BET). The average particle size of the synthesized NiO nanoparticles increases significantly with increasing combustion temperature while the specific surface area decreases. A specific surface area of ~ 100m^2/g was obtained for NiO nanoparticles with size range from 3 to 7 nm synthesized at 300 °C. High density pellets of the synthesized NiO nanoparticles were obtained using spark plasma sintering (SPS) and uniaxial hot pressing and their thermal conductivity was measured in the temperature range from 300 to 775 K. The thermal conductivity of pressed

pellets of the synthesized NiO nanoparticles is drastically decreased compared to that of NiO single crystal. A total thermal conductivity as low as 12 W/m·K at 300 K was measured for the SPS pellet of NiO nanoparticles synthesized at 300 °C. This corresponds to about a 60% reduction of the thermal conductivity compared to that of bulk NiO. The synthesized surfactant-free NiO nanoparticles, because of their chemical stability and the strong dependence of thermal conductivity on particle size, are well suited for use as nanoinclusions when designing high performance materials for waste heat recovery and solar energy conversion.

2.2 Background Survey

Since the concept of nanostructuring as a promising approach to high performance thermoelectric materials was introduced two decades ago[26,27] tremendous effort has been invested in the design of new nanocomposite materials with high figures of merit. The nanocomposites are generally fabricated by assembling fine nanoparticles of the desired thermoelectric material prepared via various synthetic techniques such as hydrothermal methods [67-71], wet chemical methods [72,73] or mechanical alloying [74-85].Another successful strategy to nanocomposite thermoelectric materials consists of in situ growth of secondary inclusion phases within a bulk thermoelectric material [22,86-95]. The motivation behind the design and implementation of nanostructuring is to take advantage of the reduction in lattice thermal conductivity arising from phonon scattering at grain boundaries and interfaces between the inclusion phase and the matrix. Reduction in lattice thermal conductivity can also be achieved in nanocomposite materials fabricated by direct combination of bulk thermoelectric materials with various volume fractions of independently synthesized nanoparticles of the inclusion phase [96,97]. However, for this approach to become a viable strategy to nanocomposite thermoelectric large

materials, synthetic techniques for large scale production of surfactant-free nanoparticles of the desired inclusion phase must be readily available. In this paper, we discuss a simple scalable synthesis method of surfactant-free NiO nanoparticles for use as inclusion phases in high temperature nanocomposite thermoelectric materials.

Nickel oxide, in bulk or nanoscale form, has been an attractive material for a variety of applications ranging from solar cells [98], electrochromic devices [99], gas sensing[100] to data storage[101]. In addition, nanostructured NiO, because of its large chemical and thermal stability, also shows great promise for use in energy conversion applications. For instance, p-type nanocrystalline NiO can be used as an inclusion phase to promote additional phonon scattering in high temperature p-type thermoelectric composite materials such as half-Heusler phases ($Zr_{0.5}Hf_{0.5}CoSb_{0.8}Sn_{0.2}$ [46] and $Zr_{0.5}Hf_{0.5}Co_{1-x}Rh_xSb_{0.99}Sn_{0.01}$ [90]) or silicon germanium materials ($Si_{80}Ge_{20}B_x$ and $Si_{80}Ge_{20}$ [75,102]). However, the performance of devices and materials fabricated using nanocrystalline NiO particles is strongly influenced by the microstructure (size and morphology) and the accessibility of the surface of the nanoparticles which, in turn, depend on synthetic strategies. Several chemical routes for the synthesis of surfactant-free, highly disperse particles of various metal oxides have been previously developed and used for decades [103-107]. However, these methods are severely limited when it comes to the preparation of particles within the nanometer range. Not only do the synthesized particles show poor crystallinity, but the synthetic protocols are generally complex, difficult to reproduce, and challenging to scale up to industrial quantities due to the high reactivity of the metal precursors. The ability to produce nanometer scale surfactant-free metal oxides with controlled particle shape and size is a cornerstone for their use in nanoscience and nanotechnology.

Recently, the solution combustion method [108] and controlled thermal decomposition of metal nitrates[109] were introduced as optimized techniques to synthesize surfactant-free NiO nanoparticles. The solution combustion technique allows homogeneous mixing in aqueous solution, of reactants at the molecular level yielding precise control over the stoichiometry of the final product. The high temperatures associated with the synthetic process insures homogeneous products with excellent crystallinity, without calcinations steps [110]. The formation of the crystalline NiO phase as well as the size of the synthesized particles is controlled by the fuel to oxidizer (metal nitrate) ratio (ψ) [108,110]. In this thesis, we explore the synthesis of surfactant-free NiO nanoparticles with various sizes using the combustion method. The synthesis parameters such as the preheating temperature of the furnace and duration of the reaction are systematically varied to gain control over the size range of the synthesized nanoparticles. The structure and morphology of the synthesized nickel oxide nanoparticles were characterized by X-ray powder diffraction (XRPD) and electron microscopy (SEM, TEM). Their specific surface area was measured using gas adsorption analysis (BET method). NiO nanoparticles obtained from reactions under various preheating temperatures and duration were compacted using spark plasma sintering (SPS) or uniaxial hot press techniques and the effects of particle size and pressing parameters on the thermal conductivity of the resulting pellets were investigated in the temperature range from 300 to 750K.

2.3. Experimental

2.3.1. Synthesis

All the reagents used in the synthesis are commercially available. Nickel nitrate hexahydrate ($Ni(NO_3)_2.6H_2O$; Aldrich, 99%), was used as the oxidizer and nickel precursor and urea

($(NH_2)_2CO$; EM Science) was used as fuel for the combustion. Aqueous solutions of nickel nitrate and urea were thoroughly mixed by stirring using a magnetic stirrer. The stoichiometric composition of nickel (II) nitrate hexahydrate (oxidizer) and urea (fuel) was calculated using the total oxidizing and reducing valences of the components. The mixture is stoichiometric and the heat of combustion is maximized when the oxidizer to fuel ratio (ψ) equals 1[111]. In this study, the oxidizer to fuel ratio was fixed at the stoichiometric value (ψ = 1). Synthesis at 300, 400 and 600 °C were performed in Pyrex beakers whereas a Quartz beaker was used for reactions with furnace preheated at 800 °C. Homogeneous mixture of nickel nitrate and urea (100 ml of each) was transferred into the appropriate beaker and placed onto a box furnace preheated to the desired reaction temperature. The mixture undergoes a flameless combustion during which the solution initially boils and the mixture gradually dehydrates and finally decomposes to produce NiO nanoparticles with the evolution of a large amount of gases such as N_2, CO_2 and H_2O according to equation (1).

$$3\ Ni(NO_3)_2\ .6H_2O_{(aq)} + 5\ NH_2CONH_{2(aq)} \rightarrow 3NiO_{(s)} + 8N_{2(g)} + 5CO_{2(g)} + 28H_2O_{(g)} \quad (1)$$

After the predetermined reaction time elapses, the beaker was removed from the furnace (at the preheated temperature) and allowed to cool to room temperature and the NiO products were collected. Reaction parameters such as the preheating temperatures and durations were varied to study their effects on nanoparticles size, color and morphology.

Specimens for thermal conductivity measurements were fabricated by spark plasma sintering or hot pressing fine powders of the synthesized NiO nanoparticles under a dynamic vacuum of ~10^{-4} Torr. Pellets obtained from spark plasma sintering was fabricated by cold

pressing the NiO nano-powder under a uniaxial pressure of 50MPa in a graphite die, followed by heating at a rate of 100 °C/min from 25 °C to 700 °C and at 50 °C/min from 700 °C to 900 °C. The total heating time was 12 min including the heating ramp. After consolidation was complete as indicated by no net displacement of the pressing piston, the sample was allowed to cool to room temperature with pressure released. Pellets obtained by uniaxial hot press were fabricated by simultaneously applying a maximum pressure of 100 MPa and a maximum temperature of 900 ^{o} C. The samples were placed into a graphite die with an inner diameter of 10 mm and then sintered under vacuum (10^{-5} Torr). The final working set point of pressure (100 MPa) was first reached with a ramp of 2 MPa/min, followed by a hold of 4 h while the temperature was still rising at a heating rate of 5^{o}C/min to 900 ^{o} C. The maximum temperature and pressure were kept for 1 h to achieve higher strengthening and good compaction of the pellet. The sample was then cooled to room temperature at a cooling rate of 5^{o}C/min simultaneously while the pressure released (2 MPa/min). The density of the resulting pellet was determined by measuring the dimensions and mass. NiO pellets were examined using transmission electron microscopy (TEM) to probe grain growth during spark plasma sintering or hot pressing

2.3.2 Characterization

The resulting NiO nanoparticles were characterized by X-ray powder diffraction for phase identification using CuK_{α} radiation (λ= 1.5406 Å) on an X'Pert Pro, PANalytical system, equipped with a curved graphite crystal monochromator and a scintillation counter, operating in θ-θ geometry with tube settings of 40 kV and 40 mA. The determination of particle size and morphology of the as-synthesized NiO nanoparticles as well as the investigation of the microstructure of spark plasma sintered or hot pressed pellet of NiO nanoparticles were

performed using a JEOL 2010 microscope in both bright field image and selected area electron diffraction (SAED) modes operated at 200 kV. TEM specimens of hot pressed and spark plasma sintered pellets were prepared by dicing 3 mm discs using an ultrasonic disc cutter (model 170, Fischione). The discs were mechanically polished using a dimple grinder with a load of 12 g (Gatan 1656), followed by Ar^+-ion milling (FISCHIONE 1010). For the characterization of the as-synthesized NiO nanoparticles by TEM, suspensions of the powders in alcohol were dropped onto a holey carbon grid.

Specific surface area measurements were performed using the N_2 gas adsorption BET method on a Micromeritics ASAP 2020. The specific surface areas were calculated by comparing the adsorption capacity of the sample at room temperature and low temperature (using liquid N_2). The gas was dosed 11 times and the average of the values obtained was reported with their standard deviations. Powder density measurements were performed using helium gas pycnometry on a Micromeritics Accupyc II 1340. Reported data with their standard deviations are the average of 10 measurements. Synthetic parameters, specific surface area, particle size range, powder density and color of the synthesized NiO nanoparticles are summarized in Table I. Thermal diffusivity data were measured using a Netzsch LFA 457 laser flash system. A pyroceram reference material was measured alongside each sample. Measurements were made under flowing N_2 gas (>30 mL/min) from 300 K to 775 K at increments of 25 K. C_p values for thermal conductivity calculations were extracted from the laser flash data and are comparable to the C_p values of Bulk NiO reported earlier[112].

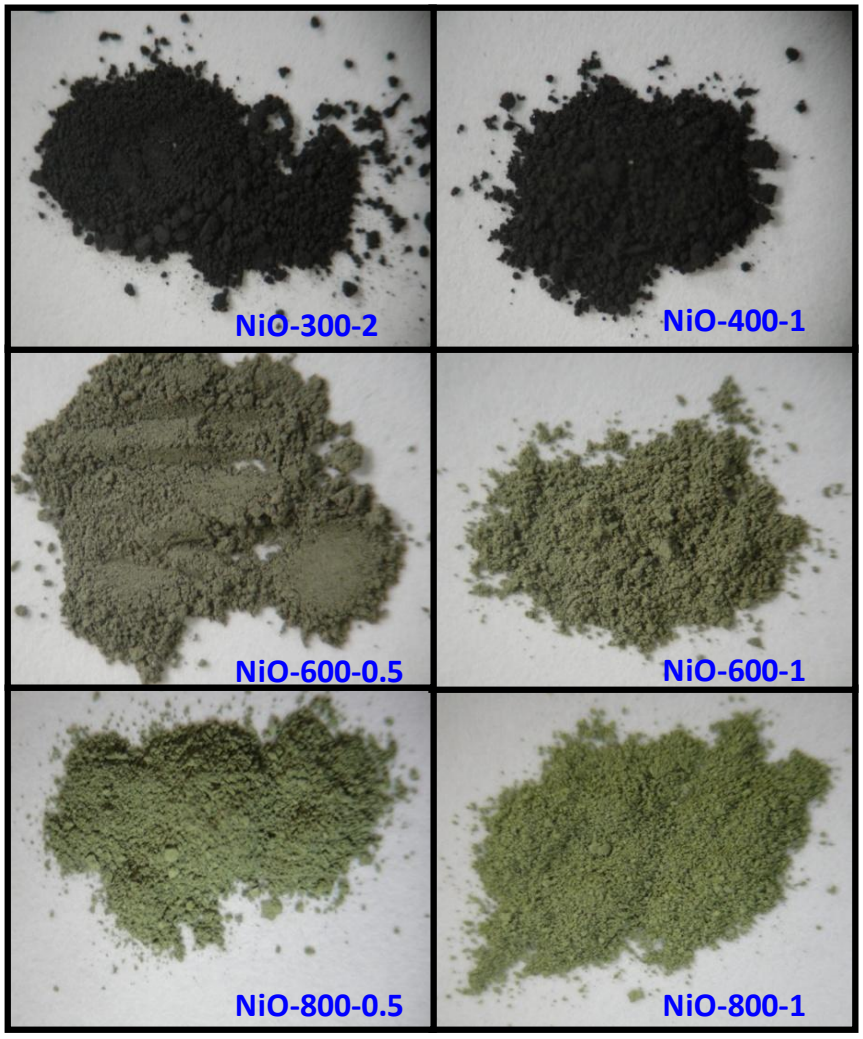

Figure 2.1 : NiO nanoparticles synthesized at various combustion temperatures and durations

2.4. Results and Discussion

2.4.1. Synthesis and X-ray diffraction

Surfactant-free NiO nanoparticles can be synthesized in fairly large quantities via combustion of a mixture of nickel nitrate (oxidizer) and urea (fuel). However, the formation of the crystalline NiO phase strongly depends on the scale of the reaction mixture as well as the temperature at which the furnace was preheated. For instance, to produce NiO nanoparticles at 300 °C with particle sizes below 7 nm, a stoichiometric mixture of nickel nitrate and urea required a minimum of 2 h for completion. When the furnace is preheated to 400 °C, NiO nanoparticles with a similar size range can be obtained within 1hr. NiO nanoparticles with a size range between 100 and 150 nm could be synthesized within 30 min with the furnace preheated at 800°C (Table 2.1). The color of the synthesized NiO nanoparticles changes gradually from black to dark green to green as the furnace preheating temperature and reaction time increase. The observed change in the color of the synthesized NiO nanoparticles can be explained by the presence of various concentration of Ni_2O_3 impurity phase in the sample [113,114]. As can be seen from Table 2.1, NiO powders with small average particle size showed lower density (high porosity) compared to the bulk counterpart (6.8 g/cm^3) [115]. The color of the synthesized NiO nanoparticles changes with variations in synthetic parameters such as temperature and duration suggesting change in the average particle size of the final product. The color of the synthesized NiO nanoparticles changes gradually from black to dark green to green as the combustion temperature and combustion time increase (Figure 2.1). The observed change in the color of the synthesized NiO nanoparticles can be explained by the presence of various concentration of Ni_2O_3 impurity phase in the sample. The small particle size, high porosity and high surface area

are favorable to the oxidation of the surface of NiO (green) nanoparticles to Ni_2O_3 (black). The conversion rate of NiO to Ni_2O_3 decreases with increasing average particle size and decreasing specific surface area resulting in the observed gradual change in the color of the synthesized NiO powders (Figure 2.1).

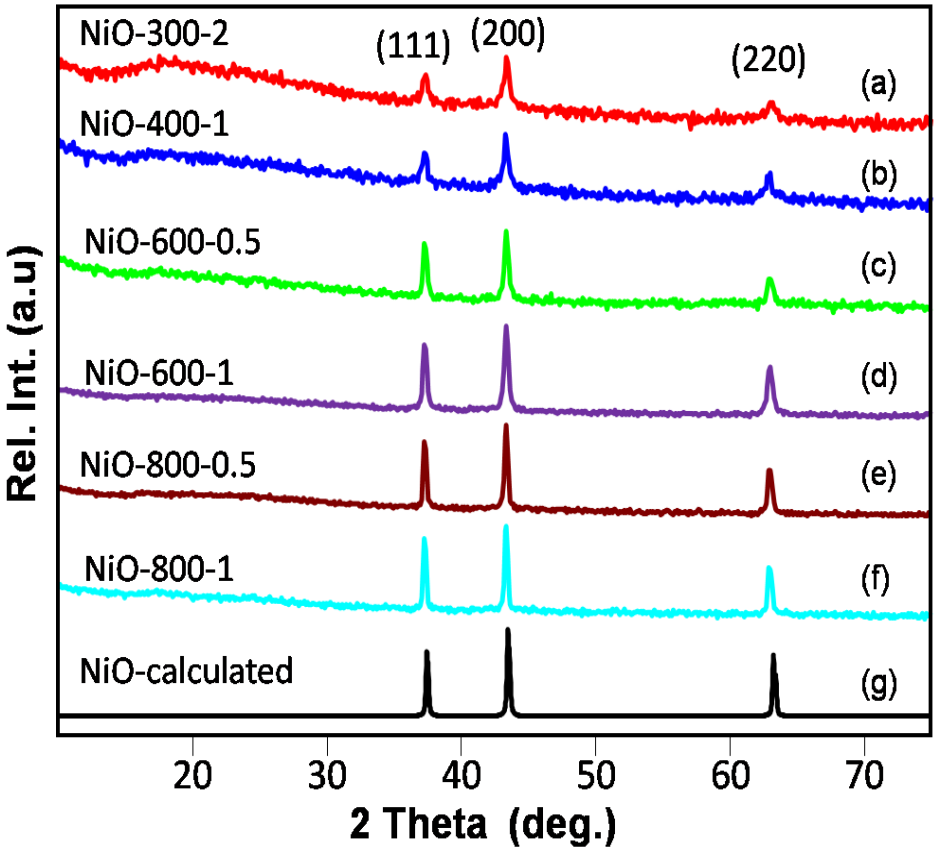

Figure 2.2 : X-ray diffraction pattern of NiO nanopraticles synthesized at: (a) 300 0 C for 2 hr; (b) 400 0C for 1 hr; (c) 6000C for 30 min; (d) 600 0C for 1 h; (e) 800 0C for 30 min and; (f) 800 0C for 1 h. The theoretical pattern of NiO is shown for comparison.

Figure 2.2 shows a comparison of X-ray diffraction patterns of NiO nanoparticles synthesized at various temperatures with the theoretical pattern calculated from NiO structural data [116]. All diffraction peaks can be indexed with the NiO fcc lattice. No additional peaks of any impurity phase could be detected on the diffraction patterns. Except for the broad feature between 15^o and 25^o (2-θ) on the diffraction patterns of NiO-300-2,NiO-400-1and NiO-600-0.5, which is attributed to amorphous Ni_2O_3, no additional peaks of any other impurity phase could be detected on the diffraction patterns. The presence of amorphous Ni_2O_3 in NiO- 300-2 and NiO-600-0.5 samples was also confirmed by X-Ray photoelectron spectroscopy(XPS)(Fig. 1.3). The broad O1s (Ni_2O_3) and Ni $2p_{3/2}$ (+ 3) peaks in the XPS spectra of the NiO-300-2 sample (Fig. 3A and B), suggests the presence of a large fraction of Ni_2O_3. However, the fraction of Ni_2O_3 is sufficiently smaller in the NiO-600-0.5 sample as can be appreciated by the large decrease in the intensity of O1s (Ni_2O_3) and Ni$2p_{3/2}$ (+3) peaks in the XPS spectra

The intensities of (111), (200) and (220) peaks on the XRD patterns of the synthesized NiO nanoparticles are comparable with those of corresponding peaks on the theoretical pattern suggesting that well crystalline NiO nanoparticles could be synthesized via the solution combustion method. The broadening of diffraction peaks of the samples produced from lower combustion temperatures indicates the formation of NiO nanoparticles with smaller sizes.

2.4.2. Particle size and specific surface area

Selected transmission electron microscopy images of the as-synthesized NiO nanoparticles are shown in Figure 2.4. Aggregates of spherical NiO nanoparticles with particle size ranging from 3 to 7 nm are obtained from combustion of nickel nitrate and urea at 300 °C over 2h (Figure 2.4A). The specific surface area of the synthesized material, determined using N_2 gas adsorption analysis (BET) is ~100 m^2/g. The measured density of 6.177(8) g/cm^3 (Table 2.1) corresponds to

about 91% of the theoretical density of bulk NiO (6.8 g/cm^3) [115]. The reduced density again suggests that the synthesized NiO nanoparticles contained some Ni_2O_3 (4.84 g/cm^3) impurity phase. The estimation of the fraction (x) of Ni_2O_3 impurity using the equation d = (1- x) d(NiO) + x d(Ni_2O_3), where d is the measured density of the sample, indicates that NiO powders synthesized at 300 °C contain approximately 32% Ni_2O_3 as an amorphous impurity phase. Increasing the furnace preheating temperature to 400 °C resulted in well crystalline NiO nanoparticles with particles size between 7 to 10 nm (Figure 2.4B). The small increase in particle size results in a decrease of the specific surface area of the synthesized materials to 52 m^2/g. Aggregates of NiO nanoparticles with increasingly larger particle sizes and broader size range are obtained when the furnace is preheated to 600 and 800 °C. NiO nanoparticles synthesized at 600 °C for 1h show particle sizes between 24 and 50 nm (Figure 2.4D) while particles synthesized at 800 °C for 1h are in the size range of 125 to 350 nm (Figure 1.4E). As a result of the large increase in the particle size of the synthesized materials, the corresponding specific surface area is drastically reduced (Table 2.1).

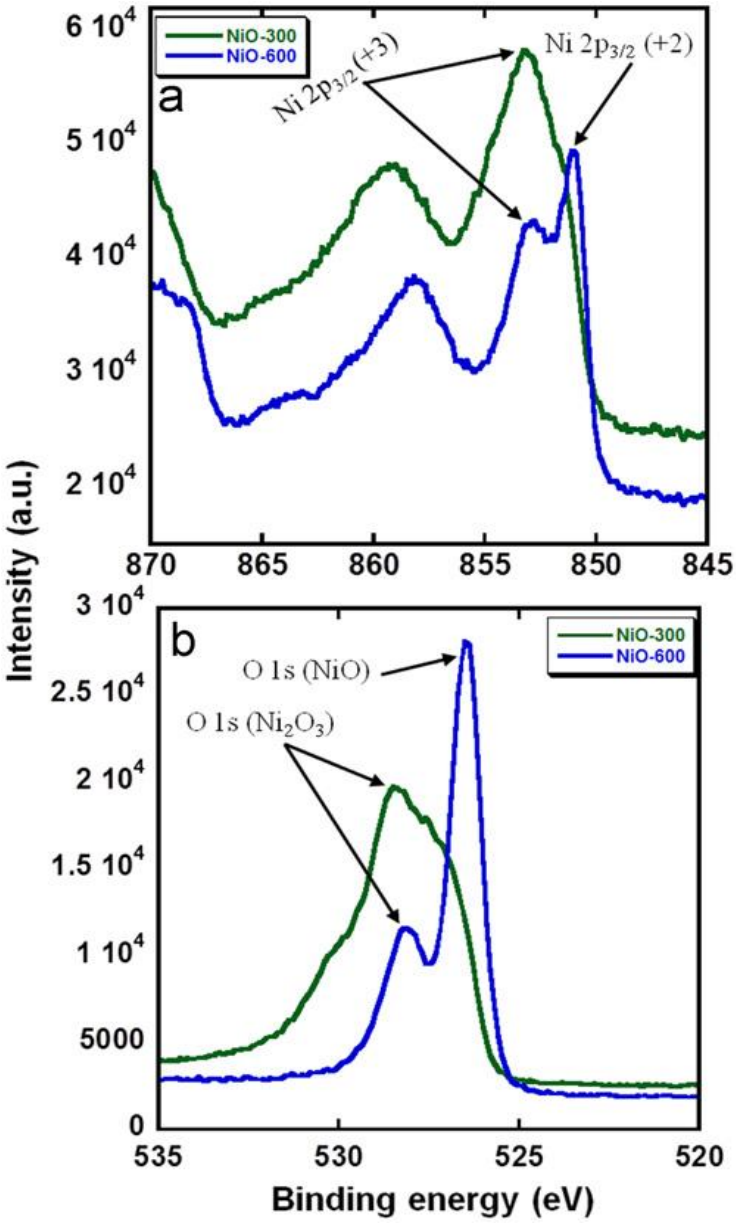

Figure 2.3 : XPS spectra of NiO nanoparticles synthesized at 300 ^{o}C for 2h and 600 ^{o}C for 30min:(a) Ni2p and (b) O1s.

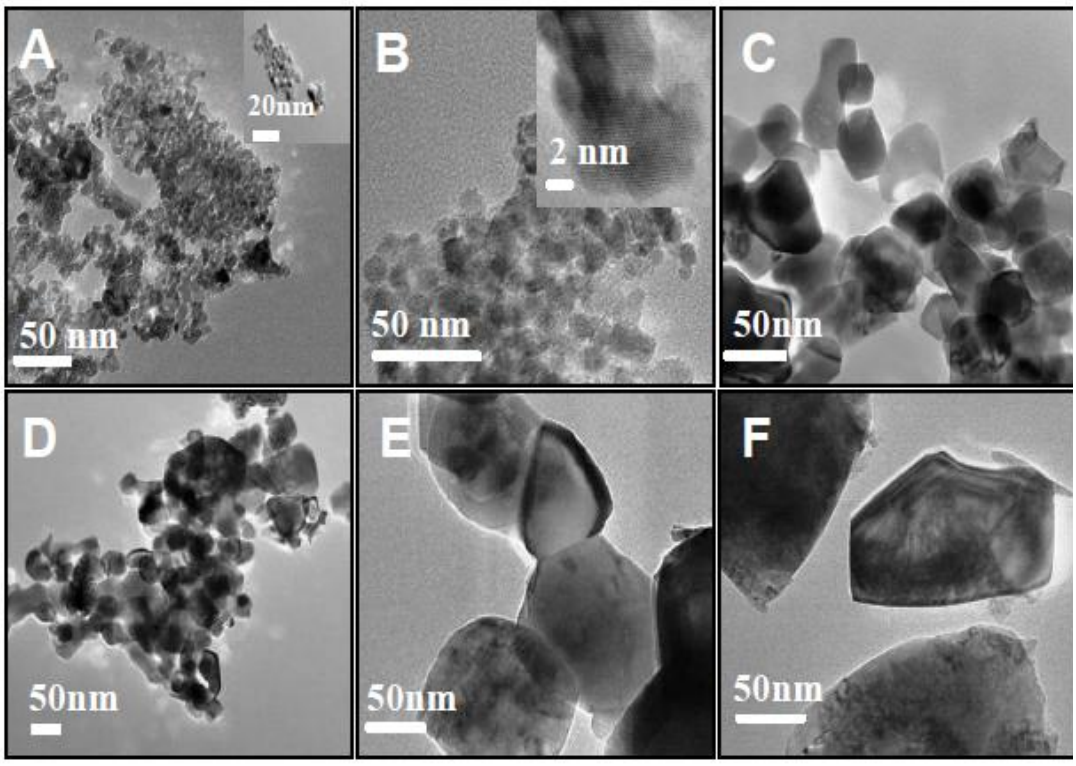

Figure 2.4: Selected transmission electron microscopy images of nickel oxide nanoparticles synthesized at: (A) 300 0C for 2 h; (B) 400 0C for 1 h; (C) 600 0C for 30 min; (D) 600 0C for 1 h; (E) 800 0C for 30 min; (F) 800 0C for 1h. Inset in (B) corresponds to high resolution TEM of a single NiO nanoparticle synthesized at 400 ^{0}C for 1 h.

Table 2.1 : Particle size range, BET specific surface area and density of NiO nanoparticles synthesized at different temperature. * NiO-300-2 corresponds to NiO nanoparticles

Sample Code	Reaction temperature (^{o}C)	Reaction duration (h)	Particle size from TEM (nm)	BET surface area (m^2/gm)	Density (g/cm^3)	Color
*NiO-300-2	300	2	3-7	99.70(3)	6.177(8)	black
NiO-400-1	400	1	7-10	52.13(3)	6.226(2)	black
NiO-600-0.5	600	0.5	24-34	8.59(2)	6.729(2)	dark-green
NiO-600-1	600	1	24-50	4.88(2)	6.731(4)	green
NiO-800-0.5	800	0.5	140-150	2.73(2)	6.880(4)	green
NiO-800-1	800	1	125-350	1.85(2)	6.925(4)	green

2.4.3. TEM and Thermal conductivity of NiO nanoparticle pellets

As stated in the introduction, independently synthesized NiO nanoparticles can be used as additional phonon scatters at high temperatures in p-type thermoelectric composite materials such as the half-Heusler or silicon germanium phases. To probe the suitability of the synthesized NiO nanoparticles for such applications, we have investigated the microstructures and the thermal conductivity of the synthesized NiO nanoparticles after compaction using spark plasma sintering or uniaxial hot pressing techniques. The density and the particle size range of the resulting pellets are given in Table 2.2.

Figure 2.5 shows selected bright field TEM images of NiO nanoparticles after spark plasma sintering (Figure 2.5A, 2.5B and 2.5C) and hot pressing (Figure 2.5D). The fcc (Fm-3m) structure of NiO with lattice parameter a = 8.35 Å, was confirmed by a selected area electron diffraction pattern obtained from one of the grains (See inset of Figure 2.5A). After spark plasma sintering, the grain size of NiO nanoparticles synthesized at 300 °C for 2 h is between 115 and 500 nm (Table 2.2). This is 30 to 70 times the size of the initial nanoparticles, indicating drastic grain growth during the spark plasma sintering process. The grains are highly crystalline, randomly oriented and densely packed with well defined grain boundaries (Figure 2.5A). The observed packing of grains is consistent with the pellet (6.285 g/cm^3) 92% NiO theoretical density (when compared to the 6.8 g/cm^3 theoretical density of NiO). The increase in the density of the sample after SPS, when compared to the measured powder density of 6.177 g/cm^3 for the as-synthesized NiO nanoparticles, suggests a significant reduction of the fraction of Ni_2O_3 impurity phase in the resulting pellet. Ni_2O_3 is known to decompose to NiO with loss of O_2 around 600 °C [117]. This decomposition reaction presumably occurs during the spark plasma

sintering process at 900 °C resulting in NiO pellets containing a smaller fraction of the Ni_2O_3 phase.

Pellets obtained from NiO nanoparticles synthesized at 400 °C for 1h also showed large grains after spark plasma sintering. The grain size is between 535 and 800 nm which represents 70 to 80 times the size of the as-synthesized NiO nanoparticles. The grains are also randomly oriented and densely packed. The pellet obtained from NiO nanoparticles synthesized at 800 °C showed the smallest grain growth after spark plasma sintering with the particle size ranging from 565 to 820 nm. The grains are densely packed with clean boundaries, consistent with the pellet 95% NiO theoretical density. The pellet fabricated from NiO nanoparticles synthesized at 400 °C for 1h via uniaxial hot pressing showed the largest grain growth (up to 130 times the size of initial nanoparticles) and a broader particle size range (from 413 nm to 1300 nm). The particles are composed of small crystalline sub-grains (~ 400 nm) and larger grains (~1300 nm). This combination of small and large grains results in more effective packing of the particles (Figure 2.3D), which is consistent with the pellet 98% NiO theoretical density (Table 2.2).

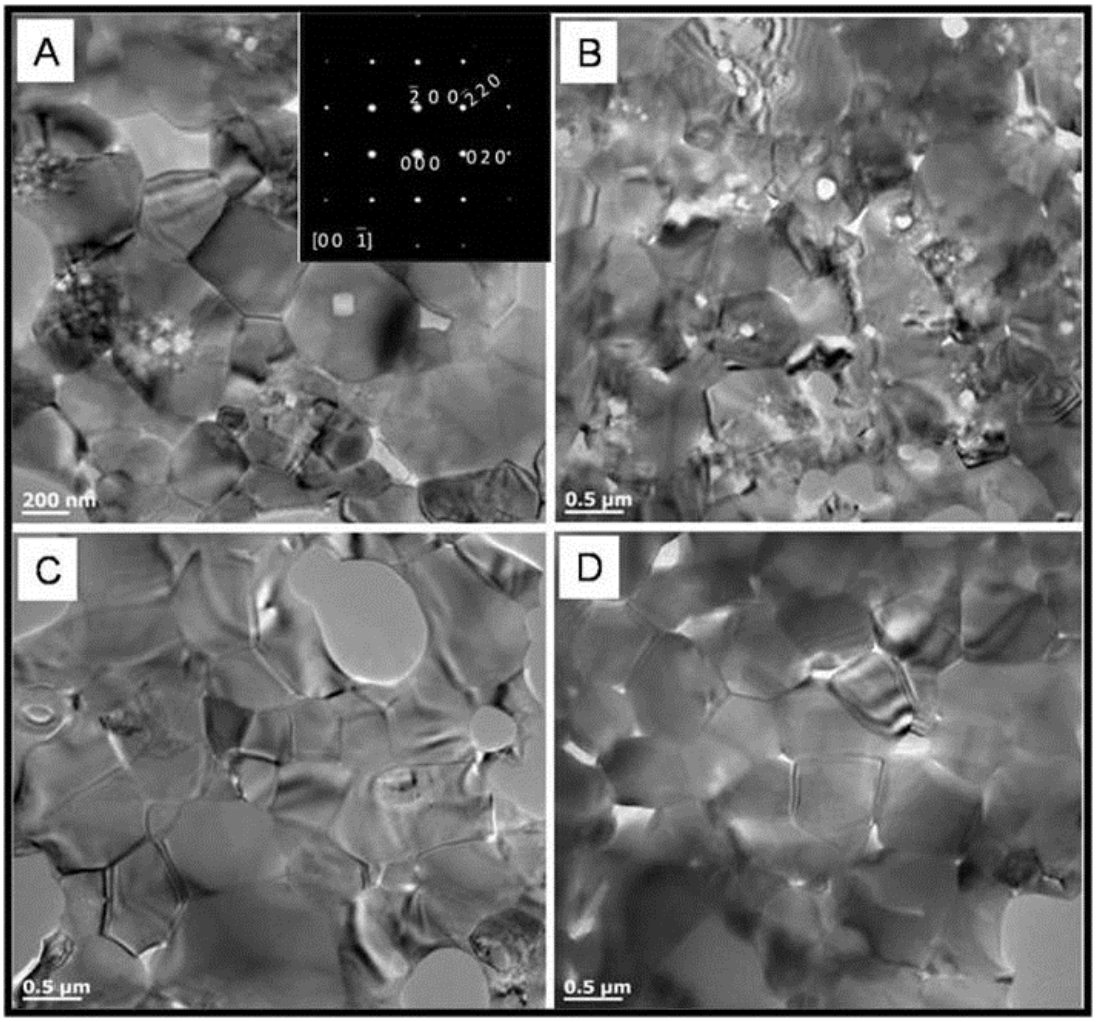

Figure 2.5 : Selected TEM images of pellets NiO nanoparticles fabricated by Spark plasma sintering or uniaxial hot pressing: (A) NiO – 300- 2- SPS; (B) NiO – 400- 1- SPS; (C) NiO – 400- 1- HP; (B) NiO – 800- 0.5- SPS.

Table 2.2 : Density and grains size (TEM) of NiO pellets fabricated by hot pressing and spark plasma sintering. *NiO-300-2-SPS corresponds to pellet of NiO-300-2 sample fabricated by SPS

Pressing technique	Sample Code	Pellet density (g/cm^3)	Grain size from TEM (nm)
SPS	NiO-300-2-SPS	6.285(6)	115-500
SPS	NiO-400-1-SPS	6.253(5)	535-800
HP	NiO-400-1-HP	6.665(6)	413-1300
SPS	NiO-800-0.5-SPS	6.443(1)	565 -820

Despite the drastic grain growth of the synthesized NiO nanoparticles after processing by spark plasma sintering and uniaxial hot press, the grain size for the pellets fabricated using NiO nanoparticles synthesized at 300 °C for 2h are still in the size range (115-500 nm) suitable for effective interface phonon scattering when embedded in high temperature thermoelectric materials such as the silicon germanium alloys. For instance, the average phonon mean free path in heavily doped $Si_{80}Ge_{20}$ alloy is in the range of 200 to 300 nm at room temperature [118]. This suggests that NiO inclusions with size range up to 300 nm can significantly reduce the phonon thermal conductivity of such alloys. However, phonon scattering at grain boundaries are more effective when the inclusion phases are considerably smaller than the phonon mean free path in the host matrix. Therefore surfactant-free NiO nanoparticles with size ranges between 10 and 150 nm, which can be synthesized at up to 10 grams per hour via combustion of nickel nitrate and urea at temperatures between 400°C and 800 °C, are suitable for use as inclusions in the fabrication of silicon germanium nanocomposites.

Although, spark plasma sintering and hot pressing of free-standing NiO nanoparticles result in large grain growth, we anticipate that by embedding the nanoparticles in high melting point matrices such as silicon germanium alloys, the matrix-nanoparticle interactions will

significantly suppress the particle growth during thermal processing. Therefore, $Si_{80}Ge_{20}/NiO_{(nano)}$ composites with nanometer scale NiO inclusions can be obtained using spark plasma sintering or hot pressing. Interestingly, the average electron mean free path in heavily doped $Si_{80}Ge_{20}$ alloy is about 5 nm[118], suggesting that by carefully tailoring the size range of the NiO inclusions, electron flow throughout the $Si_{80}Ge_{20}$ matrix will not be significantly affected, thus resulting in nanocomposites with high figures of merit (ZT).

Figure 2.6 shows the temperature dependence of the thermal conductivity of the synthesized NiO nanoparticles after spark plasma sintering or uniaxial hot pressing. Temperature dependence of the thermal conductivity of NiO single crystal[119] is shown for comparison. Regardless of the synthesis and pressing conditions, the thermal conductivity of all samples decreases with increasing temperature. All thermal conductivity curves showed a change in slope between 510 and 530 K which is the magnetic transition (Néel temperature) region of bulk NiO. At lower temperatures

(300 K to 500 K), the temperature dependence of the thermal conductivity for all samples follows the power law $\kappa \sim T^{-\lambda}$ suggesting that the thermal conductivity in this temperature range is dominated by acoustic phonon scattering. Similar behavior of the thermal conductivity was observed for NiO single crystal (Figure 2.6). The power exponent (λ) increases with the average grain size within the specimen which in turn is a function of the sample processing conditions. The observed values of λ are 1.47 for NiO-300-2-SPS, 1.73 for NiO-400-1-SPS, and 1.93 for 800-0.5-SPS samples. A rather steeper dependence ($\lambda = 2.11$) was observed for the NiO-400-1-HP specimen. Around the magnetic transition temperature, all thermal conductivity curves show a continuous minimum contrasting with the sharp change in slope observed for the thermal conductivity of NiO single crystal (Figure 2.6).

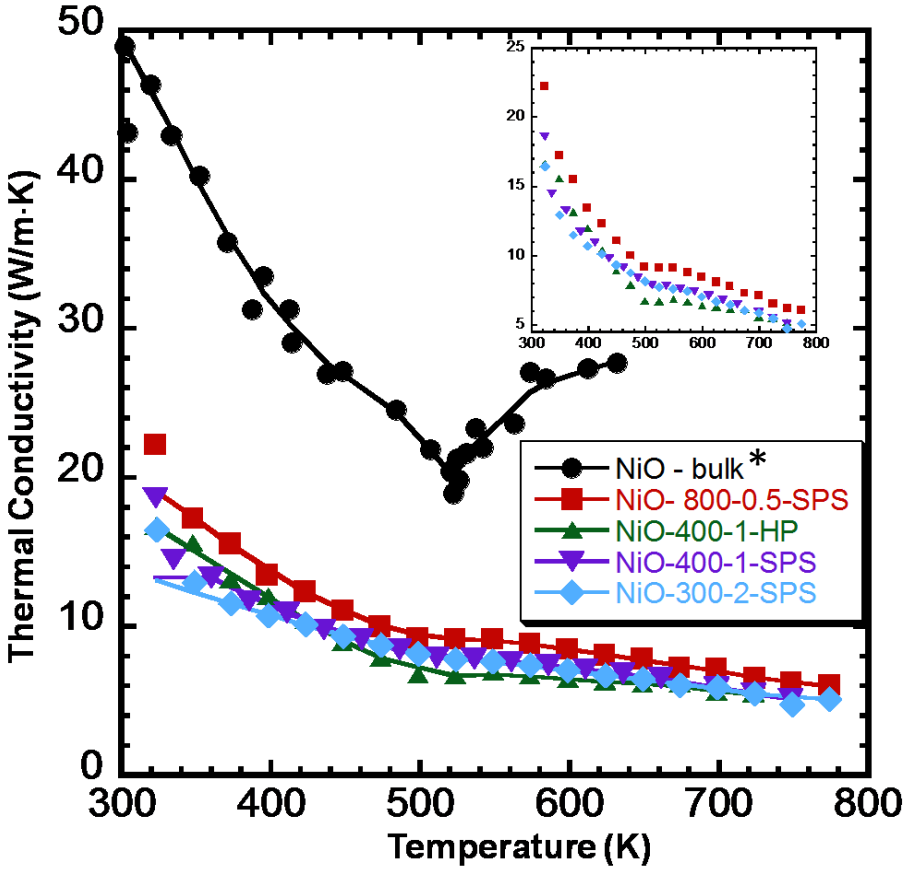

Figure 2.6 : Temperature dependence of the thermal conductivity of NiO nanoparticles pellets obtained by spark plasma sintering or uniaxial hot pressing. The thermal conductivity of NiO single crystal adapted from ref. 53 is plotted for comparison

This phenomenon was described as resulting from critical scattering of phonons by the spin system at the Néel temperature, in addition to the existing acoustic, boundary and impurity scattering mechanisms [119,120].

As it can be seen from the inset of Figure 2.6, the abruptness of the change in slope of the thermal conductivity curves decreases when moving from NiO-800-0.5-SPS to NiO-300-2-SPS. This suggests that grain sizes within the pellets play a key role in how phonons are scattered by the spin system at the Néel temperature. The broad range of NiO grain sizes and the random orientation of the grains within the pellets, as revealed by the TEM images (Figure 2.5), lead to regions of different Néel temperatures at which the critical phonon scattering by the spin system occurs. The density of such regions increases with decreasing average grain size within the pellets resulting in the weakening of the anomaly in the thermal conductivity curves. At higher temperatures (i.e. above the magnetic transition temperature), the thermal conductivities of the synthesized materials continue to decrease at a slower slope, again contrasting with the thermal conductivity observed in bulk NiO, which increases with temperature above the Néel temperature (Figure 2.6).

The most interesting finding in the study is the strong suppression of the thermal conductivity of NiO when grain size is on the nanometer scale. The overall decrease in the thermal conductivity of NiO nanoparticle pellets compared to that of the NiO single crystal is higher than 60%. At room temperature, the thermal conductivity dropped from ~50 W/m·K for bulk NiO to ~20 W/m·K for the NiO-800-0.5-SPS specimen. This sharp decrease in the thermal conductivity likely arises from the increased phonon scattering at the multiple grain boundaries within the pellets. At high temperatures, phonon scattering at grain boundaries is added to the existing acoustic phonon scattering mechanism resulting in even larger decreases in the thermal conductivity of the NiO nanoparticle pellets compared to that of the NiO single crystal. At 750 K, a thermal conductivity of ~5 W/m·K was measured for the NiO-300-2-SPS specimen. By extrapolation the current thermal conductivity temperature dependence, a value of ~4W/m·K can

be anticipated at 1000 K. The observed dependence of the thermal conductivity of NiO on the grain size could be beneficial in the design of bulk nanocomposite thermoelectric materials with low thermal conductivity and high figures of merit. Assuming, small grain growth of the synthesized NiO nanoparticles when embedded in a bulk matrix, nanocomposites with significantly lower thermal conductivity can be designed with carefully chosen matrices.

2.5 Conclusions

Surfactant-free NiO nanoparticles with various and controllable size ranges can be produced in a relatively short time via solution combustion method using nickel nitrate as an oxidizer and urea as the fuel. The particle size range and the crystallinity of the final product can be controlled by adjusting the furnace preheating temperature and the duration of the reaction. For example, a minimum of 2 h is required to produce NiO nanoparticles with size range between 3 and 7 nm at a combustion temperature of 300 °C. However, NiO nanoparticles with size range of 140-150 nm can be obtained within 30 minutes when the furnace preheated at 800 °C. The thermal conductivity of pressed pellets of the synthesized NiO nanoparticles are reduced by more than 60% compared to that of NiO single crystal. The synthesized NiO nanoparticles, because of their chemical stability at high temperature and the strong dependence of the thermal conductivity on the particle size, are suitable for use as inclusions in the design of nanocomposite materials for high temperature energy conversion.

Chapter 3

COMBUSTION SYNTHESIS OF CO_3O_4 NANOSTRUCTURES: EFFECT OF SYNTHESIS CONDITIONS ON PARTICLES SIZE, MAGNETISM AND TRANSPORT PROPERTIES

3.1 Overview

This chapter opens with a brief description about the importance of mixed valence Cobalt oxide(Co_3O_4), followed by the experimental part explaining the synthesis of surfactant-free Co_3O_4 nanostructures with various particles size ranges via the solution combustion method using cobalt nitrate solution as cobalt precursor and urea as the combustion fuel. Control over the average particles size range by tuning the reaction ignition temperature between 300 °C and 800 °C is one of the targets of this study. Further it describes various characterization methodologies to ascertain the structure –properties relationship of this nonmaterial. For example, X-ray diffraction (XRD) and helium gas pycnometry indicated the formation of single phase Co_3O_4 nanoparticles with spinel structure. Transmission electron microscopy (TEM) studies revealed an increase of the size range from 5–8 nm to 200–400 nm for Co_3O_4 nanoparticles synthesized at 300 °C and 800 °C, respectively. The corresponding decrease in the specific surface area from 39 m^2/g to ~2 m^2/g was confirmed by gas adsorption analysis using BET techniques. Magnetic

susceptibility measurements revealed a dominant antiferromagnetic (AFM) ordering and the Néel temperature decreases with decreasing average particle size range from 31 K (200–400 nm) to 25 K (5–18 nm). Interestingly, effective magnetic moments (ranging from 4.12 μ_B to 6.16 μ_B) substantially larger than the value of 3.9 μ_B expected for Co^{2+} ions in the normal spinel structure of Co_3O_4 were extracted from the inverse susceptibility data. This finding was rationalized taking into account the disordered distribution of Co^{2+} and Co^{3+} ions in the Co_3O_4 inverse spinel structures ($[(Co^{2+})_{1-x}(Co^{3+})_x]^{tet}[(Co^{2+})_x(Co^{3+})_{2-x}]^{oct}O_4$) where the inversion degree (x) depends on the synthesis temperature. Transport measurements using hot pressed pellets of Co_3O_4 nanoparticles indicated p-type semiconducting behavior and drastic reductions in the thermal conductivity with decreasing average particle size.

3.2 Background survey

Ongoing widespread research efforts focusing on the development of facile and energy efficient synthesis routes for large scale production of new and/or old inorganic materials in their nanometer size is driven by their superior properties when compared to their bulk counterpart [121-125]. The interesting and technologically useful properties of nanostructured materials are mainly attributed to quantum confinement effects and variation in the specific surface area arising from their small particle size[24,126]. For instance, the controlled manipulation of the shape and/or size of various inorganic nanomaterials have been shown to enhance properties such as: thermal conductivity, electrical conductivity, optical, magnetic and catalytic behavior. Nanostructured transition metal oxides (TMO) such as NiO, CoO, Fe_3O_4, Co_3O_4, CuO and MnO are the most popular systems due to their attractive industrial applications[121-125]. Among these TMO, spinel cobalt oxide (Co_3O_4) has received considerable attention due to its chemical and thermal stability and its potential application in gas sensing[127], electro-photochemical process[128], catalysis[129,130] and batteries[131,132]. Over the past decades, a variety of Co_3O_4 nanostructures[133-141] such as nanowire, nanotubes, nanosheets nanocubes, nanoparticles etc., have been synthesized using various methods which typically involve thermal decomposition of precursors [142-144]. However, to fully achieve their ultimate performance, simple strategies for large scale production of surfactant-free Co_3O_4 nanostructures with control over their particles size must be developed. Along this line, the solution combustion synthesis (SCS) method has been widely used as a simple and energy efficient process for the fast large scale production of complex metal oxides with high surface area and high purity[108,145-147]. This method allows homogeneous mixing of the metal salt precursor and a fuel of choice at the molecular level in aqueous solution, enabling a

precise control over the stoichiometry of the final product. The high temperatures associated with the reaction of the reactants at the point of ignition ensure the formation in a relatively short time of homogeneous products with excellent crystallinity. Despite the fact that Co_3O_4 powders have been synthesized using SCS methods, it appears to the best of the authors' knowledge that systematic investigations on the effect of synthesis conditions, such as the reaction ignition temperature (preheating temperature of the furnace), on the particle size, specific surface area, and the magnetic and transport properties of the resulting nanostructures have not been reported so far. Although previous studies on the magnetic behavior of Co_3O_4 nanoparticle samples synthesized using various techniques have consistently reported a significant drop of the Neel temperature (T_N) with decreasing average particle size, the effective magnetic moment (μ_{eff}) of Co_3O_4 nanoparticle samples calculated from susceptibility data are generally larger than the spin only value of 3.9 μ_B expected for Co^{2+} and there is a large disparity on the magnitude of the reported μ_{eff} values [142,148,149]. This suggests that the temperature used for the synthesis of the Co_3O_4 nanoparticle samples investigated in those studies may have a strong influence on the effective magnetic moment. For example, a sufficiently high reaction temperature can induce a disordered distribution of Co^{2+} and Co^{3+} ions in various metallic sites within the spinel structure of Co_3O_4 leading to the alteration of the magnetic and electronic properties.

Here, we report a fast production of surfactant-free Co_3O_4 nanoparticles with various sizes using a modified solution combustion synthesis method. We tune the reaction ignition-temperature to achieve Co_3O_4 nanoparticles product with various particle size range. The structure and morphology of the synthesized Co_3O_4 nanoparticles were characterized by X-ray powder diffraction and scanning electron microscopy. Their specific surface area was measured using gas adsorption analysis following the Brunauer, Emmett and Teller (BET) method.Optical

properties have been studied by using UV-Vis spectrocopy. The magnetic behavior of Co_3O_4 nanoparticles obtained from reactions under various preheating temperatures and their electronic and thermal properties measured using hot pressed pellets are discussed in the light of changes in the disordered distribution of Co^{2+} and Co^{3+} ions in the spinel structure of the synthesized Co_3O_4 nanostructures.

3.3 Experimental

3.3.1 Synthesis

All the reagents involved in the synthesis are commercially available and were used as received without further purifications. Cobalt nitrate hexahydrate ($Co(NO_3)_2.6H_2O$; Aldrich, 99%) was used as the oxidizer and cobalt precursor, and urea ($(NH_2)_2CO$; EM Science) was used as fuel for the combustion reaction. Aqueous solutions of cobalt nitrate and urea were thoroughly mixed by stirring using a magnetic stirrer. The stoichiometric composition of Cobalt (II) nitrate (oxidizer) and urea (fuel) was calculated using the total oxidizing and reducing valences of the components. The mixture is stoichiometric and the heat of combustion is maximized when the oxidizer to fuel ratio (ψ) equals 1 [111]. In this study, the oxidizer to fuel ratio was fixed at the stoichiometric value ($\psi = 1$). The aqueous solution containing the redox mixture was taken in a Pyrex crystallizing dish and stirred for 10 min. Then the mixture was transferred into the appropriate beaker (Pyrex beaker for reactions below 600 °C and Quartz beaker for the reaction at 800 °C) and placed into a box furnace preheated to the desired combustion temperature (reaction ignition temperature). Instantaneous combustion reaction occurs during which the solution initially boils and the

mixture gradually dehydrates and finally decomposes to produce Co_3O_4 nanoparticles with the evolution of a large amount of gases such as N_2, CO_2 and H_2O according to equation (1).

$$9\ Co(NO_3)_2\ .6H_2O(aq) + 14\ NH_2CONH_2(aq) \rightarrow 3\ Co_3O_{4(s)} + 23\ N_{2(g)} + 14\ CO_{2(g)} + 82\ H_2O_{(g)} \quad (1)$$

After the reaction, the beaker was removed from the furnace and allowed to cool to room temperature and the cobalt oxide products were collected. Reaction parameters such as the reaction-ignition temperature and the duration of the reaction were varied to study their effects on the size range of Co_3O_4 nanoparticles. A complete reaction was achieved within 1h with the furnace temperature set at 300°C. Increasing the furnace preheating temperature to 400°C resulted in the formation of pure Co_3O_4 nanoparticles within 30 min. Two additional batches of Co_3O_4 nanoparticles were prepared in 30 min with the furnace preheating temperature set at 600 °C and 800 °C.

3.3.2 Characterization

The as-synthesized Co_3O_4 nanoparticles were characterized by X-ray powder diffraction for phase identification using CuK_α radiation (λ= 1.5406 Å) on an X'Pert Pro, PANalytical system, equipped with a curved graphite crystal monochromator and a scintillation counter, operating in θ-θ geometry with tube settings of 40 kV and 40 mA. To determine the particle size range and morphology of the as-synthesized Co_3O_4 nanopowder sample field emission scanning electron microscopy (using the LEO 1530 Variable Pressure) and high resolution electron microscopy images (using a JEOL 2010 microscope operated at 200 kV) were performed on various samples. Specific surface area measurements were performed using the N_2 gas adsorption BET method on a Micromeritics ASAP 2020. The specific surface areas were calculated by comparing the adsorption capacity of the sample at room temperature and low temperature (using liquid N_2).

The gas was dosed 11 times and the average of the values obtained was reported with their standard deviations. Powder density measurements were performed using helium gas pycnometry on a Micromeritics Accupyc II 1340. Reported data with their standard deviations are the average of 10 measurements. Synthetic parameters, specific surface area, particle size range and powder density of the synthesized Co_3O_4 nanoparticles are summarized in Table 3.1. UV–visible absorption spectra were recorded using a spectrophotometer Varian Cary 5000 UV-Vis-NIR Spectrophotometer at room temperature. The powder samples, prepared by diluting the samples with standard Barium Sulphate powder were used for the UV–visible measurements. The measurements were done within the range of 250-1000 nm.

Table 3.1: Particle size range, BET specific surface area and density of Co_3O_4 nanoparticles synthesized at different temperature. *Co_3O_4-300-1 corresponds to Co_3O_4 nanoparticles synthesized at 300^{o}C in 1h.

Sample Name	Reaction Temperature (°C)	Reaction time (h)	Particle size range from TEM (nm)	BET surface area (m^2/g)	Density (g/cm^3)
*Co_3O_4-300-1	300	1	5 – 18	38.58(3)	6.2 (1)
Co_3O_4-400-0.5	400	0.5	12 – 20	14.37(3)	6.3(2)
Co_3O_4-600-0.5	600	0.5	75 – 150	2.65(6)	6.2(1)
Co_3O_4-800-0.5	800	0.5	200 – 400	1.59(2)	6.3(2)

The direct current (DC) susceptibility measurements were performed using a superconducting quantum interference device (SQUID-MPMS) magnetometer on about 60 mg of polycrystalline powder samples of Co_3O_4 nanoparticles protected in polycarbonate sample holder. The

temperature dependence magnetization under zero-field-cooled (ZFC) and field cooled (FC) conditions were measured between 2 K and 300 K for all samples with 100Oe applied field. The raw data were corrected for the sample holder contribution.

Specimens for thermal conductivity, electrical resistivity and thermopower measurements were obtained by consolidating fine powders of the synthesized Co_3O_4 nanoparticles under a dynamic vacuum of ~10^{-4} Torr. Pellets were fabricated using a uniaxial hot press by simultaneously applying a maximum pressure of 100 MPa and a maximum temperature of 900 ^{o}C. The samples were placed into a graphite die with an inner diameter of 10 mm and then sintered under vacuum (10^{-5} Torr). The final working set point of pressure (100 MPa) was first reached with a ramp of 2 MPa/min, followed by a hold of 4h while the temperature was still rising at a heating rate of 5^{o}C/min to 900 ^{o}C. The maximum temperature and pressure were kept for 1h to achieve higher strengthening and good compaction of the pellet. The sample was then cooled to room temperature at a cooling rate of 5^{o}C/min simultaneously while the pressure released (2MPa/min). The density of the resulting pellet was determined by measuring the dimensions and mass.

Thermal diffusivity data were measured using a Netzsch LFA 457 laser flash system. A pyroceram reference material was measured alongside each sample. Measurements were made under flowing N_2 gas (>30 mL/min) from 300 K to 775 K at increments of 25 K. C_p values for thermal conductivity calculations were extracted from the laser flash data. The instrument precision for the thermal diffusivity data is ±6%. Seebeck coefficient and electrical resistivity were measured simultaneously from 375 to 775 K under a low pressure of He atmosphere using a commercial ZEM-3 system from ULVAC-RIKO. The instrument precision for the electrical resistivity and Seebeck coefficient data is ±4%.

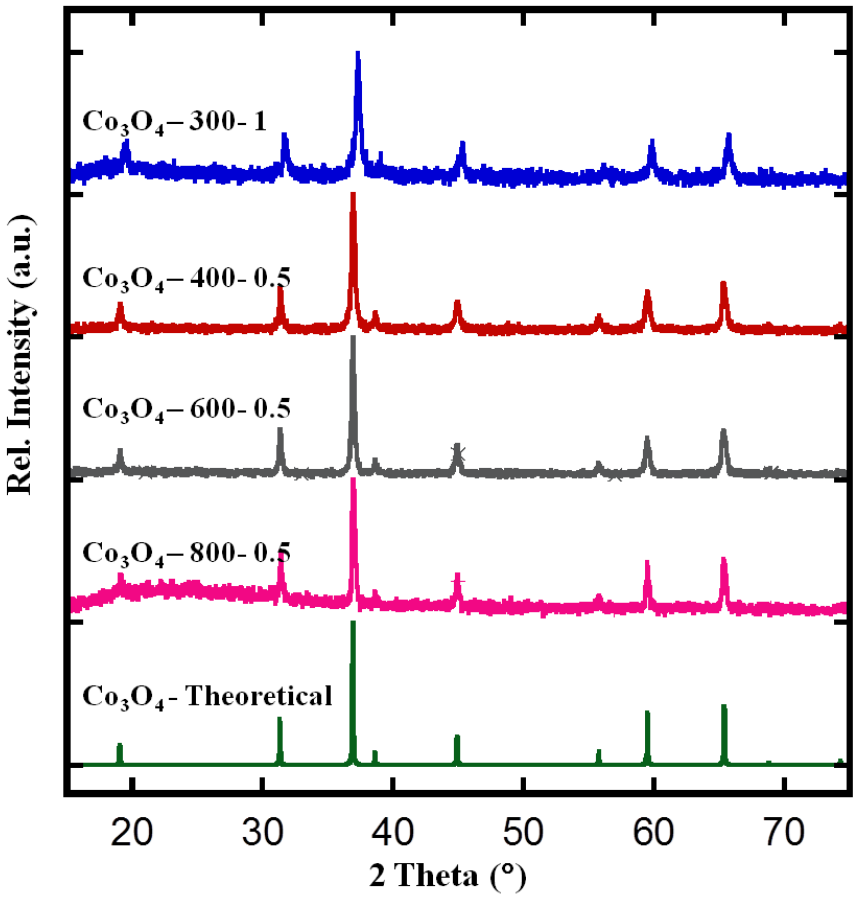

Figure 3.1 : X-ray powder diffraction patterns of Co_3O_4 nanoparticles synthesized at various temperatures. The theoretical pattern of Co_3O_4 is shown for comparison.

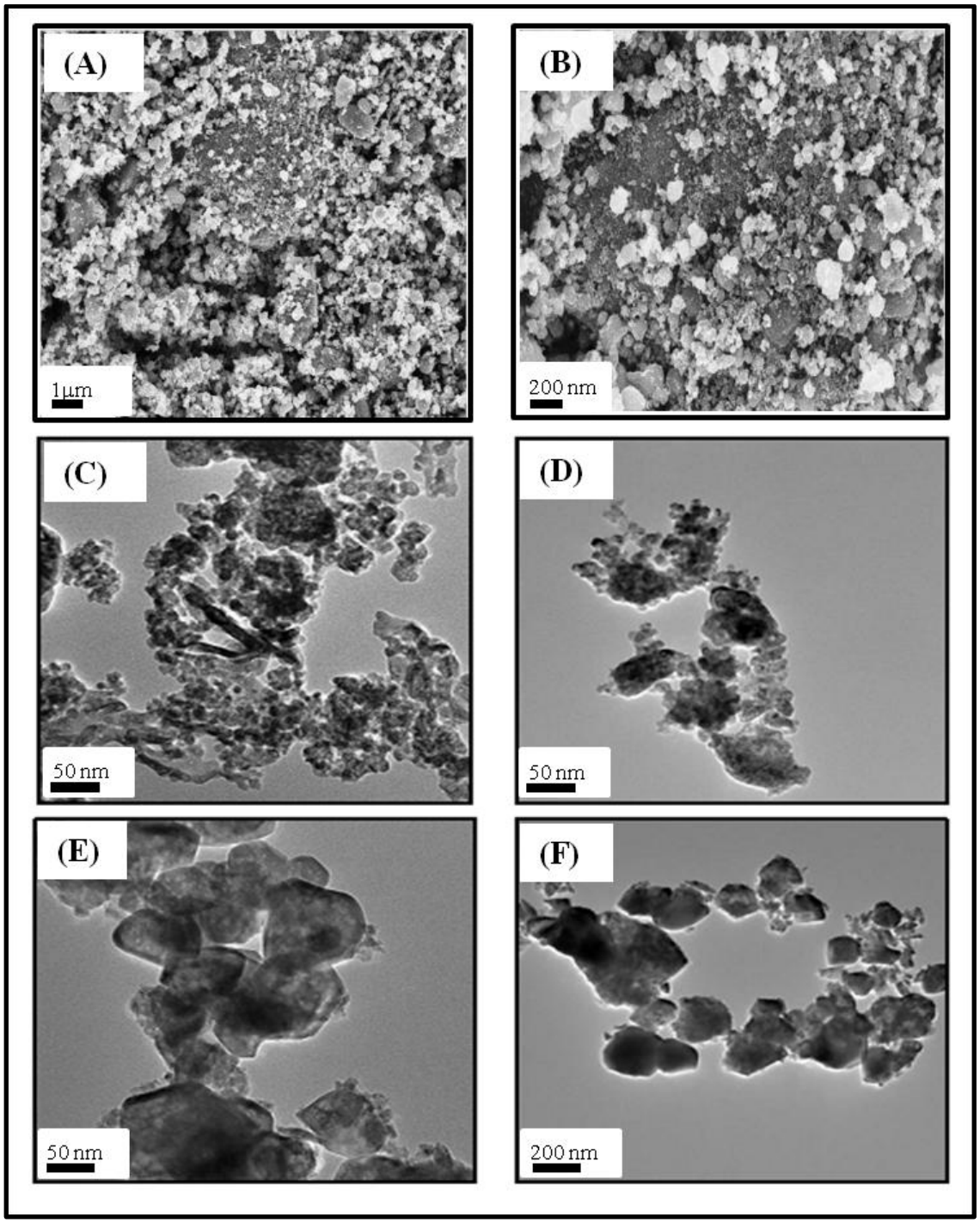

Figure 3.2 : Scanning electron microscope images of the Co_3O_4-300-1 sample taken at various regions (A and B). Selected transmission electron microscopy images of Co_3O_4 nanoparticles synthesized at: (C) 300 °C for 1h; (D) 400 °C for 0.5h; (E) 600 °C for 0.5h; (F) 800 °C for 0.5h

3.4 Results and discussion

Synthesis and characterization. Figure 3.1 shows the XRD patterns of Co_3O_4 nanoparticles synthesized by solution combustion method modified by varying the reaction ignition temperatures. All diffraction peaks on the patterns match nicely with the corresponding peak on the theoretical pattern of cubic Co_3O_4 (ICSD no. 150805), suggesting successful rapid synthesis of high pu-rity Co_3O_4 nanoparticles by the so-modified solution combustion method. No obvious additional peak corresponding to any other cobalt oxide phases such as CoO or Co_2O_3 could be detected in the powder patterns confirming the suitability of the solution combustion synthesis method for cost-efficient and rapid large scale production of Co_3O_4 nanoparticles. The well-resolved diffraction peaks on the XRD patterns of the as-synthesized Co_3O_4 nanoparticles (Fig. 3.1) reveals their excellent crystallinity. However, diffraction peaks on the XRD pattern of the sample synthesized at 300^o C (Co_3O_4-300-1) seem to be relatively wider than corresponding peak on the XRD patterns of samples synthesized at higher temperatures. This suggests a comparatively smaller particle size for the Co_3O_4-300-1 sample. It is important to note that attempt to reduce the reaction time to 30 min while maintaining the reaction ignition temperature at 300 °C resulted in an incomplete reaction with the formation of amorphous products. However, upon increasing the reaction ignition temperature to 400 °C and above, a complete reaction with the formation of highly crystalline Co_3O_4 nanoparticles could be achieved after 30 min. Figs.3. 2A and 3.2B show scanning electron microscopic (SEM) images of the Co_3O_4-300-1 sample taken at various locations within the specimen. It appears that Co_3O_4 nanoparticles resulting from the combustion method have non-uniform particle shape and a broad distribution of particle size within nanometer range. Transmission electron microscopy (TEM) study of the

Co_3O_4-300-1 specimen revealed that large fractions of the sample are agglomerates consisting of fine particles with size range between 5 and 18 nm (Fig. 3.2C). The specific surface area of 39 m^2/g measured for the Co_3O_4-300-1 sample using BET method is comparable to the value of 36 m^2/g previously reported for Co_3O_4 nanoparticles synthesized by solution combustion method [145,147]. For Co_3O_4 prepared at 400^o C in 30 min (Co_3O_4-400-0.5), the average particle size varies between 12 and 20 nm (Fig. 3.2D) and the BET specific surface area decreases to 14 m^2/g. Further increase in the reaction ignition temperature to 600 °C and 800 °C resulted in the formation of Co_3O_4 nanoparticles with substantially larger average size range (Figs. 3.2E and 3.2F) after 30 min and the BET specific surface areas is significantly reduced (Table 3.1). The density values of ~ 6.2(1) g/cm^3 measured for the synthesized cobalt oxide nanoparticles (Table1) are very similar to the reported bulk density value of 6.12 g/cm^3. The above described structural data strongly suggest successful synthesis of highly crystalline single phase Co_3O_4 nanoparticles in a relatively short time and our ability to tune the average particle size range by varying the reaction ignition temperature.

Magnetic Properties. To probe the effect of the reaction ignition temperature on the magnetic behavior of the synthesized Co_3O_4 nanoparticles, magnetic susceptibility data were collected under field cooled (FC) and zero-field cooled (ZFC) conditions. Figure 3 shows the temperature dependent ZFC and FC susceptibility curves of Co_3O_4 nanoparticles synthesized under various reaction ignition temperatures. Regardless of the synthesis conditions, the magnetic susceptibility gradually increases with decreasing temperature, reaches a maximum at temperatures between 20K and 40K and decrease with further cooling to 2K. This general shape of the temperature dependent susceptibility curves featuring a downturn at low temperatures suggests a dominant antiferromagnetic (AFM) ordering in the synthesized Co_3O_4 nanoparticles.

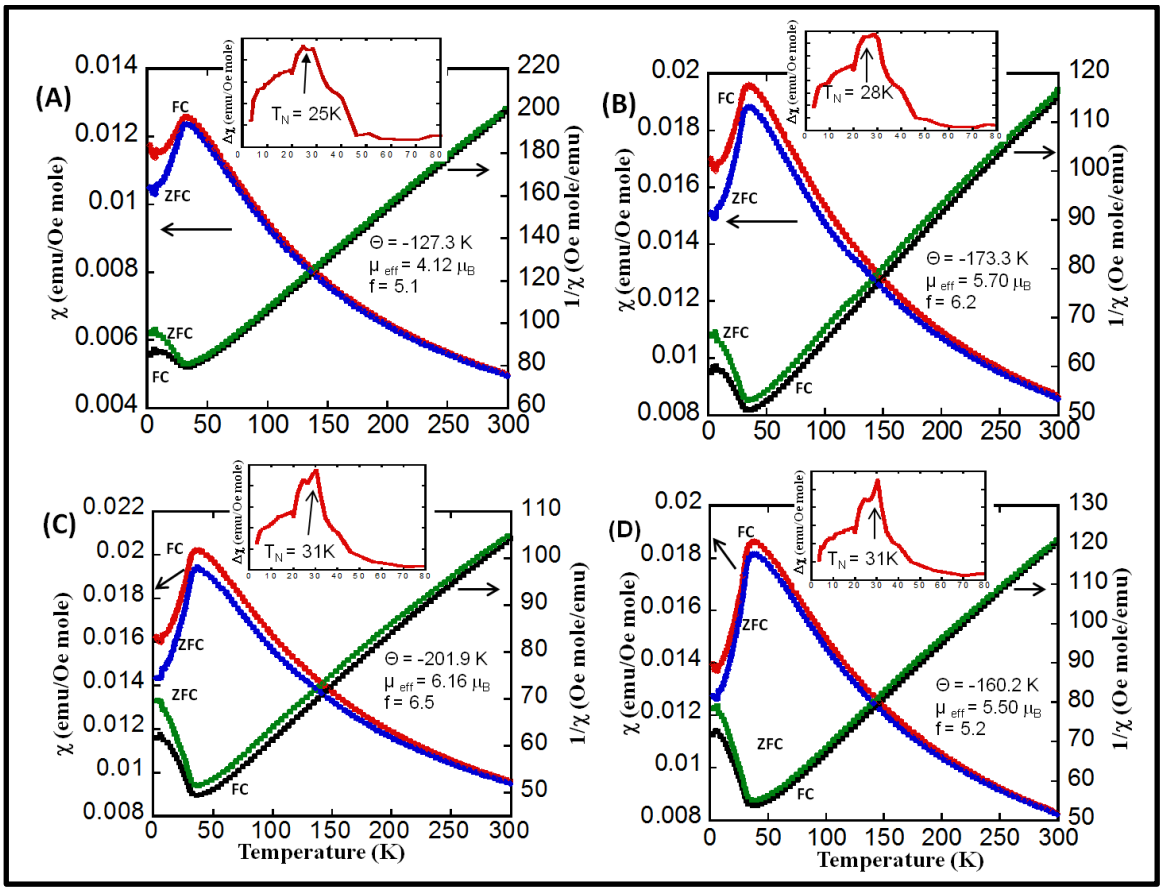

Figure 3.3 : Temperature dependence of the field-cooled (FC) and zero field-cooled (ZFC) magnetic susceptibility and inverse susceptibility of various Co_3O_4 samples under 100 Oe external applied fields. (A) Co_3O_4-300-1; (B) Co_3O_4-400-0.5; (C) Co_3O_4-600-0.5;(D)Co_3O_4-800-0.5

However, careful analysis of the susceptibility curves (see inset of Figs. 3.3A to 3.3D) revealed that the Néel temperature (T_N) at which the transition from the paramagnetic to the AFM ordering occurs increases with increasing reaction ignition temperatures. The observed T_N values are 25K for Co_3O_4-300-1, 28K for Co_3O_4-400-0.5, and 31K for Co_3O_4-600-0.5 and Co_3O_4-800-0.5 samples. These values are significantly lower than the T_N = 40K reported for bulk Co_3O_4 [150,151]. As shown above, the average particle size ranges of the synthesized Co_3O_4 nanoparticles

decrease with decreasing reaction ignition temperatures. Therefore, the observed gradual decrease in the T_N with decreasing reaction ignition temperature can be associated with the reduction in the size of the synthesized Co_3O_4 nanoparticles. This result is consistent with previously reported decrease in the T_N of Co_3O_4 nanoparticles due to finite size effects [142,148,149].

The temperature dependent inverse susceptibility data above T_N for all Co_3O_4 nanopaticle samples follow the Curie-Weiss law. The Weiss constants and the effective magnetic moments extracted from the linear fits of the inverse susceptibility data are reported in Fig. 3.3. The large negative values of the Weiss constant (Co_3O_4-300-1: θ = -127.3 K; Co_3O_4-400-0.5: θ = -173.3 K; Co_3O_4-600-0.5: θ = -201.9 K; and Co_3O_4-800-0.5: θ = -160.2 K) indicate a strong AFM ordering in the Co_3O_4 samples. However, the large difference in the magnitude of the Weiss constant in various samples suggests some variations in the strength of the AFM exchange interactions with the alteration of the reaction ignition temperature. Interestingly, the effective magnetic moments calculated from the linear fits of the inverse susceptibility curves (4.12 μ_B for Co_3O_4-300-1; 5.70 μ_B for Co_3O_4-400-0.5; 6.16 μ_B for Co_3O_4-600-0.5; and 5.50 μ_B for Co_3O_4-800-0.5) are larger than the spin only effective magnetic moment of 3.9 μ_B expected for Co^{2+} (S = 3/2) in Co_3O_4 with normal spinel structure. In addition, the effective magnetic moment of the synthesized Co_3O_4 nanoparticles increases with increasing reaction ignition temperature from 300 °C to 600 °C, reaches a maximum for the Co_3O_4-600-0.5 sample and decreases with further increase of the temperature to 800 °C. The observed simultaneous change in the Weiss constants and the effective magnetic moments suggest that the variation of the reaction ignition temperatures probably induces a new distribution of Co^{2+} and Co^{3+} in the various metal positions in the crystal structure of Co_3O_4 spinel, which ultimately leads to various degrees of competing magnetic interactions in the samples. The presence of some degrees of frustration? in the dominant AFM

ordering in Co_3O_4 nanoparticle samples can also be assessed qualitatively by the divergence of the ZFC and FC susceptibility curves at temperatures above T_N (Fig. 3.3). In non-frustrated AFM materials, a clear overlap of the FC and ZFC susceptibility curves is generally observed at temperatures above the Néel transition temperature. Quantitatively, a measure of the degree of geometrical spin-frustration is given by the frustration parameter $f = |\theta|/T_N$, where T_N is the cooperative ordering transition temperature and $f > 5$ indicating strong spin frustration [152,153]. One can see from the values of θ, f and μ_{eff} (Fig. 3) that the strength of AFM coupling, the degree of spin frustration, as well as the magnitude of the effective magnetic moments in various Co_3O_4 nanoparticle samples depend strongly on the reaction ignition temperatures. Co_3O_4 nanoparticles synthesized at 300 °C showed the smallest degree of spin frustration (f = 5.1) and the effective magnetic moment of 4.12 μ_B is only 6% higher than the theoretical value of 3.9 μ_B expected for Co^{2+} in Co_3O_4 with normal spinel structure. When the reaction ignition temperature is increased to 400 °C, the degree of spin frustration of the AFM spin state also increased (f = 6.2) along with the Weiss constant (θ = -173.3K) as well as the effective magnetic moment per formula unit (5.70 μ_B). The highest degree of spin frustration (f = 6.5) and the largest Weiss constant (θ = -201.9K) were observed for Co_3O_4 nanoparticles synthesized at 600 °C and the resulting effective magnetic moment of 6.16 μ_B is 59% higher than the expected value of 3.9 μ_B for Co^{2+} in Co_3O_4 spinel.

From the above analysis, it appears that the magnetic behavior of Co_3O_4 nanoparticle samples is not just sensitive to the average particle size as demonstrated in numerous studies [142,148,149], but is also strongly influenced by the temperature of the synthesis. One possible rationalization of the observed change in the magnetic behavior with the synthesis temperature can be obtained by considering possible change in the distribution of Co^{2+} and Co^{3+} cations in the crystal structure of

Co_3O_4 nanoparticles. Co_3O_4 crystallizes with a normal spinel structure A- with general formula $[A]^{tet}[B_2]^{oct}O_4$, where $[A]^{tet}$ is the tetrahedral A-site occupied by one Co^{2+} ion and $[B_2]^{oct}$ is the octahedral B-sites occupied by two Co^{3+} ions. Recent studies suggested the possibility of charge transfer between Co^{2+} at A-site and Co^{3+} at B-sites in the structure of Co_3O_4 nanoparticle upon application of external magnetic fields[154] or high pressures[155]. Likewise, disordered distribution of Co^{2+} and Co^{3+} ions in various metallic A and B sites is anticipated at sufficiently high synthesis temperature (above 300 °C in the present study) due to increased thermal vibration of atoms within the crystal lattice, which promotes atomic diffusion between the A and B sites. Therefore, inverse spinel structure, $[(Co^{2+})_{1-x}(Co^{3+})_x]^{tet}[(Co^{2+})_x(Co^{3+})_{2-x}]^{oct}O_4$, with various inversion degrees (x) can be obtained depending on the reaction ignition temperature. Within this picture, the overall effective magnetic moment of the resulting Co_3O_4 nanoparticle can be correlated to the inversion degree, x (i.e. the fraction of Co^{3+} located within the tetrahedral A-site in the inverse spinel structure of Co_3O_4 nanoparticle). In bulk Co_3O_4 with normal spinel structure, the effective magnetic moment per formula unit ($4.14\mu_B$) [151] originate solely from Co^{2+} ($3d^7$) at the tetrahedral A-site in high spin state ($e_g^4t_{2g}^3$, S = 3/2) and the Co^{3+} ($3d^6$) atom located within the octahedral B-sites in low spin state ($t_{2g}^6e_g^0$, S = 0) has no magnetic moment. However, in the case of diffusion of a fraction (x) of Co^{3+}($3d^6$) ions into the tetrahedral site, the new spin distribution $e_g^3t_{2g}^3$ (high spin state)[151] leads to a total spin $S_1 = 2x$, whereas the diffusion of Co^{2+}($3d^7$) into the octahedral B-site maintains the high spin state electronic

configuration $t_{2g}^5e_g^2$ resulting in a total spin $S_2 = 3x/2$. Therefore, the overall effective magnetic moment of Co_3O_4 inverse spinel, $[(Co^{2+})_{1-x}(Co^{3+})_x]^{tet}[(Co^{2+})_x(Co^{3+})_{2-x}]^{oct}O_4$, with various degrees of inversion (x) can be estimated using the equation: $\mu_{effective}(\mu_B) = \mu(Co^{2+}) + \mu(Co^{3+}) = 3.87 + 2[2x(1+2x)]^{1/2}$.

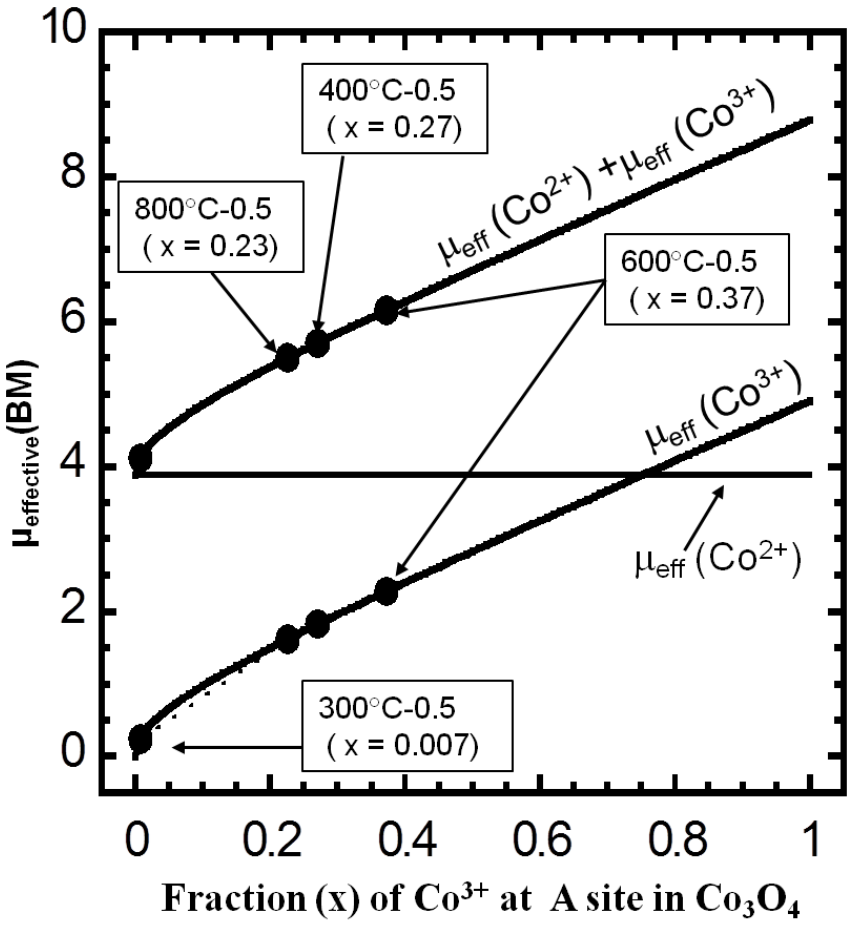

Figure 3.4: Effective magnetic moment per formula unit as a function of the inversion degree x (amount of Co^{3+} located within the tetrahedral A sites in the Co_3O_4 structure) along with the variation in individual contribution from the Co^{2+} and Co^{3+} ions.

Fig. 3.4 shows the plot of total effective magnetic moment per formula unit of Co_3O_4 inverse spinel along with contributions from Co^{2+} and Co^{3+} as a function of the inversion degree x. It can be observed that the overall effective magnetic moment of the synthesized Co_3O_4 nanoparticles is larger than the expect value because of the diffusion of a small fraction (x) of Co^{3+} into the tetrahedral A-sites, which induces a change in its spin state from low-spin (S = 0) to high spin (S = 2). For a fully inverse spinel structure of Co_3O_4 (x = 1), the spin only effective magnetic moment anticipated from the equation given above is $8.78\mu_B$. Along this line, a projection of experimental effective magnetic moments extracted from the susceptibility data on the theoretical curve (Fig. 3.4) can enable the estimation of the inversion degree (x) in Co_3O_4 nanoparticles synthesized under various reaction ignition temperatures. For instance, the smallest effective magnetic moment of 4.12 μ_B for the Co_3O_4-300-1sample corresponds to the mixing of ~ 0.007 Co^{3+} and 0.993 Co^{2+} ions into the tetrahedral A-site leading to the structural formula $[(Co^{2+})_{0.993}(Co^{3+})_{0.007}]^{tet}[(Co^{2+})_{0.007}(Co^{3+})_{1.993}]^{oct}O_4$ (x = 0.007), which is very close to the normal spinel structure. Likewise, the largest effective magnetic moments of 6.16 μ_B observed for the Co_3O_4-600-0.5 sample arises from the mixing of 0.37 Co^{3+} and 0.63 Co^{2+} ions into the tetrahedral A-site resulting in the inverse spinel structural formula $[(Co^{2+})_{0.63}(Co^{3+})_{0.37}]^{tet}[(Co^{2+})_{0.37}(Co^{3+})_{1.63}]^{oct}O_4$ (x = 0.37). One important conclusion from the above discussion is that the large effective magnetic moments (compared to the theoretical value of 3.9 μ_B) obtained for Co_3O_4 in numerous studies as well as the discrepancy between the reported values [142,151,154] are likely associated with changes in the local distribution of Co^{2+} and Co^{3+} in the crystal structures, which in turn depends on the temperature of the synthesis, rather than originating from additional contributions from the orbital moment [142,151].

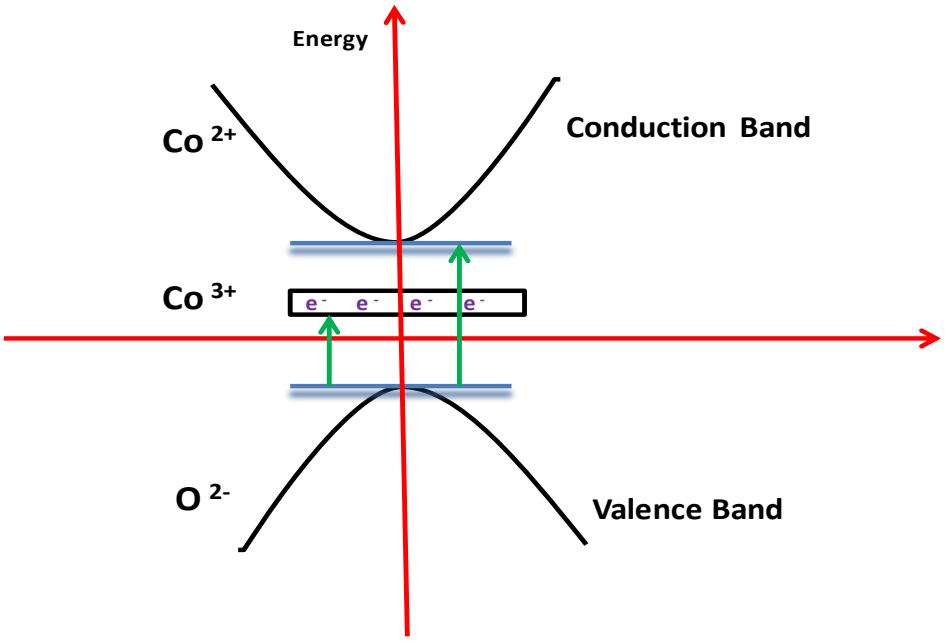

Figure 3.5: Schematic representation of the band structure of Co_3O_4

Optical Measurements. Co_3O_4 i.e. $Co^{2+}[Co^{3+}]_2O_4$ is known to crystallize in a cubic normal spinel structure which contains the cobalt ions in two different oxidation states(Figure 3.5) . The Co^{+2} $[3d^7 (4t_{2g}3e_g)]$ is located at tetrahedral site bearing a high spin [S = 3/2] whereas,Co^{+3} $[3d^6 (6t_{2g}0e_g)]$ is located at octahedral site with a low spin [S=0].The optical absorption of Co_3O_4 nanoparticles within the wavelength range of 200 nm - 800 nm has been investigated. Figure 6 shows plots of $(\alpha h\upsilon)^2$ as a function of photon energy (hν in eV) for Co_3O_4 nano particles at different synthesizing temperature (300°C - 800°C). The absorption band gap energy can be determined by the following equation[156] : $(\alpha h\upsilon)^2 = B(h\upsilon - E_g)$;Where hυ is the energy of the photon, α is the absorption coefficient, B is a constant relative to the inherent property of the material and n is a value that depends on the nature of transition (2 for a direct allowed transition). Extrapolation of these curves on the energy axis depicts the optical band gap of the materials. From Fig. 3.6, presence of two slopes has been observed. The first bandgap can be

associated to $O^{2-} \rightarrow Co^{2+}$ charge-transfer process while the second one can be ascribed to $O^{2-} \rightarrow Co^{3+}$ charge transfer[157-160].The band gap of Co^{+3} for all the samples lies within the range 1.5-1.7eV whereas, for Co^{+2} it lies within 2.00-2.15eV compared to the previously reported works[161-163].

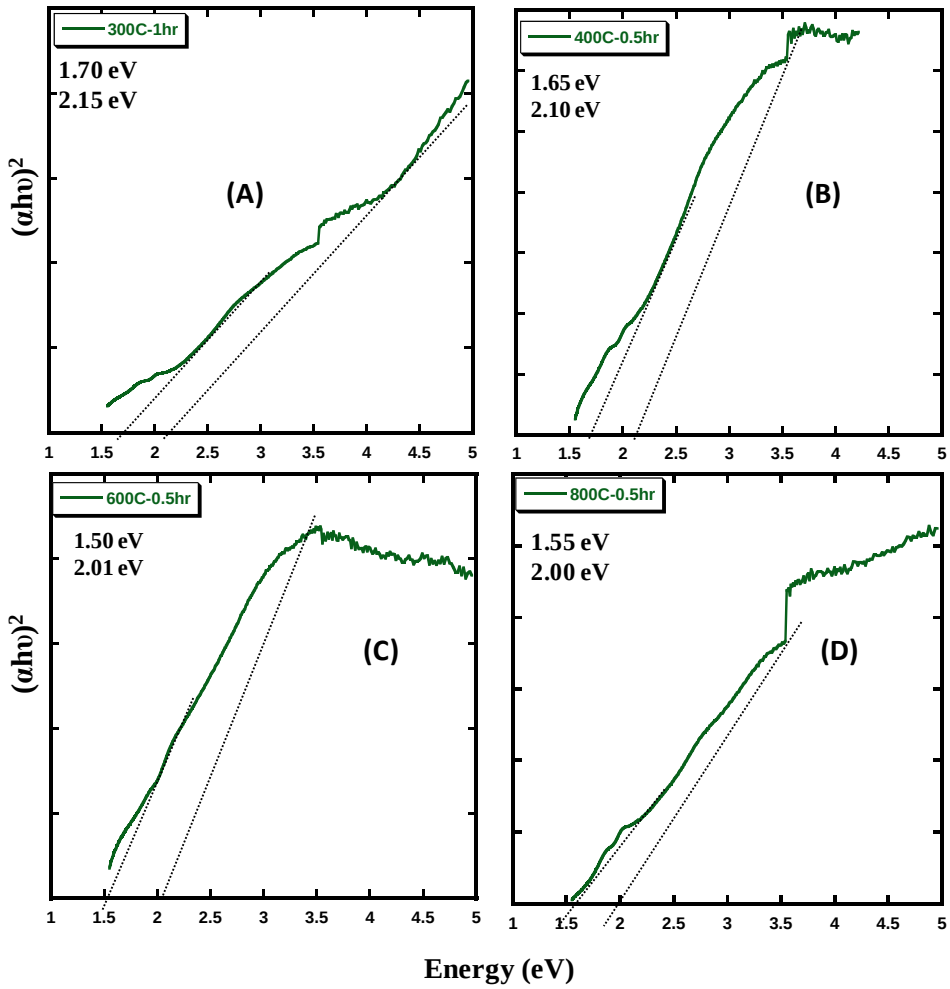

Figure 3.6: Plots of $(\alpha h\upsilon)^2$ as a function of photon energy (eV) for Co_3O_4 nano particles synthesized at (A) 300°C-1 hr;(B) 400°C-0.5hr;(C) 600°C-0.5 hr and (D) 800°C-1 hr

Thermoelectric properties. To assess the effect of (1) change in the nanoparticle size range and (2) disorder in the distribution of Co^{2+} and Co^{3+} within the crystal structure of the synthesized Co_3O_4 nanoparticles on their thermoelectric behavior, we have performed high temperature measurements of the thermal conductivity, electrical conductivity and thermopower on various hot press pellet samples. Fig. 3.7A shows the temperature dependence of the thermopower of various Co_3O_4 samples. All samples showed positive thermopower values in the whole temperature range indicating holes as majority charge carriers. At 425 K, the thermopower of various samples increases from 150 μV/K for the Co_3O_4-400-0.5 sample to 200 μV/K for the Co_3O_4-300-1 and Co_3O_4-600-0.5 samples, and further increases to 250 μV/K for the Co_3O_4-800-0.5 sample. Regardless of the synthesis conditions, the thermopower of all samples gradually increase with rising temperature reaching maximum values of 325 μV/K (Co_3O_4-400-0.5), 360μV/K (Co_3O_4-300-1 and Co_3O_4-600-0.5), and 450μV/K (Co_3O_4-800-0.5) at 775K. Surprisingly, the Co_3O_4-300-1 and Co_3O_4-600-0.5 samples showed similar thermopower values in the whole temperature range, whereas lower thermopower values are observed for the Co_3O_4-400-0.5 sample and the largest values are obtained for the Co_3O_4-800-0.5 sample. The temperature dependent electrical conductivity of the synthesized Co_3O_4 nanoparticles is shown in Fig. 7B. The electrical conductivity of all samples increases exponentially with rising temperature suggesting that the synthesized Co_3O_4 nanoparticles are p-type semiconductors. Regardless of the temperature, similar values of the electrical conductivity ranging from 0.25 S/cm at 425K to 2.8 S/cm at 775K were observed for the Co_3O_4-300-1, Co_3O_4-400-0.5, and Co_3O_4-600-0.5, whereas lower electrical conductivity values (ranging from ~0.02 S/cm at 300K to and 1.5 S/cm at 775 K) were measured for the Co_3O_4-800-0.5 sample.

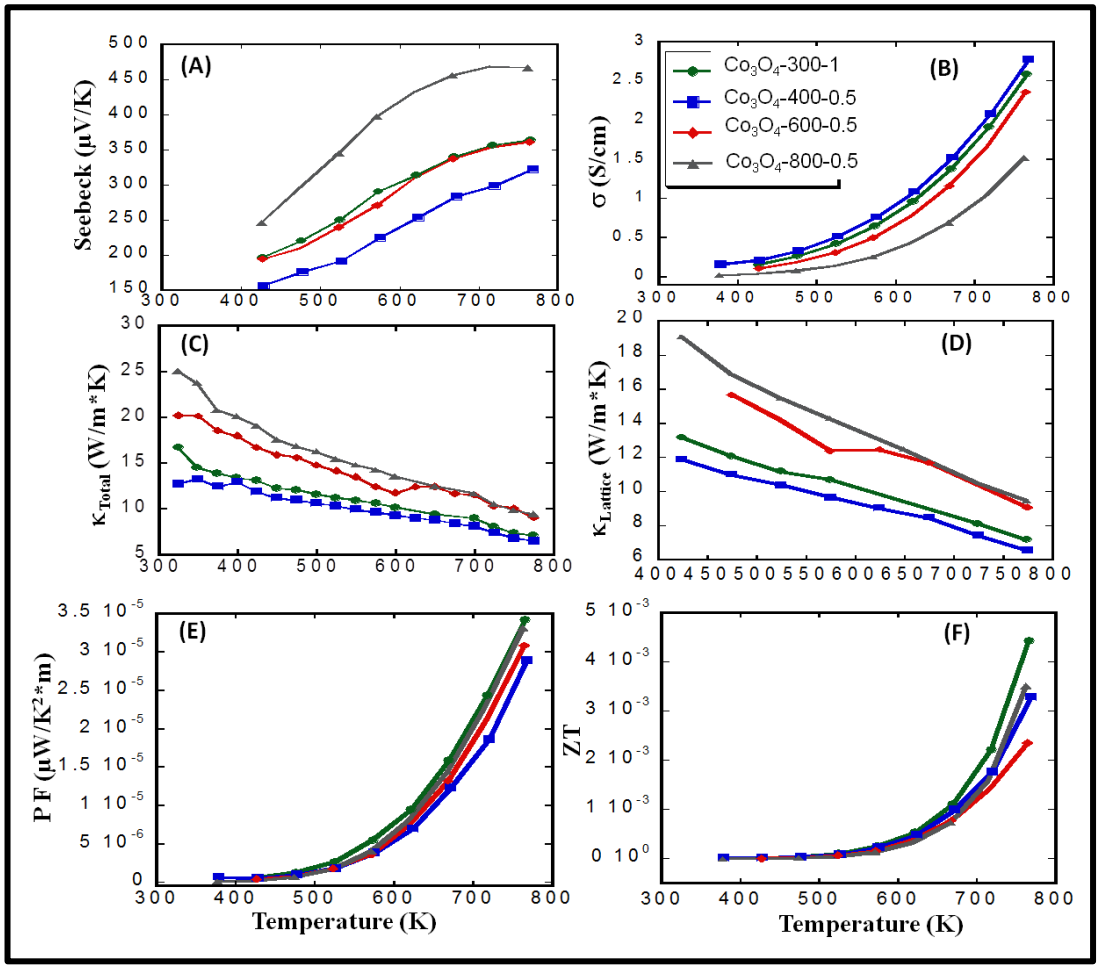

Figure 3.7 : Temperature dependence of the electronic and thermal transport properties of Co_3O_4 nanoparticles. (A) Seebeck coefficient; (B) Electrical conductivity; (C) Total thermal conductivity; (D) Lattice thermal conductivity; (E) Power factor (PF);(F) ZT

To understand the origin of the observed variations in the thermopower and electrical conductivity values of various Co_3O_4 samples, we have analyzed the electrical conductivity curves using the Arrhenius law ($\sigma \sim \exp(E_g/2k_BT)$ and electronic band gaps for various samples

were extracted from linear fit of the ln(σ) versus $1/2k_BT$. It was found that the Co_3O_4-300-1 and Co_3O_4-600-0.5, samples have a similar band gap (~0.50 eV) which may explain the similarity in their electrical conductivity and thermopower at all temperatures. The lowest band gap (~0.37 eV) was observed for the Co_3O_4-400-0.5 and the largest band gap of ~0.56 eV was obtained for the Co_3O_4-800-0.5 sample. This change in the electronic band gap of various Co_3O_4 samples is consistent with the observed trend on electrical conductivity and thermopower curves. The change in the band gap is likely associated with the variation in (1) the average particles size and/or (2) the distribution of Co^{2+} and Co^{3+} at the A and B sites within the crystal structure due to the alteration of the reaction ignition temperature.

Figs. 3.7C and 3.7D show the temperature dependence of the total and lattice thermal conductivities of various Co_3O_4 samples. Thermal conductivities were calculated from the diffusivity and Cp data extracted from the measurement using laser flash method. The Cp data were comparable to the previously reported value [164]. Regardless of the temperature, the total thermal conductivity of the synthesized Co_3O_4 samples gradually increases with increasing reaction ignition temperature. For example, the total thermal conductivity values at 300K are 12.8 W/mK, 16.8 W/mK, 20.2 W/mK, and 25 W/mK for the Co_3O_4-300-1, Co_3O_4-400-0.5, Co_3O_4-600-0.5, and Co_3O_4-800-0.5 sample, respectively. A similar trend was observed for the lattice thermal conductivity (Fig. 3.7D). These experimental results are consistent with the expected enhancement of phonon scattering due to increase density of grain boundaries arising from the reduction of the average particle sizes. The thermal conductivity of all samples decreases with increasing temperature reaching values as low as 6.6 W/mK at 775K for the Co_3O_4-300-1 sample. The temperature dependence of the power factor (PF) and figure of merit (ZT) calculated from the above electronic and thermal transport data are shown in Figs. 3.7E and

3.7F. Low PF values are observed for all Co_3O_4 nanoparticle samples due to their poor electrical conductivity. Regardless of the synthesis conditions, the PF increases rapidly with increasing temperature from ~0.68 $\mu W/K^2m$ at 300K to 35$\mu W/K^2m$ at 775K. The combination of low PF and high total thermal conductivity of the synthesized Co_3O_4 nanoparticle samples results in low ZT values ranging from 4×10^{-5} at 300K to 4.4×10^{-3} at 775K.

3.5 Conclusions

In summary, we have demonstrated the ability to produce in a relatively short time via by solution combustion method, single phase Co_3O_4 nanoparticles with various average particle sizes by tuning the reaction ignition temperature between 300 °C and 800 °C. The particle size range of the resulting Co_3O_4 nanoparticles increases from 5nm -18 nm for the Co_3O_4-300-1 sample to 200 – 400 nm for the Co_3O_4-800-0.5 sample. Magnetic susceptibility measurements revealed a gradual increase in the Néel temperature of Co_3O_4 nanoparticles from T_N = 25 K for the Co_3O_4-300-1 sample to T_N = 31 K for the Co_3O_4-800-0.5 sample. These values are significantly lower than the value of ~40 K reported for bulk Co_3O_4. Large effective magnetic moments (μ_{eff}) ranging from 4.12 μ_B (Co_3O_4-300-1) to 6.16 μ_B (Co_3O_4-600-0.5) were calculated from the linear fits of the inverse susceptibility data using the Curie-Weiss law. This substantial increase in the μ_{eff} of various samples when compared to the value of 3.9 μ_B expected for Co^{2+} in Co_3O_4 normal spinel structure was ascribed to the disordered distribution of Co^{2+} and Co^{3+} in the tetrahedral A-site and the octahedral B-sites in the structure of the synthesized Co_3O_4 nanoparticles. Thermal and electronic transport studies indicated a gradual reduction in the thermal conductivity of various Co_3O_4 samples upon decreasing the reaction ignition

temperature. A strong variation in the electrical conductivity and thermopower of various Co_3O_4 samples was also observed. Changes in the electronic properties were associated with alterations in the electronic band gap due to various degrees of Co^{2+}/Co^{3+} disorder in the structure of Co_3O_4, which in turn depend on the reaction ignition temperature.

Chapter 4

STUDIES ON THERMOELECTRIC PROPERTIES HALF-HEUSLER NANOCOMPOSITES

4.1 Overview

This chapter describes synthesis and characterization of different composition of half-Heusler alloys(both p-type and n-type) The thermopower (S) and electrical conductivity (σ) in conventional semiconductors are coupled adversely through the carriers' density (n) making it difficult to achieve meaningful simultaneous improvements in both electronic properties through doping and/or substitutional chemistry. Here, the effectiveness of coherently embedded full-Heusler (FH) quantum dots (QDs) has been discussed in tailoring the density, mobility and effective mass of charge carriers in the half-Heusler (HH) matrix. The concept of band structure engineering near the Fermi level through atomic-scale alteration of a bulk semiconductor crystal structure using coherently embedded intrinsic semiconducting quantum dots provides a unique opportunity to manipulate the transport behavior of the existing ensembles of carriers within the semiconducting matrix. Here we show that in situ growth of coherent nanometer-scale full-Heusler (FH) quantum dots (FH-QDs) within the p-type half-Heusler (HH) matrix induces a drastic decrease of the effective carrier density within the HH/FH-QD nanocomposites at 300K

followed by a sharp increase with rising temperature. This behavior is associated with the formation of staggered heterojunctions with a valence band (VB) offset energy, ΔE at the HH/FH phase boundaries. The energy barrier (ΔE) discriminates existing holes with respect to their energy by trapping low energy (LE) holes, while promoting the transport of high energy (HE) holes through the VB of the FH-QDs. This results in surprisingly large increases in the mobility and the effective mass of HE carriers contributing to electronic conduction. The simultaneous reduction in the density and the increase in the effective mass of carriers resulted in large enhancements of the thermopower whereas; the increase in the mobility minimizes the drop in the electrical conductivity. This strategy to manipulate the transport behavior of existing ensembles of charge carriers within a bulk semiconductor using QDs is very promising and could pave the way to a new generation of high figure of merit thermoelectric materials.

4.2 Background survey

One of the major roadblocks to large improvements in the thermoelectric figures of merit ($ZT = T(\sigma \times S^2)/\kappa$, where κ is the thermal conductivity, T is the absolute temperature and $\sigma \times S^2$ is the power factor (PF)) of leading thermoelectric materials such as the Bi_2Te_3, PbTe, $CoSb_3$ and half-Heusler (HH) based systems remains the difficulty of making meaningful simultaneous improvements in both the electrical conductivity (σ) and thermopower (S) of these materials through doping and/or substitutional chemistry [4-6,20,22-25,46,79,81,86-88,91,94,165-176]. In conventional semiconductors, both of these transport parameters are inversely coupled through the carrier concentration, n. For heavily doped cubic semiconductors such as the half-Heusler compounds, the thermopower (S) and electrical conductivity (σ) can be expressed as $S = [(8\pi^2(k_B)^2)/3eh^2]m^*T(\pi/3n)^{2/3}$ (for a parabolic band model in the energy independent scattering

approximation [177]); and $\sigma = ne\mu$ (k_B is the Boltzmann constant, e is the carrier charge, h is Planck's constant, m* is the effective mass of the charge carrier, n is the carrier concentration and μ is the mobility of charge carrier). Therefore, the maximization of one parameter by tuning the carrier concentration (n) via doping and/or substitutional chemistry inevitably results in the minimization of the other. This longstanding roadblock to the fabrication of high performance thermoelectric materials (ZT ~ 3), has therefore severely delayed the ability to realize cost effective and "clean" solid-state energy conversion devices capable of competing with traditional mechanical energy conversion systems. Among various strategies employed to enhance the ZT of traditional and emerging thermoelectric materials, the concept of nanostructuring as an effective means to achieve drastic reductions in the lattice thermal conductivity (κ_L) while minimizing any adverse impact on the PF has dominated thermoelectric research over the past 15 years. As a result, mechanisms by which phonons are scattered at matrix/inclusion interfaces are now better understood [5,6,22-25,169-172]. Unfortunately, thermal conductivity reduction alone cannot boost the ZT of most thermoelectric materials systems to the targeted goal of ZT ~ 3 and one must now explore means to combine significant decreases in κ with meaningful increases in the PF. Moreover, the gains in the PF must originate from a large increase in S as opposed to a large increase in σ if the target goal of ZT ≥ 3 is to be achieved. This is due to the fact that by increasing σ, one inevitably increases the electronic part of κ, while an increase in S does not directly affect κ. It is therefore imperative to design and implement innovative concepts that could lead to large enhancements in the PF through (1) significant increases in S while mitigating losses in σ or (2) significant increases in both S and σ, simultaneously with large reductions in κ. Recently introduced concept of atomic scale structural engineering of thermoelectrics (ASSET) has been proved to be an important method to boost the thermopower

and carrier mobility within a bulk semiconducting matrix simultaneously with a drastic reduction in the thermal conductivity [178,179]. Bulk nanocomposites resulting from the ASSET approach are semiconductors with integrated nanostructures (SINs). Here, the semiconducting matrix and the embedded sub-ten nanometer range inclusions form highly coherent atomic-scale phase boundaries. In this work, ASSET approach has been used for both the p-type and n-type half-Heusler matrix (MgAgAs structure type; space group: F-43m) with full-Heusler inclusions ($MnCu_2Al$ structure-type; SG: Fm-3m) of general compositions $Ti_{0.5}Hf_{0.5}Co_{1+z}Sb_{09}Sn_{0.1}$ ($0 \leq z \leq 0.1$) and $Ti_{0.5}Hf_{0.5}Ni_{1+z}Sn_{0.975}Sb_{0.025}$ ($0 \leq z \leq 0.1$) that the coherent phase boundaries between the matrix and inclusion phases govern the charge carriers transfer processes across the matrix/inclusion interfaces. We found that careful manipulation of the chemistry and structure of the matrix/inclusion phase boundaries can lead to an effective enhancement in the thermopower and carrier mobility within the HH matrix simultaneously with large reductions in the thermal conductivity without severe losses in the electrical conductivity [178,179]. Our initial report on the n-type $Zr_{0.25}Hf_{0.75}Ni_{1+x}Sn$ and $Zr_{0.25}Hf_{0.75}Ni_{1+x}Sn_{0.975}Bi_{0.025}$, systems [178] has sparked a fast growing research interest on the application of similar concept to various combinations of HH/FH compositions as well as other thermoelectric material systems [4,180-188].

4.3 Experimental

4.3.1 Synthesis

p-type $Ti_{0.5}Hf_{0.5}Co_{1+x}Sb_{0.9}Sn_{0.1}$ nanocomposites (x = 0, 0.04, 0.05, 0.06, 0.07, 0.08) consisting of a bulk half-Heusler (HH) matrix with nominal composition $Ti_{0.5}Hf_{0.5}CoSb_{0.9}Sn_{0.1}$ and various mole fractions of full-Heusler (FH) inclusions, were synthesized via liquid state mediated solid-state reactions of high purity elemental powders (Ti, Hf, Sn, Sb and Co) in the desired

stoichiometry. A similar method was employed for the n-type composition $Ti_{0.5}Hf_{0.5}Ni_{1+x}Sn_{0.975}Sb_{0.025}$ **(**x= 0, 0.005, 0.01, 0.04, 0.08**).** Approximately 5g of the starting compositions containing various fractions of Co were thoroughly mixed under Ar atmosphere using an agate mortar and pestle to improve homogeneity. The mixture was sealed in a silica tube under a residual pressure of ~ 10^{-4} Torr and heated at 1173K for 14 days including the temperature ramping stage. The resulting products were consolidated into pellets at 900^{o}C under an applied pressure of 100 MPa using a uniaxial hot press. Detailed densification procedures are described elsewhere [41,43,44]. The relative densities of the pressed pellets were obtained by dividing the geometrical density (calculated using the pellet's dimension and mass) by the "true" density of the as-synthesized polycrystalline powder, measured using He gas pycnometry on a Micromeritics Accupyc II 1340. The relative density of all hot pressed pellets was above 95%.

4.3.2 Characterization

The structures and microstructures of the synthesized p-type and n-type (HH(1-x)/FH(x)) nanocomposites were respectively investigated by powder X-ray diffraction using a monochromated CuK_{α} radiation, high-resolution transmission electron microscopy (HRTEM JEM3100F), and spherical aberration corrected scanning transmission electron microscopy (Cs-corrected STEM, JEOL JEM2100F). Details on TEM sample preparation are described elsewhere [41,43]. The analytical x-ray energy-dispersive spectroscopy (EDS) line-scan was performed with an EDAX detector to examine the atomic distribution of all constituent elements between the FH and HH phases for p type composite. Selected area electron diffraction (SAED) photographs of selected specimens were used for the identification of both FH and HH phases. Seebeck coefficient and electrical resistivity were measured simultaneously from room temperature to 500°C under a low pressure He atmosphere using a commercial ZEM-3 system

from ULVAC-RIKO. The instrument precision for the electrical resistivity and Seebeck coefficient data is ±4%. The thermal conductivity was calculated from the thermal diffusivity data measured by the laser flash method (LFA-457 from Netzsch) from 20°C to 500°C under flowing N_2 gas (>30 mL/min). The instrument precision for the thermal diffusivity data is ±6%. A Pyroceram reference material was measured alongside each sample and C_p values for thermal conductivity calculations were extracted from the laser flash data. The electrical conductivity data were combined with the Hall coefficient measurements to evaluate and extract accurate information on the temperature dependence of the carrier density and the mobility of charge carriers in the nanocomposites. The Hall coefficient data were measured in the temperature range from 300K to 775K under the magnetic field of 1T using a large Oxford air-bore superconducting magnet cryostat that accommodates a small tubular oven and a Hall insert. The instrument uncertainty for Hall coefficient data is ±5%.

4.4 Thermoelectric Properties

Thermoelectric performance of p-type $Ti_{0.5}Hf_{0.5}Co_{1+x}Sb_{0.9}Sn_{0.1}$ (HH(1-x)/FH(x)) nanocomposites

Here, we extend the ASSET concept for the first time to the p-type $Ti_{0.5}Hf_{0.5}Co_{1+x}Sb_{0.9}Sn_{0.1}$ HH/FH nanocomposite systems. It has been found that nanometer scale inclusions with FH structure coherently embedded within the crystal lattice of the p-type HH matrix ($Ti_{0.5}Hf_{0.5}Co_{1+x}Sb_{0.9}Sn_{0.1}$) greatly alter the electronic transport behavior of the existing ensemble of free charge carriers within the HH matrix. For instance, starting from a heavily doped HH matrix with temperature-independent carrier concentration, embedding various fractions of FH inclusions led to a gradual decrease of the effective carrier density at 300K. Interestingly, the carrier density rapidly increases with rising temperature and asymptotically tends to the carrier

density of the nanostructure-free HH matrix. The observed large reductions in the effective carrier density within the HH/FH nanocomposites at 300K result in simultaneous increase in the thermopower (S) and the carrier mobility (μ). Surprisingly, the large increase in the thermopower is maintained at high temperatures, even for the HH/FH nanocomposites showing similar values of the carrier density with the nanostructure-free HH matrix. This strongly suggests that the embedded FH nanostructures also alter the effective mass (m*) of the existing carriers within the HH matrix. These fascinating electronic behavior within the p-type $Ti_{0.5}Hf_{0.5}Co_{1+x}Sb_{0.9}Sn_{0.1}$ HH/FH nanocomposites are rationalized by combining transmission electron microscopy (TEM) data with the concept of carriers culling by the valence bands maxima offset energy barrier, ΔE, at multiple HH/FH interfaces. This ability to drastically improve the PF of thermoelectric materials via nanostructuring strategy without increasing the thermal conductivity can open up new ways to further enhance the figure of merit of atomic-scale structurally engineered counterparts of existing n-type and p-type thermoelectric materials.

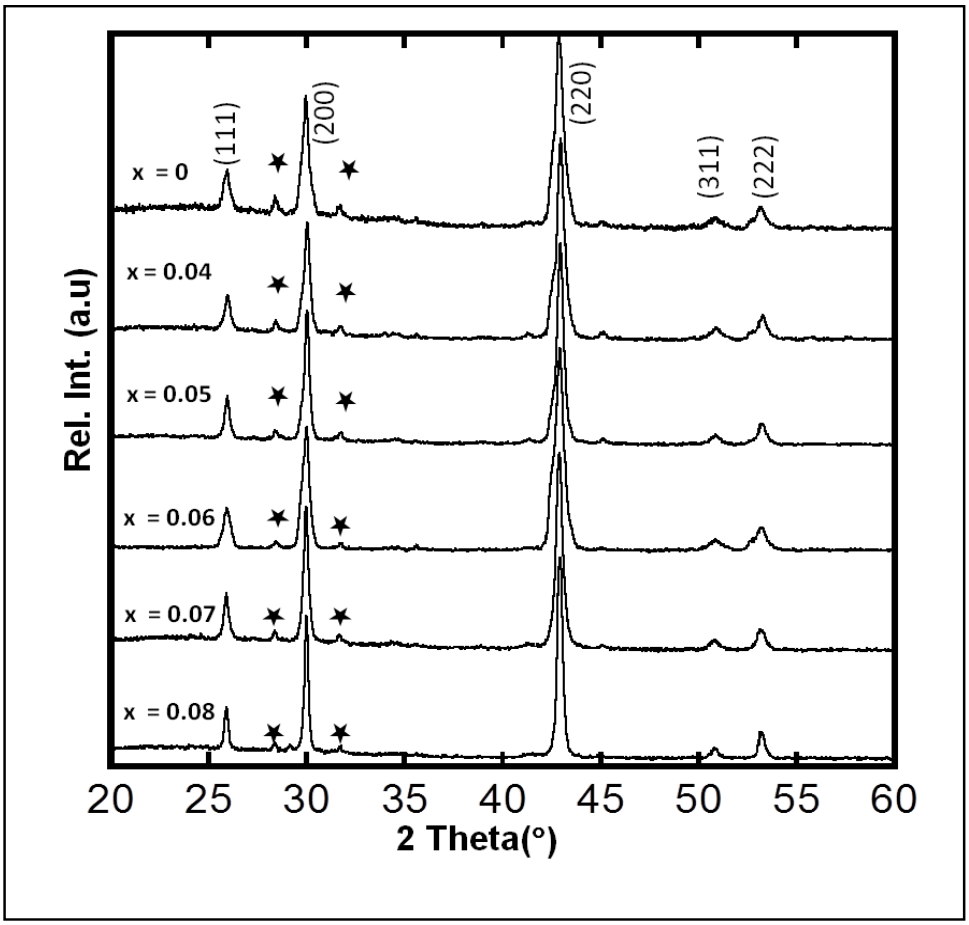

Figure 4.1 : X-ray powder diffraction patterns of the synthesized p-type $Ti_{0.5}Hf_{0.5}Co_{1+x}Sb_{0.9}Sn_{0.1}$ (HH(1-x)/(x)FH) nanocomposites. ★ corresponds to additional peaks of the HfO_2 main impurity phase.

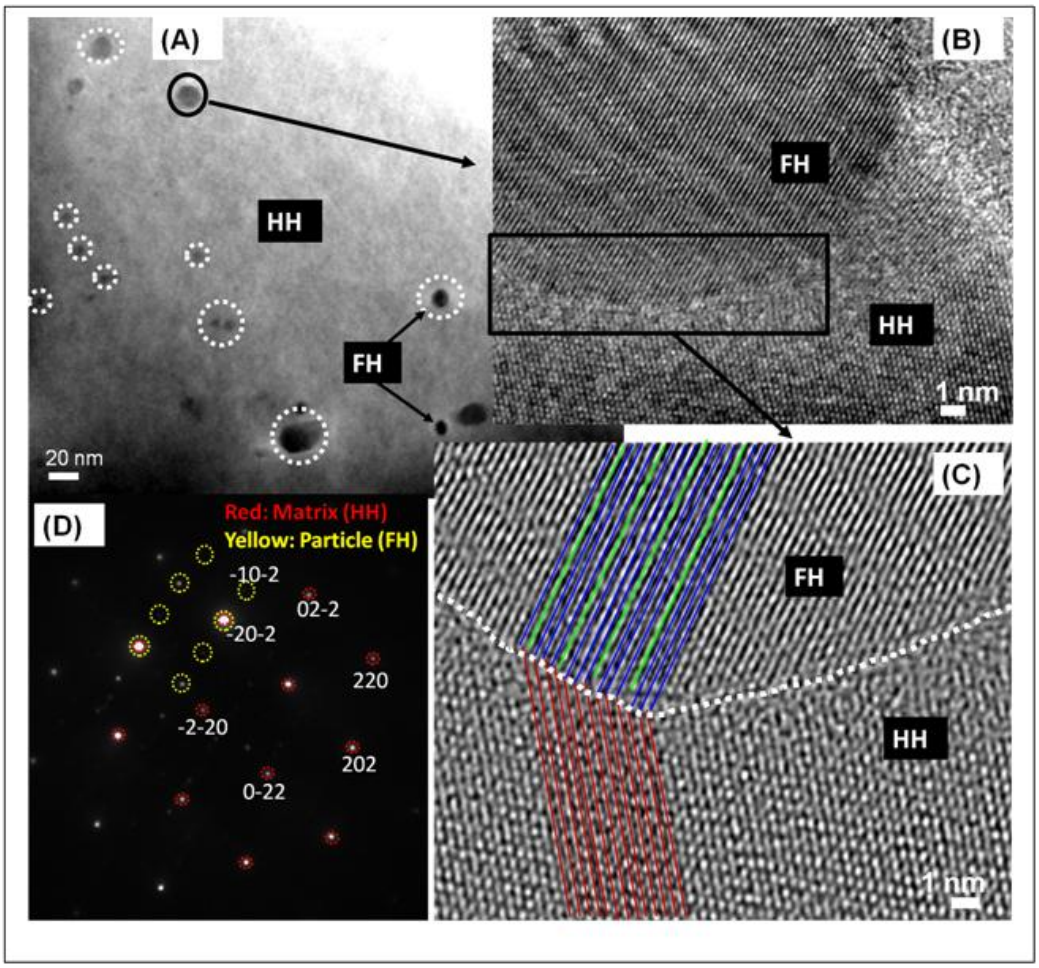

Figure 4.2 : (A) A low magnification TEM image of a hot pressed pellet of HH/FH(5%) bulk composite showing spherical nanometer scale (5nm to 60 nm) particles of FH well dispersed in a micrometer scale HH grain; **(B)** A HRTEM image of one of the precipitate showing excellent crystallinity and coherency with the matrix; **(C)** Enhanced HRTEM image revealing details of the HH/FH phase boundary structure; **(D)** SAED pattern of a portion of the HH/FH phase boundary indicating different crystallographic orientation for both HH and FH regions.

Bulk nanostructured alloys with nominal composition $Ti_{0.5}Hf_{0.5}Co_{1+x}Sb_{0.9}Sn_{0.1}$ (x = 0, 0.04, 0.05, 0.06, 0.07, 0.08) consisting of a matrix with half-Heusler (HH) crystal structure (MgAgAs structure type, space group: F-43m) containing coherently embedded nanoprecipitates with full-Heusler (FH) structure ($MnCu_2Al$ structure-type, SG: Fm-3m) were successfully prepared by

direct liquid state mediated solid-state combination of a mixture of high purity elemental powders of Hf, Ti, Sb, Sn and Co in the desired stoichiometry, at 1173K for 14 days. The mole fraction of FH nanoprecipitates within the composites is controlled by careful adjustment of the amount of excess elemental Co (relatively to the stoichiometry of a pure HH phase) in the starting composition. Such manipulation of the starting composition using excess Co is expected to trigger a simultaneous solid-state transformation of a given fraction of the HH phase into a Co-rich phase with FH structure according to reaction (1).

$$0.5Ti + 0.5Hf + (1+x)Co + 0.9Sb + 0.1Sn \rightarrow (1-x)Ti_{0.5}Hf_{0.5}CoSb_{0.9}Sn_{0.1}\ (HH) + x\ Ti_{0.5}Hf_{0.5}Co_2Sb_{0.9}Sn_{0.1}\ (FH) \quad (1)$$

X-ray powder diffraction (XRD) patterns of the resulting $Ti_{0.5}Hf_{0.5}Co_{1+x}Sb_{0.9}Sn_{0.1}$ ($0 < x < 0.8$) confirmed the formation of the HH phase along with minor HfO_2 impurity phase (Figure 4.1). However, no obvious peak that could indicate the presence of the anticipated FH phase was observed, even for the composition with excess Co ($x = 0.08$). The absence of the FH peaks in XRD patterns of the synthesized materials can be interpreted as the dissolution of the excess Co within the crystal structure of the HH matrix (formation of interstitial solid-solution). However,previous work with the n-type [178,179] systems showed that regardless of the amount of excess Ni (x value), the formation of the bi-phasic HH/FH system is favored over a simple dissolution of the excess element in interstitial positions within the structure of the majority phase. The spontaneous segregation between the HH and FH phases in the resulting product is driven by the difference in their structure type which precludes the formation of substitutional solid-solutions. In addition, the large fraction of vacancies within the structure of the HH matrix also favored the formation of the FH phase over the formation of an interstitial solid-solution between the HH matrix and the excess atoms (Ni or Co). This is due to the fact that the vacant

tetrahedral sites within the HH structure are relatively larger than interstitial sites and therefore can accommodate the excess atoms (Co, Ni, etc) with minimal distortion of the HH crystal lattice. To further investigate the presence of FH phases within the synthesized $Ti_{0.5}Hf_{0.5}Co_{1+x}Sb_{0.9}Sn_{0.1}$ materials, a high resolution (scanning) transmission electron microscopy (STEM) study was performed on several specimens of the sample with 5 at% excess Co. Careful examination of the low magnification (TEM) image revealed the presence of small spherical precipitates with size ranging from 5 to 60 nm randomly dispersed within the HH matrix (Figure 4.2A). High resolution image (Figure 4.2B) and selected area electron diffraction (SAED) pattern (Figure 4.2D) of a portion of the phase boundaries between the HH matrix and the precipitate revealed that both phases are highly crystalline with ordered crystal structures and are oriented along different crystallographic directions. Careful analysis of the SAED pattern suggested that the HH matrix with the unit cell parameter of 6.11Å is oriented along [-1 1 1] whilst the precipitate with the unit cell parameter of 6.78Å is oriented along zone axis [-1-1 0]. The cubic structure of the precipitates and the ~10% increase in their unit cell parameter with respect to the HH matrix suggest some structural similarities between the HH matrix and the precipitates. This result points to the formation of FH nanoprecipitates within the HH matrix as anticipated from reactions Eq. (1). An enhanced high-resolution TEM image of the HH-matrix/FH-inclusion phase boundary revealed coherent to semi-coherent relationships between lattice planes in both structures (Figure 4.2C). The small size and spherical shape of the FH inclusions along with the coherent nature of phase boundaries with the HH matrix strongly suggest either endotaxial nucleation of the FH seed crystals from a preformed HH crystal lattice followed by their isotropic growth through a solid-state Co diffusion type of mechanism, or a competing co-nucleation of both HH and FH seed crystals at various reaction fronts during the

solid-state synthesis from the mixture of elemental powders, followed by growth through an Ostwald ripening type mechanism. The final sizes of the FH inclusions within individual grains of the polycrystalline powder of HH/FH composite remain relatively small giving the dilute nature of the FH seed crystals within the reaction medium.

Study on Carrier Transports of the p-type nanocomposites The presence of coherently embedded nanometer scale FH inclusions within the crystal lattice of a p-type HH matrix with the nominal composition $Ti_{0.5}Hf_{0.5}CoSb_{0.9}Sn_{0.1}$ was found to alter drastically its electronic

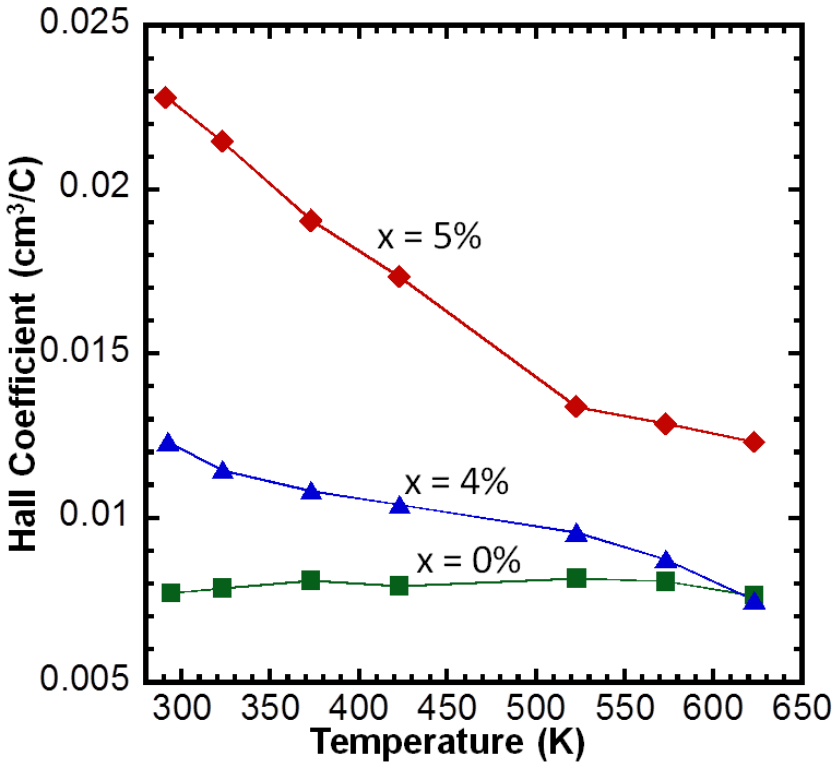

Figure 4.3 : Temperature dependence of the Hall coefficient of selected $Ti_{0.5}Hf_{0.5}Co_{1+x}Sb_{0.9}Sn_{0.1}$ (HH(1-x)/FH(x)) nanocomposites

transport properties. All $Ti_{0.5}Hf_{0.5}Co_{1+x}Sb_{0.9}Sn_{0.1}$ samples showed positive values of the Hall coefficient (Figure 4.3) and the thermopower (Figure 4.3B) indicating holes as the majority charge carriers. At 300K, the Hall coefficient (R_H) of the $Ti_{0.5}Hf_{0.5}Co_{1+x}Sb_{0.9}Sn_{0.1}$ samples increases from 0.008 cm^3/C for the HH matrix ($Ti_{0.5}Hf_{0.5}CoSb_{0.9}Sn_{0.1}$) to 0.012 cm^3/C for the sample with x = 0.04 and to 0.023 cm^3/C for the composition with x = 5% (Figure 4.3). The observed increase in R_H corresponds to a large drop in the hole density (Figure 4.4A) within the HH matrix upon increasing the mole fraction of the FH ($Ti_{0.5}Hf_{0.5}Co_2Sb_{0.9}Sn_{0.1}$) nanoinclusions, accordingly with the equation $p = +1/eR_H$ (e is the electron charge). At 300K, the density of holes in the $Ti_{0.5}Hf_{0.5}Co_{1+x}Sb_{0.9}Sn_{0.1}$ samples decreases from ~ 80 × $10^{19}/cm^3$ for the HH matrix (x = 0) to ~50× $10^{19}/cm^3$ upon addition of 4 at.% excess elemental Co in the starting mixture (which corresponds to the formation of $Ti_{0.5}Hf_{0.5}Co_{1.04}Sb_{0.9}Sn_{0.1}$ bulk nanocomposite containing 96 mole% HH and 4 mole% FH (96%HH/4%FH)). The hole density further decreases to ~28× $10^{19}/cm^3$ with the addition of 5 at.% excess elemental Co in the starting mixture ((95%HH/5%FH)). One possible straightforward interpretation of the observed drop in the hole density is obtained by assuming that the embedded FH nanoinclusions are metallic in nature and electronically dope the p-type HH matrix by dumping extra electrons which partially compensate the existing holes within the HH matrix. However, this interpretation does not account for the observed large change in the temperature dependence of the Hall coefficient (and therefore hole density) in the $Ti_{0.5}Hf_{0.5}Co_{1+x}Sb_{0.9}Sn_{0.1}$ samples that is clearly apparent already at room temperature where intrinsic carrier excitations do not take place. For instance, the Hall coefficient (R_H) is nearly temperature independent for the nanostructure free HH matrix (x = 0), whereas for $Ti_{0.5}Hf_{0.5}Co_{1+x}Sb_{0.9}Sn_{0.1}$ samples containing FH nanoinclusions, R_H decreases with increasing temperature (Figure 4.3) and progressively so with the increasing content of FH

nanoinclusions. Similar comparison can be made regarding temperature-dependent hole density curves for various $Ti_{0.5}Hf_{0.5}Co_{1+x}Sb_{0.9}Sn_{0.1}$ samples (Figure 4.4A). The hole density in the HH matrix (x = 0) remains nearly constant with increasing temperature, consistent with the behavior of a heavily doped semiconductor. However, the hole density in the sample containing 4 mole% FH inclusions gradually increases with temperature and tends asymptotically to the upper limit curve corresponding to the initial density of carriers within the HH matrix. For the sample with 5 mole% FH, a 62% drop in the carrier density is still observed at 625K when compared to the hole density within the HH matrix. This surprising increase in the hole density in the $Ti_{0.5}Hf_{0.5}Co_{1+x}Sb_{0.9}Sn_{0.1}$ nanocomposites with rising temperature is not consistent with the electron-hole compensation viewpoint used above to explain the drop in the hole density at 300K with increasing mole fraction of FH nanoinclusions. The primary reason is a strong temperature dependence of the Hall coefficient already at 300 K, well below the temperature where across-the-gap excitations can set in. The fact that the hole concentration within the nanocomposite is temperature dependent starting from 300K and asymptotically tends to the HH matrix carrier density at high temperatures suggests that this temperature dependent behavior is imposed by the embedded FH nanostructures rather than being a consequence of a simple doping process. To explain the decreasing carrier density and its progressively stronger temperature dependence with the increasing content of FH nanoinclusions in the HH matrix, we propose a new mechanism whereby the holes within the valence band (VB) of the HH matrix are discriminated with respect to their energy at the heterojunction between the HH matrix and the embedded FH nanostructures (Figure 4.5A). In this mechanism, we must consider that the embedded FH

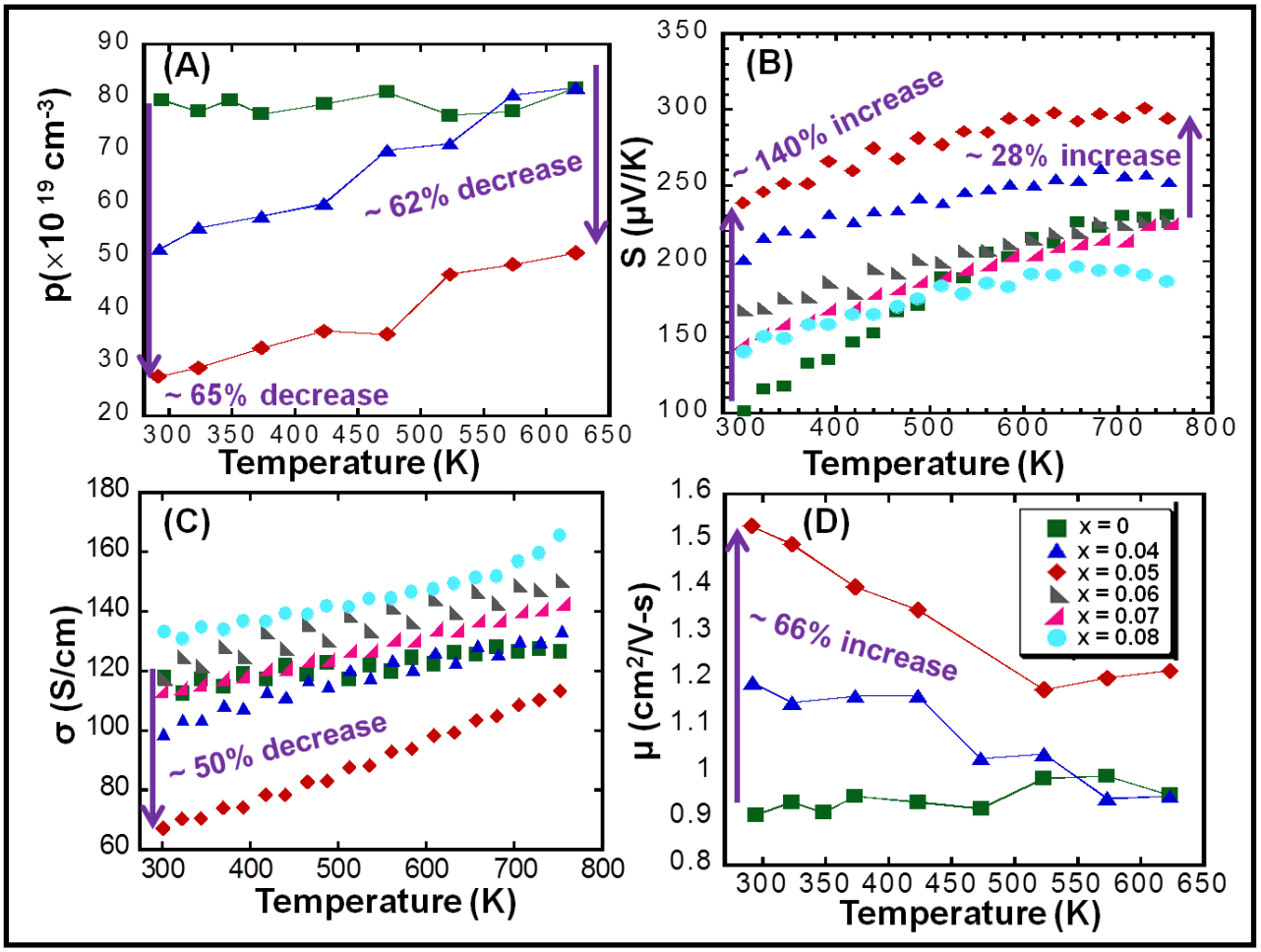

Figure 4.4 : Temperature dependence of the electronic transport properties of $Ti_{0.5}Hf_{0.5}Co_{1+z}Sb_{0.9}Sn_{0.1}$ (HH(1-x)/FH(x)) bulk nanocomposites: (A) Carrier concentration, (B) Seebeck coefficient; (C) Electrical conductivity and (D) Carrier mobility.

nanoinclusions because of their very small size behave like semiconductors with an energy gap E_g(FH) due to quantum confinement effects. Although a direct measurement of the semiconducting character of individual FH inclusions in the composites is not practical, our assumption is supported by the above discussion which clearly suggests that the observed hole density data is not consistent with a consideration that the embedded FH inclusions retain their bulk metallic nature. As the size of the FH inclusions decreases, the top of the valence band (VB) of the FH inclusions is gradually pushed below the valence band edge of HH. For a sufficiently small size of the FH nanoinclusions, the valence band maximum (VBM) of the FH inclusions will lie below the acceptor impurity band of the HH matrix. This results in the formation of an energy offset, ΔE, between the VBM of the FH inclusions and the highest energy level of the acceptor impurity band of the HH matrix. The potential barrier, ΔE, acts as an energy filter for conduction holes within the VB of the p-type HH matrix (Figure 4.5A). The magnitude of ΔE depends on the position of the VBM of FH inclusions which, in turn, under quantum confinement regime, depends on the size of the FH nanoinclusions. Within this band diagram picture, relative reductions in the carrier density measured at 300 K in the synthesized p-type HH (1-x)/ FH(x) nanocomposites correspond to the fraction of low energy conduction holes from the VB of the HH matrix trapped by the potential barrier, ΔE, at the HH/FH interfaces. The gradual increase in the carrier density with temperature observed in HH(1-x)/FH(x) nanocomposites can then be attributed to the promotion upon thermal excitation of "low energy"(LE) carriers trapped at the energy barrier around 300K, to energy levels higher than the magnitude of ΔE. One can anticipate a linear increase in the fraction of LE holes trapped by the potential barrier with the increasing population density of HH/FH interfaces within the HH(1-x)/FH(x) nanocomposites, provided FH nanoinclusions are of uniform size. An increase in the size of the FH

nanoinclusions would induce a reduction in the magnitude of ΔE leading to a smaller fraction of LE holes trapped at the HH/FH interfaces. Therefore, the departure from the linear relationship between the carrier density and the mole fraction of the FH phase (x values) observed for the HH(1-x)/FH(x) nanocomposites when going from the 4 at.% excess elemental Co to a composition with 5 at.% excess Co suggests alterations of both the population density of the HH/FH interfaces and the size of FH inclusions under our synthesis conditions.

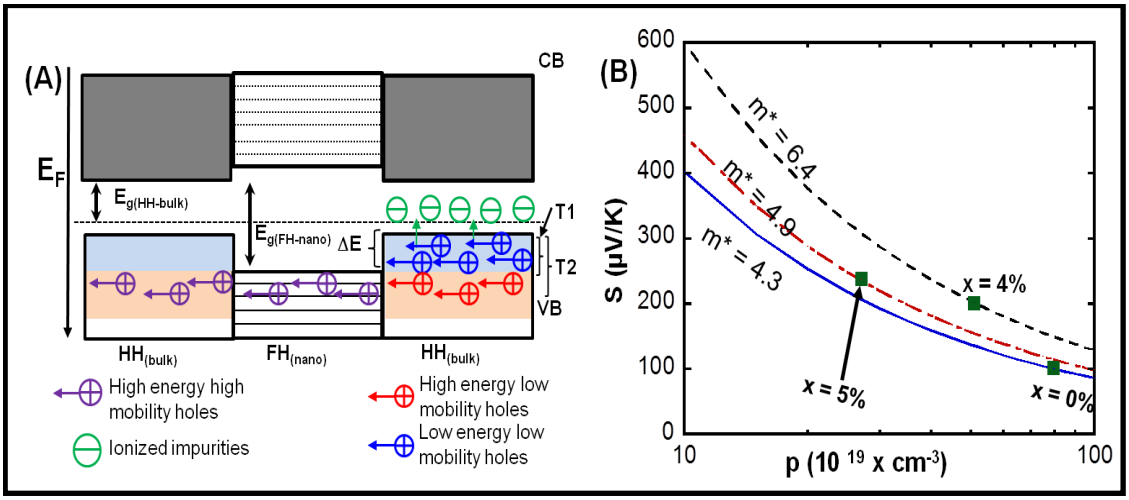

Figure 4.5 : (A) Schematic illustration of the atomic scale band structure engineering of a p-type HH matrix using a nanoinclusion with the FH composition. Selective trapping of low energy holes and transfer of high energy holes at the HH/FH heterojunction results in a decrease of the effective carrier density at 300 K simultaneously with an alteration of the carrier effective mass (m*) as revealed by the Pisarenko plots (B).

Figure 4.4B shows the temperature dependent thermopower (S) of HH(1-x)/FH(x) nanocomposites containing various mole fractions of FH nanoinclusions. All samples display positive thermopower values confirming p-type semiconducting behavior. At 300 K, the

thermopower rapidly increases with increasing mole fractions of FH inclusions ranging from 100 μV/K for the matrix (x = 0) to a maximum value of 240 μV/K for the nanocomposite with x = 0.05. This corresponds to a 140% increase in the thermopower, which is consistent with the observed large decrease in the carrier density with increasing x values. A further increase in the FH content above 5 mole% resulted in a gradual decrease of the thermopower value. However, a thermopower value of 140 μV/K (which corresponds to a 40% enhancement) was observed for the composition with 8 mole% FH inclusions. Regardless of the mole fraction of FH inclusions, the thermopower of the HH(1-x)/FH(x) nanocomposites slowly increases with rising temperature, whereas the thermopower of the matrix increases considerably more rapidly. However, a 28% enhancement in the thermopower (~300 μV/K) is still maintained at 775K for a composite with 5mole% FH inclusions. To further understand the nature of the observed large enhancement in the thermopower of the synthesized HH(1-x)/FH(x) nanocomposites, a Pisarenko plot giving a relationship between the thermopower and the carrier density (p), $S = [(8\pi^2(k_B)^2)/3eh^2]m^*T(\pi/3p)^{2/3}$ for compositions with x = 0, 0.04, and 0.05 was constructed (Figure 4.5B). Assuming parabolic bands and an energy independent relaxation time assumptions, the thermopower at a given temperature can be described by a unique value of the effective mass (m*) [177]. However, no single value of the effective mass that allows fitting of all the data could be obtained, suggesting that the embedded FH nanoinclusions, in addition to reducing the effective carrier density within the $Ti_{0.5}Hf_{0.5}CoSb_{0.9}Sn_{0.1}$ (HH) matrix, also significantly alter the electronic band structure close to the Fermi level. This is confirmed by an increase in the carrier effective mass (m*) values extracted from the fits of S versus p curves for HH(1-x)/FH(x) nanocomposites. At 300K, the values of the effective mass (m*) are 4.3 m_e (x = 0), 6.4 m_e (x = 0.04), and 4.9 m_e (x = 0.05), respectively.

The temperature dependent electrical conductivity of the synthesized HH(1-x)/FH(x) nanocomposites is shown in Figure 4.4C. The electrical conductivity at 300K initially decreases with the increasing FH content, reaches the minimum value of 62 S/cm for the composition with 5 mole% FH inclusions and thereafter increases with further increasing FH content (increasing x values). The minimum room temperature value of the electrical conductivity observed for the nanocomposite containing 5 mole % FH inclusions corresponds to a ~ 50% reduction in the electrical conductivity when compared to that of the HH matrix (120 S/cm). The observed reduction in the electrical conductivity with the increasing FH content up to 5mole% is consistent with the reduction in the carrier density (Figure 4.4A). However, the magnitude of the drop in the electrical conductivity is smaller than the anticipated 65% decrease (accordingly to the equation $\sigma = p\mu e$) if the hole mobility remained constant. This strongly suggests that the reduction in the carrier concentration observed in several HH(1-x)/FH(x) compositions is accompanied by a large increase in the hole mobility at 300K (Figure 4.4D). Interestingly, room temperature values of the electrical conductivity higher than that of the HH matrix were observed for HH(1-x)/FH(x) nanocomposites with $x > 0.05$, simultaneously with the observed enhancements in the thermopower (Figure 4.4B). For instance, the electrical conductivity of the HH(0.92)/FH(0.08) nanocomposite is ~ 135 S/cm at 300K. This corresponds to ~13% enhancement in the electrical conductivity when compared to the HH matrix, while a 40% enhancement in the thermopower was also observed for the same sample at 300 K. This simultaneous increase in the thermopower and the electrical conductivity of the HH(0.92)/FH(0.08) nanocomposite clearly indicates that the reduction in the carrier concentration of HH(1-x)/FH(x) nanocomposites is overcompensated by a large enhancement in the carrier mobility. Astonishingly, the electrical conductivity of the synthesized nanocomposites

increases with rising temperature, whereas a nearly temperature independent conductivity is observed for the HH matrix. This change in the temperature dependence of the electrical conductivity is consistent with the observed rapid increase in the carrier density in HH(1-x)/FH(x) nanocomposites with rising temperature and suggests that the embedded FH nanoinclusions modify the electrical conduction within the HH matrix.

Figure 4.4D shows the temperature dependent carrier mobility of selected $Ti_{0.5}Hf_{0.5}Co_{1+x}Sb_{0.9}Sn_{0.1}$ (HH(1-x)/FH(x)) nanocomposites. While the carrier mobility decreases with increasing temperature regardless of the composition, it increases markedly with the increasing content of FH nanoinclusions at a given temperature. For instance, at 300 K, the mobility increases 0.9 $cm^2/V{\cdot}s$ for the HH matrix to 1.5 $cm^2/V{\cdot}s$ for the composite with x = 0.05. This corresponds to ~ 66% increase in the hole mobility. The observed enhancement in the hole mobility with the increasing content of FH inclusions (regardless of the temperature) is quite surprising. In a conventional semiconductor, the overall mobility of charge carriers as defined by the expression $\mu = e(\tau/m^*)$ is influenced by the carrier effective mass (m*) and by the average relaxation time (τ) between various scattering events including phonon-electron scattering, ionized-impurity scattering and electron-electron scattering. Upon embedding FH inclusions within the HH matrix, one would normally expect a decrease in τ due to increased frequency of carrier scattering events. This should lead to a significantly lower carrier mobility provided the carrier effective mass remains constant. However, from the Pisarenko plot giving the relationship between the thermopower and the carrier density (Figure 4.4B), we observe an increase in the carrier effective mass in the HH(1-x)/FH(x) nanocomposites. This result again suggests that one should observe lower carrier mobilities in the synthesized nanocomposites. The highly surprising large increase in the carrier mobility observed in the HH(1-x)/FH(x) nanocomposites, despite the

simultaneously enhanced effective masses of charge carriers, indicates that the embedded FH nanostructures promote charge carrier transport within the semiconducting HH matrix instead of hindering it as one would normally expect for a conventional semiconducting composite system.

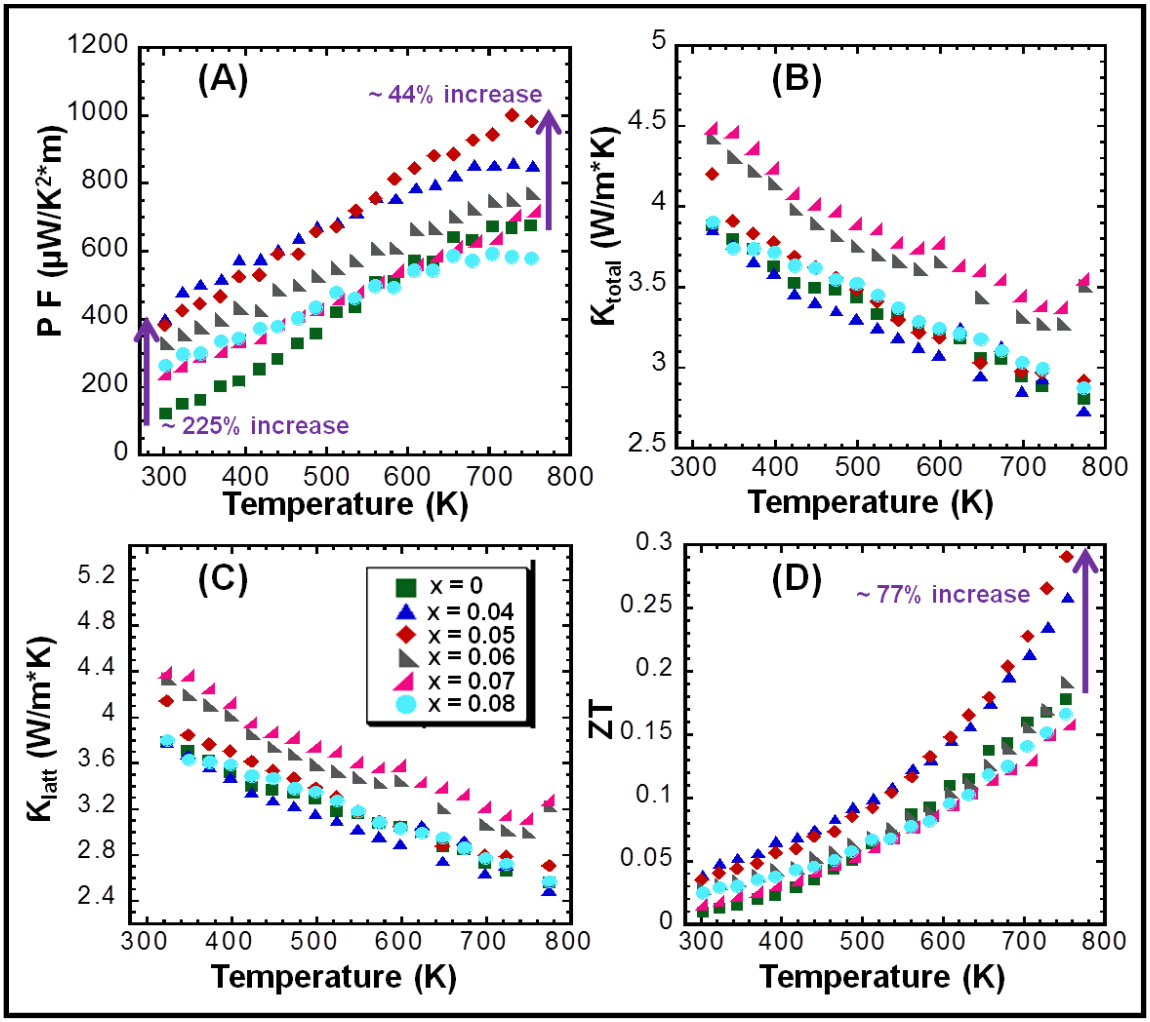

Figure 4.6 : Temperature dependence of the thermoelectric properties of $Ti_{0.5}Hf_{0.5}Co_{1+z}Sb_{0.9}Sn_{0.1}$ (HH(1-x)/FH(x)) bulk nanocomposites: (A) Power factor, (B) Total thermal conductivity; (C) Lattice thermal conductivity and (D) Figure of Merit (ZT).

The observed large increase in the mobility is therefore ascribed to a surprisingly large increase in the relaxation time (τ). Several factors can contribute to an increase in the relaxation time of HH(1-x)/FH(x) nanocomposites. For example, a drop in the effective carrier density arising from the trapping at 300K, of low energy carriers by the potential barrier, $\triangle E$ at the HH/FH interfaces (Figure 4.5A) results in a reduction in the frequency of electron-electron collisions leading to a longer relaxation time between scattering events. Another important contributing factor may be a spatial separation at the HH/FH interfaces, where holes located within the valence band (VB) of the FH inclusions are separated from ionized-impurities located within the acceptor sub-band in the HH matrix (Figure 4.5A). This spatial separation breaks weak electrostatic interactions between ionized-impurities and holes leading to a lower frequency of carrier scattering by ionized-impurities. Finally, it is highly likely that the high energy carriers (those able to get across the barrier at the HH/FH interface) are more mobile than the average carrier.

The observed large enhancement in the thermopower and only a modest decrease in the electrical conductivity result in large improvements in the power factor ($PF = \sigma \cdot S^2$) of $Ti_{0.5}Hf_{0.5}Co_{1+x}Sb_{0.9}Sn_{0.1}$ (HH(1-x)/FH(x)) nanocomposites (Figure 4.6A). At 300K, the power factor of the p-type $Ti_{0.5}Hf_{0.5}CoSb_{0.9}Sn_{0.1}$ (HH) matrix is 100 $\mu W/K^2m$ and slowly increases with temperature to 650$\mu W/K^2m$ at 775K. Upon embedding 4 mole% and 5 mole% of FH nanoinclusions into the HH matrix, the room temperature value of the PF of the resulting nanocomposites increases to 400$\mu W/K^2m$. A further increase in the FH content however results in a gradual decrease of the PF due to a drop in the thermopower values. The PF of the HH(1-x)/FH(x) nanocomposites monotonically increases with rising temperature, reaching a value of 1000 $\mu W/K^2m$ at 775K for the composition with 5 mole% of FH inclusions.

Figures 4.6B and 4.6C show the temperature dependence of the total and lattice thermal conductivity of HH(1-x)/FH(x) nanocomposites. The lattice thermal conductivity (κ_L) was obtained by subtracting the electronic component κ_e from the total thermal conductivity, κ. $\kappa_e = L_o\sigma T$ was estimated using the Wiedemann-Franz law where $L_o = 2.45 \times 10^{-8}$ $W\Omega K^{-2}$ is the Lorenz number. The thermal conductivity of HH(1-x)/FH(x) nanocomposites is comparable to that of the HH matrix except for compositions with x = 0.06 and 0.07 which showed higher total as well as lattice thermal conductivities. At 300K, the thermal conductivity is ~ 3.9 W/m·K and decreases almost linearly with rising temperature, reaching a value as low as 2.7 W/m·K at 775K for the composition with x = 0.04. It is somewhat surprising that the effect of FH nanoinclusions is not more apparent in the behavior of the lattice thermal conductivity. Perhaps the mass and strain contrast between FH nanoinclusions and the HH matrix is not large enough to affect phonon scattering.

Large enhancements in the power factor of HH(1-x)/FH(x) nanocomposites with x = 0.04 and 0.05 over the value of the power factor of the HH matrix coupled with comparable values of their total thermal conductivities result in a large improvement in the thermoelectric figure of merit (ZT) of these nanocomposites at high temperatures (Figure 4.6D). At 775K, the ZT values of HH(1-x)/FH(x) nanocomposites increase from ZT ~ 0.15 for the composition with x = 0 to approximately ZT ~ 0.3 upon coherently embedding 5 mole% FH nanoinclusions within the HH matrix. This corresponds to a nearly 80% improvement when compared to the $Ti_{0.5}Hf_{0.5}CoSb_{0.9}Sn_{0.1}$ (HH) matrix (Figure 4.6D). Although, the observed highest ZT value for the p-type $Ti_{0.5}Hf_{0.5}Co_{1.05}Sb_{0.9}Sn_{0.1}$ (HH(95%)/FH(5%)) nanocomposite remains relatively low when compared to fully optimized state-of-the-art HH materials [189], we anticipate that the

application of the FH nanostructuring concept reported in this work will lead to higher figures of merit when working with HH matrices having optimized carrier densities.

Thermoelectric performance of n-type $Ti_{0.15}Hf_{0.85}Ni_{1+x}Sn_{0.975}Sb_{0.025}$ (HH(1-x)/FH(x)) nanocomposites

This study mostly showcases the effect of nanostructuring on the n-type composition as it showed in the p-type composition, explained earlier. It demonstrated that the thermopower (S) and carrier mobility (μ) within a bulk semiconducting half-Heusler (HH) matrix with composition $Ti_{0.15}Hf_{0.85}NiSn_{0.975}Sb_{0.025}$ are gradually enhanced by embedding in a coherent fashion, various fractions of full-Heusler (FH) quantum dots (QDs) within the crystal lattice of the HH matrix. Quantum dots (QD) engineered half-Heusler (HH) semiconducting composite materials consisting of $Ti_{0.15}Hf_{0.85}NiSn_{0.975}Sb_{0.025}$ (HH) matrix with various mole fractions of quantum dots (QDs) with full-Heusler (FH) structure (nominal composition $Ti_{0.15}Zr_{0.85}Ni_2Sn_{0.975}Sb_{0.025}$) coherently embedded within the crystal lattice of the HH matrix was achieved by direct solid-state reaction of a mixture of high purity elemental powders of Ti,Hf, Ni and Sn in the desired stoichiometry, at 900 °C for seven days. The mole ratio of Ti,Hf, Ni and Sn is calculated to form a pure HH phase, and various amount of excess elemental Ni (0 at.%,0.5 at.%, 1 at.%,2 at.%, 4 at.%, 5 at.%, 7 at.%,8 at.%,9 at.% and 10 at.%) is added to the initial mixture to program a simultaneous partial solid state transformation of the resulting HH phase into a FH structure according to reaction (2).

$$0.15Ti + 0.85Hf + (1+x)\,Ni + 0.975\,Sn + 0.025\,Sb \rightarrow (1-x)\,Ti_{0.15}Hf_{0.85}NiSn_{0.975}Sb_{0.025}\ (HH) + xTi_{0.15}Hf_{0.85}Ni_2Sn_{0.975}Sb_{0.025}\ (FH) \quad (2)$$

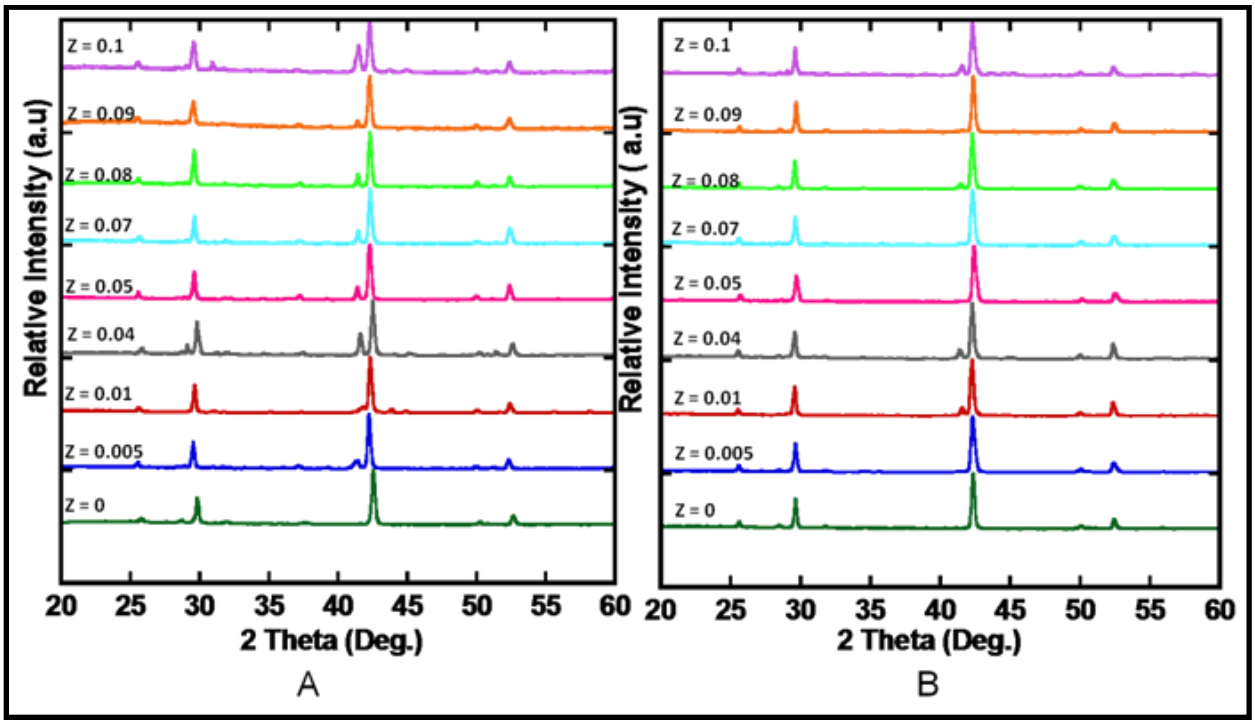

Figure 4.7 : X-ray diffractions patterns of $Ti_{0.15}Hf_{0.85}Ni_{1+z}Sn_{0.975}Sb_{0.025}(0\leq z\leq 0.1)$ half-Heusler alloys after first heating (A) and after second heating (B).

All the sample fabrication were done by employing the procedure as mentioned in earlier section . Structural characteristics of the resulting Ti0.15Hf0.85Ni1+xSn0.975Sb0.025 nanocomposites were investigated using X-ray powder diffraction (XRD) and transmission electron microscopy (TEM). XRD data (Fig. 4.7A) of the as-synthesized $Ti_{0.15}Hf_{0.85}Ni_{1+x}Sn_{0.975}Sb_{0.025}$ (x = 0, 0.005, 0.01, 0.02, 0.04, 0.05 ,0.07, 0.08, 0.09 and 0.1) materials suggested that the samples faced insolubility issue. It was speculated that may be the annealing temperature or the annealing time was not adequate for the completion of the reaction. So the samples were reannealed for 200 hours at 900^{o}C to drive the reactions towards completion (Figure 4.7B). The samples obtained from second heating showed X-ray diffraction patterns closer to the single phase half-Heusler alloy.

To probe the presence of the FH secondary phase within the synthesized nanocomposites and also to determine their characteristics high resolution transmission electron microscopy (HRTEM) study was performed on selected specimens. TEM images from the sample containing 8 at.% excess Ni ($Ti_{0.15}Hf_{0.85}Ni_{1.08}Sn_{0.975}Sb_{0.025}$), which corresponds to a nanocomposite system consisting of 92 mole% HH and 8 mole % FH ,reveal that the FH precipitates have nearly spherical morphology with size ranging from 20 nm (Fig. 4.8). The spherical shape of the nanodots suggests endotaxial nucleation of the precipitate seed crystals within the HH crystal lattice followed by their isotropic growth. The selected-area electron diffraction pattern (Fig. 4.8, inset) confirmed that it is fcc structure. Therefore, we predict based on the above structural details as well as on the chemical equation (2) that the observed precipitates are full-Heusler nanodots (quantum dots). Observation of spherical shaped FH nanodots and their high lattice coherency with the HH matrix suggests a co-nucleation and growth of both HH and FH seed crystals during the solid-state reaction from the mixture of elemental powers.

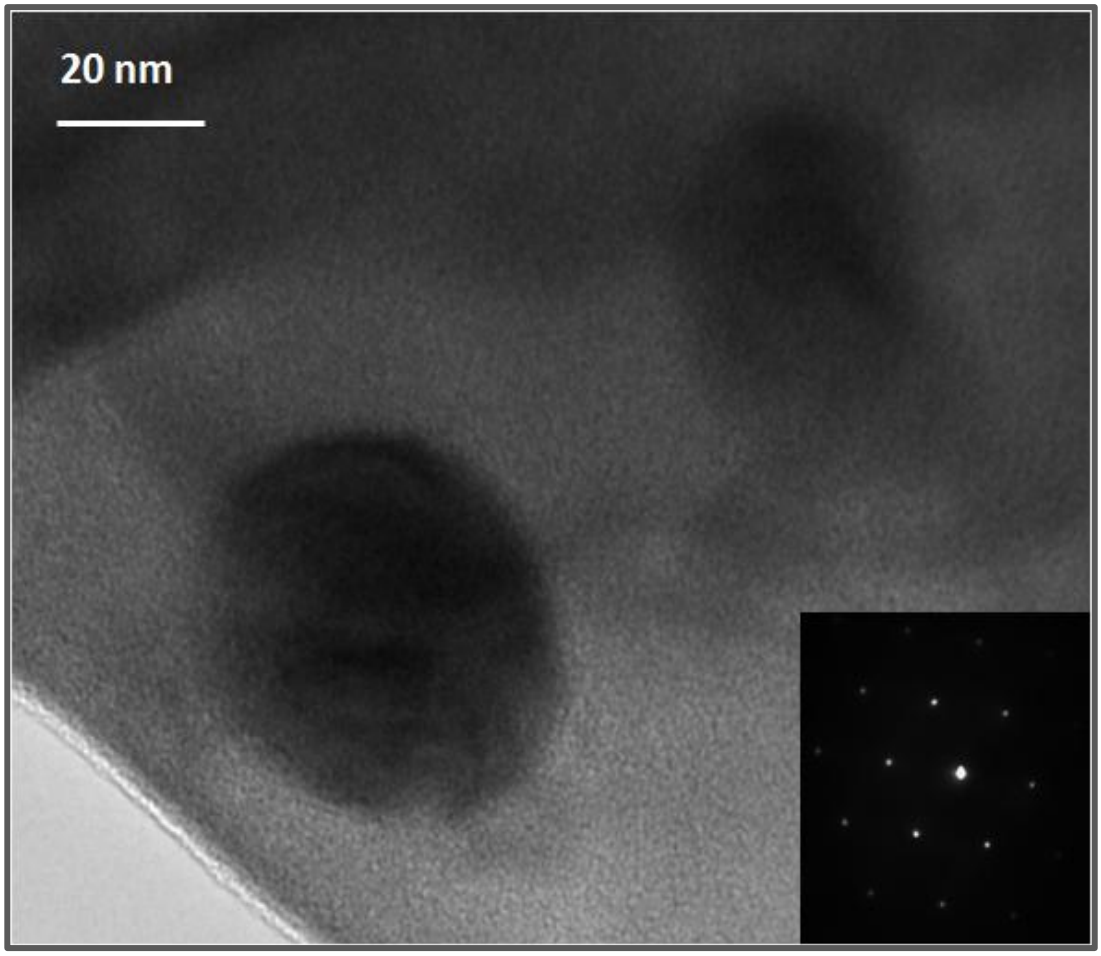

Figure 4.8 : TEM images of a hot pressed pellet of HH/FH(8%) bulk composite showing nanometer scale particles of FH micrometer scale grains . The spherical FH precipitates with particles size around 30 nm. Electron diffraction pattern FH regions showed it to be fcc(inset).

Studies on Carrier Transports of the p-type nanocomposites

Figs. 4.9A to 4.9D reflect the high temperature electronic transport properties of $Ti_{0.15}Hf_{0.85}Ni_{1+x}Sn_{0.975}Sb_{0.025}$ (HH) materials containing various mole fractions of the FH nanostructures embedded within the HH matrix. At 300K, the density of charge carriers in the $Ti_{0.15}Hf_{0.85}NiSn_{0.975}Sb_{0.025}$ (HH) matrix is ~ 40 × 10^{19}/cm^3 (Fig. 4.9A). Being an n-type nanocomposite, electrons act as the charge carriers for these materials. This value of the carrier density starts to increase and attains the maximum value of ~115 × 10^{19}/cm^3 at 300K, upon addition of 4 at.% excess elemental Ni in the starting mixture, which corresponds to the formation of $Ti_{0.15}Hf_{0.85}Ni_{1.04}Sn_{0.975}Sb_{0.025}$ bulk nanocomposite containing 96 mole% HH and 4 mole% FH (96%HH/4%FH) according to equation (2). Increasing the excess of elemental Ni to 8 at.% results in a larger decrease of the carrier density (49%) at 300K within the corresponding 92%HH/8%FH nanocomposites with respect to the 4 at% FH composition.

Careful analysis of temperature dependent carrier density curves for various $Ti_{0.15}Hf_{0.85}Ni_{1+x}Sn_{0.975}Sb_{0.025}$ (HH(1-x)/FH(x)) nanocomposites revealed different trends in their shape with respect to temperature. For the nanostructure-free composition (x = 0), the carrier density remains almost constant up to 550 K which is the behavior of a typical intrinsic semiconductor. For $Ti_{0.15}Hf_{0.85}Ni_{1+x}Sn_{0.975}Sb_{0.025}$ (HH(1-x)/FH(x)) the carrier density gradually increases with temperature. For the composition with 0.5 mole% FH, the carrier density behaves almost same as the matrix (x = 0). As the Ni added in excess of 1increases slowly with rising temperature from 300K up to 550K. In (HH(1-x)/FH(x)) nanocomposites with 4 mole% and 10 mole% FH, the carrier density increases at a faster rate between 300 and 775K. It is noteworthy,

that the carrier density within the (HH(1-x)/FH(x)) nanocomposites remains higher or equal to the HH matrix carrier density irrespective the temperature. This gradual increase in the carrier density with temperature observed for the (HH(1-x)/FH(x)) nanocomposites is similar to the behavior typically expected for doped semiconductors. The overall carrier density within the HH(1-x)/FH(x)) nanocomposites at a given temperature is higher for all the samples than that of the $Ti_{0.15}Hf_{0.85}NiSn_{0.975}Sb_{0.025}$ matrix indicates that some additional carriers were added to the existing ensemble of carriers within the matrix upon embedding the FH nanostructures. Such enhancement in the carrier concentration of the HH/FH composite could be associated with a gradual reduction in the band gap of the HH matrix with increasing FH content. This simple explanation is also consistent with the thermo power data in which the gradual decrease with the temperature of maximum thermo power with increasing FH content suggests a reduction in the band gap of the HH matrix (Fig. 4.9B). Therefore, the traditional doping concept is well applicable in this system. But the sample with maximum doping (x = 0.08) shows almost similar values of Seebeck with that of HH matrix values which is attributed to the comparable carrier density. Fig. 4.9B shows the temperature dependence of the thermopower of HH(1–x)/FH(x) composites. All samples showed negative values of the thermopower indicating n-type conducting behavior in the measured temperature range. The thermopowers of the composites increase with temperature regardless of the mole fraction of the FH inclusions.

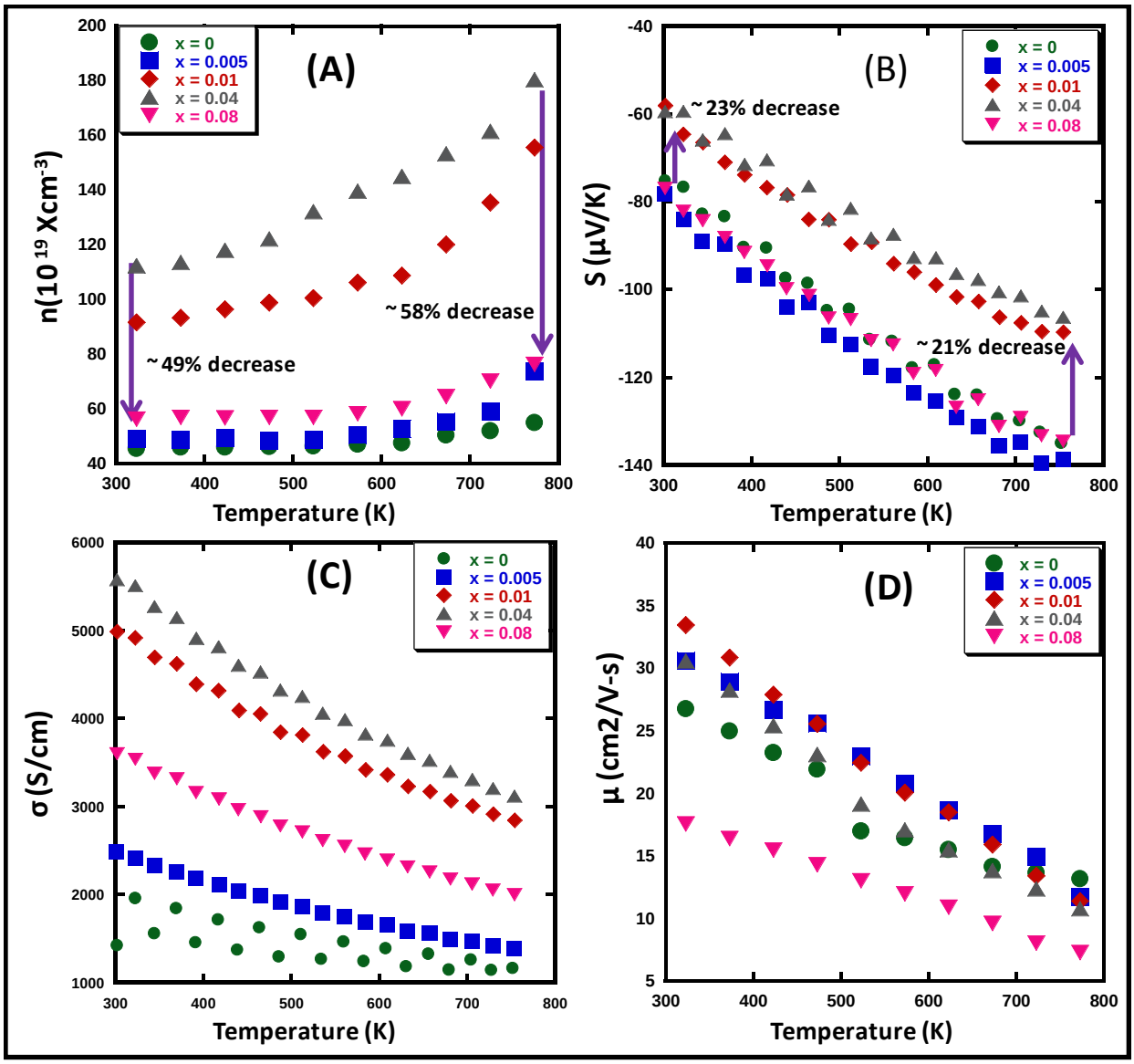

Figure 4.9 : Temperature dependent electronic transports in quantum dots engineered $Ti_{0.1}Zr_{0.9}Ni_{1+x}Sn$ nanocomposites. (A) carrier density; (B) thermopower; (C) electrical conductivity; (D) carrier mobility.

The introduction of large metallic inhomogeneities in the form of full-Heusler (FH) phases into a semiconductor such as the half-Heusler (HH) alloys mostly lead to electronic doping of the semiconducting HH matrix by the FH inclusion phase. As a result of which a drastic increase in the carrier density can be observed with increasing mole fraction of FH inclusions [41]. However, the observed decrease in the carrier density in the sample with 8% mole fraction of FH inclusions is ascribed to the formation of energy barriers, ΔE, at the HH-matrix/FH-inclusion interfaces, which act as an energy filter for conduction electrons within the HH matrix [42]. The gradual increase in the carrier density with temperature observed in the HH(1-x)/FH(x)) nanocomposites can be associated with some forms of charge carriers "culling" within the conduction band (CB) of the (HH) matrix, based on their relative energy distribution (e.g. low energy carrier versus high energy carrier), using the embedded FH nanostructures.

Fig. 4.10A shows the band structure of HH-FH phase. Both the phases are similar with respect to their chemical composition but differs by the presence of a partially filled band with Ni character on top of the FH valence band (VB). Presence of this additional band tends to push the valence band maxima (VBM) and the conduction band minima (CBM) of the FH inclusion to higher energy compared to that of the corresponding HH phase which might steer the formation of type –II (staggered gap) heterojunctions at the nanometer scale HH/FH interfaces within the $Ti_{0.15}Hf_{0.85}Ni_{1+x}Sn_{0.975}Sb_{0.025}$ (HH(1-x)/FH(x)) nanocomposites (Fig. 4.10B). This energy difference (ΔE) between the band maxima of both the phases act like a "filter "for conduction electrons within the conduction band of the HH matrix, filtering these charge carriers according to their energy values. This energy difference mostly depends on the position of CBM of the FH inclusion. Under quantum confinement regime, this phenomenon can be explained as the contribution of size of the FH nanoinclusions.

Therefore, the relative reductions in carrier density measured in various $Ti_{0.15}Hf_{0.85}Ni_{1+x}Sn_{0.975}Sb_{0.025}$ (HH(1-x)/FH(x)) nanocomposites at 300 K reflects the fraction of low energy conduction electrons from the CB of the HH matrix trapped by the potential barrier, ΔE, at the HH/FH interfaces. The gradual increase in the carrier density with temperature observed in $Ti_{0.15}Hf_{0.85}Ni_{1+x}Sn_{0.975}Sb_{0.025}$ (HH(1-x)/FH(x)) nanocomposites can thus be attributed to "low energy"(LE) carriers, which are trapped at the energy barrier around 300K, gradually overcoming the ΔE potential barrier due to thermal excitation. The fraction of LE electrons trapped by the potential barrier increases with the population density of HH/FH interfaces within the $Ti_{0.15}Hf_{0.85}Ni_{1+x}Sn_{0.975}Sb_{0.025}$ (HH(1-x)/FH(x)) nanocomposites, but also decreases with increasing size of FH nanostructures (decreasing ΔE). Under our synthesis conditions, increasing the percentage of excess elemental Ni atoms in the starting compositions can lead to the formation of: (1) a large number of small FH quantum dots with narrow size distribution or (2) a mixture of small and large FH quantum dots. This explains the observed irregularities in the drops of carrier density within the $Ti_{0.1}Zr_{0.9}Ni_{1+x}Sn$ (HH(1-x)/FH(x)) nanocomposites when going from the 4 at.% excess elemental Ni to the compositions with 8 at.% excess Ni (Fig. 4.9A).

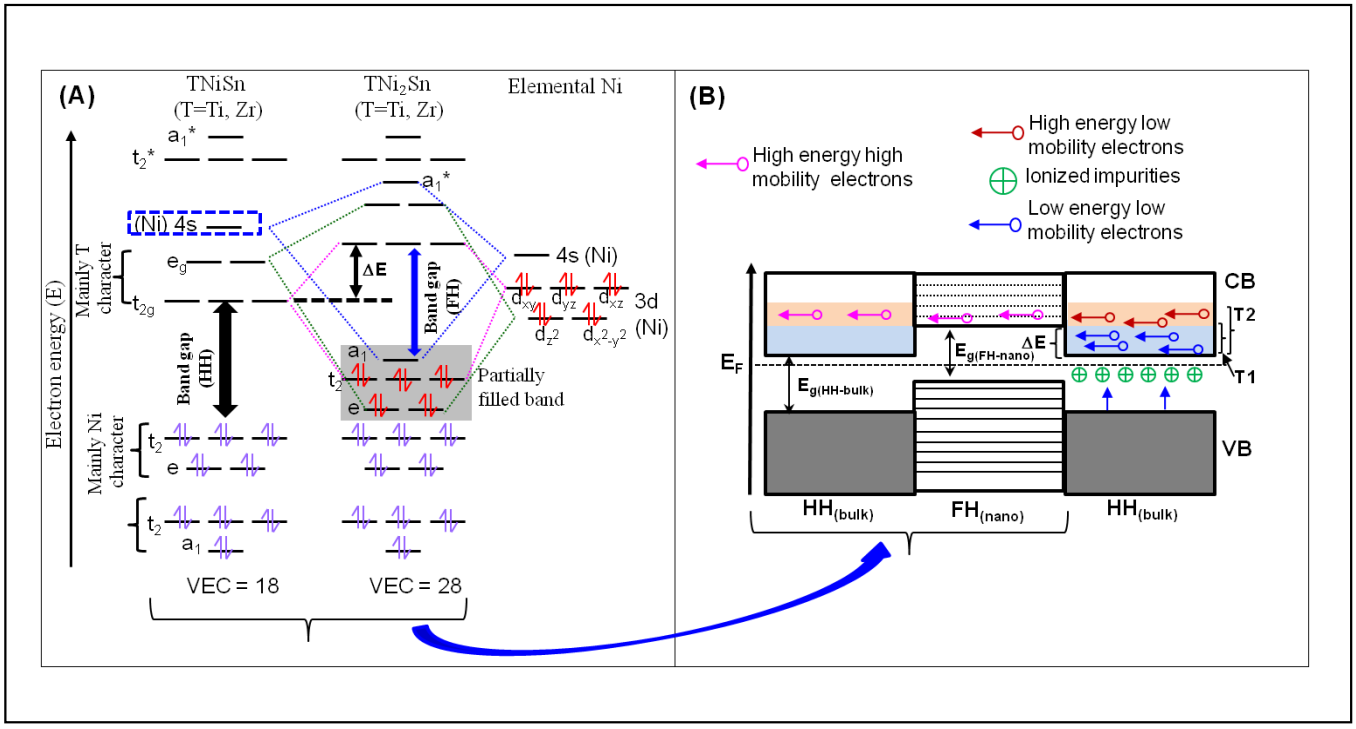

Figure 4.5 : Illustrations of the HH and FH band structures alignment at the HH/FH interfaces. (A) Molecular orbital diagram of full-Heusler (TNi_2Sn) generated from that of half-Heusler phase (TNiSn) upon insertion of elemental Ni into vacant tetrahedral site. Comparison of the HH and FH molecular orbital diagrams reveals energy offset of both the valence band maxima (VBM) and the conduction band minima (CBM) leading to nanometer scale type-II (staggered gap) heterojunctions at the HH/FH interface. The conduction band energy offset, ΔE, acts as an energy filter for conduction electrons within the HH matrix. (B) Proposed mechanism of the filtering of low energy electrons (from CB of HH) at the potential barrier, ΔE, (reducing effective carrier density) and spatial separation of high energy electrons (within CB of FH) from ionized-impurities at nanometer scale HH/FH heterojunctions. Cyan and orange colors represent distributions of low and high energy electrons at temperatures T1 and T2 (T2 > T1) within the CB of the HH matrix.

Figure 4.9 B explains the Seebeck or the thermopower of the nanocomposite. The FH quantum dots induce changes in the effective carrier density within the $Ti_{0.15}Hf_{0.85}NiSn_{0.975}Sb_{0.025}$ (HH) matrix as well as their temperature dependence, are also expected to result in large alterations of the thermopower of $Ti_{0.15}Hf_{0.85}Ni_{1+x}Sn_{0.975}Sb_{0.025}$ (HH(1-x)/FH(x)) nanocomposites (Fig. 4.9B). All nanocomposites showed negative values of the thermopower in the measured temperature range, suggesting electrons as the majority charge carriers. At room temperature (300 K), the thermopower value of $Ti_{0.15}Hf_{0.85}Ni_{1+x}Sn_{0.975}Sb_{0.025}$ nanocomposites increase from -75 μV/K (for x = 0) to -59 μV/K (for x = 0.04). This corresponds to about 23% decrease in the thermopower of HH(96%)/FH(4%) nanocomposite compared to the $Ti_{0.15}Hf_{0.85}NiSn_{0.975}Sb_{0.025}$ (HH) matrix. The room temperature values of the thermopower further increase to -77 μV/K (for x = 0.08) which is comparable to the HH matrix. Irrespective of the composition, the absolute values of the thermopower of $Ti_{0.15}Hf_{0.85}Ni_{1+x}Sn_{0.975}Sb_{0.025}$ nanocomposites increase with rising temperature, reaching maximum values at 775K. The thermopower of the HH matrix and the HH-FH composite (x=0.005) are almost comparable. Furthermore, the composite with FH content (x= 0.01,0.04) shows an decrease in the thermopower which can be explained due to increase in the mole fraction of FH content which is a result of increased carrier density observed in Fig 4.9 A. contrary to this common trend, composite with x= 0.08 shows an increased thermopower comparable to matrix. To justify this observed anomalous behavior , careful examination has been done on the carrier mobility with respect to the percentage of FH inclusion(Fig. 4.9D). The plot revealed anomalous changes in the magnitude of carrier mobility upon altering the FH content in $Ti_{0.15}Hf_{0.85}Ni_{1+x}Sn_{0.975}Sb_{0.025}$ (HH(1-x)/FH(x)) nanocomposites. It is observed that the thermo power value of the HH(92%)/FH(8%) nanocomposite at 775K is almost equal to that of

the $Ti_{0.15}Hf_{0.85}NiSn_{0.975}Sb_{0.025}$ (HH) matrix despite the noticeable difference in their carrier mobility at the same temperature.

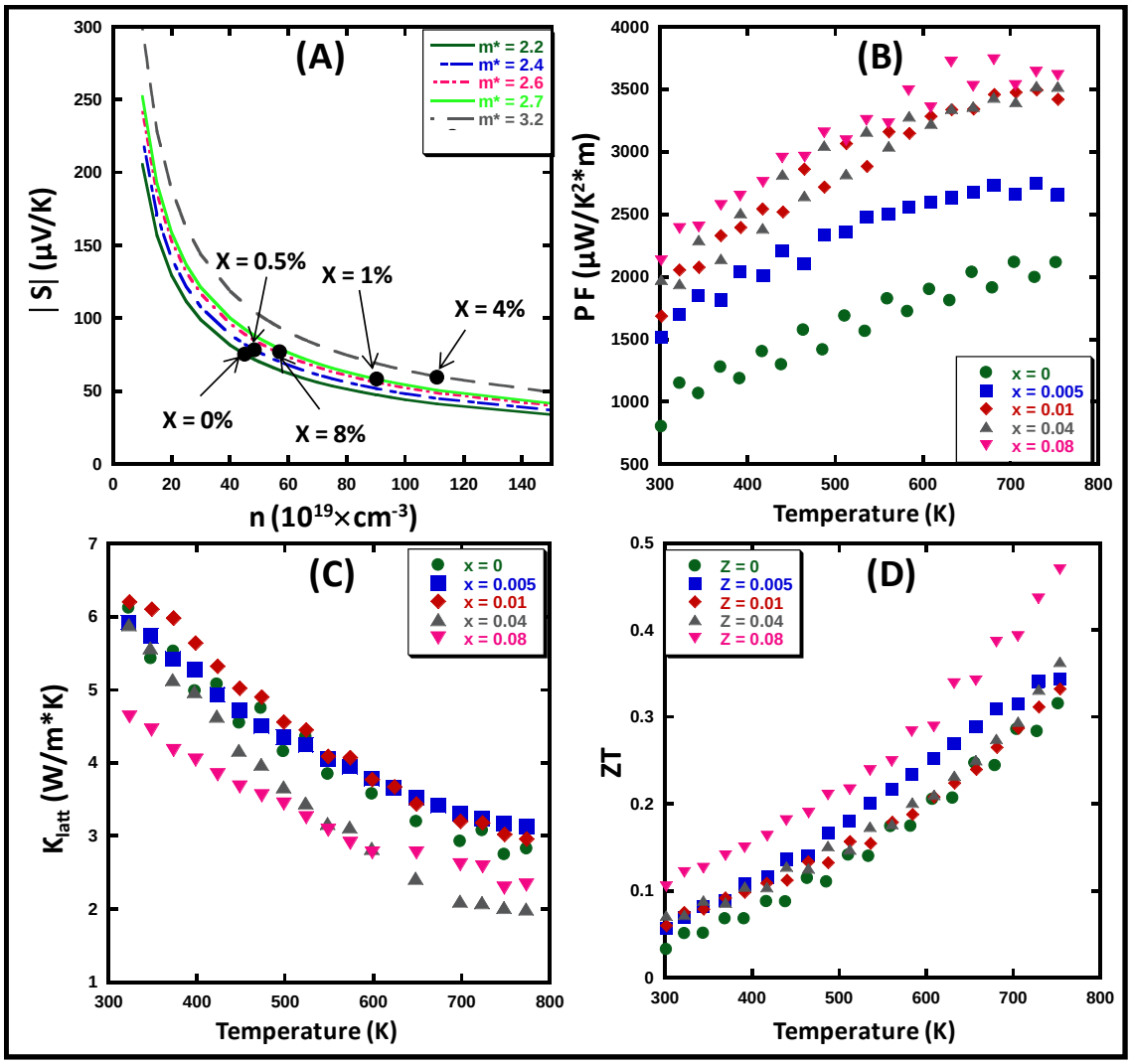

Figure 4.11 : Pisarenko plot and temperature dependence of the thermoelectric performance of $Ti_{0.15}Hf_{0.85}Ni_{1+x}Sn_{0.975}Sb_{0.025}$ nanocomposites. (A) Pisarenko plot showing large enhancements of the thermopower (S) due to simultaneous decrease in carrier concentration and increase in the carrier effective mass (m*) with increasing excess Ni. Temperature dependent (B) Power factor; (C) Lattice thermal conductivity; and (D) thermoelectric figure of merit (ZT) of HH(1-x)/FH(x) bulk nanocomposites (x= 0; 0.005;0.01; 0.04; 0.08).

To fully understand these surprising changes in the thermopower upon alteration of the effective carrier density of the $Ti_{0.15}Hf_{0.85}Ni_{1+x}Sn_{0.975}Sb_{0.025}$ (HH(1-x)/FH(x)) nanocomposites using FH quantum dots, we have constructed Pisarenko plots describing the relationship between the thermopower and carrier density for each of the $Ti_{0.15}Hf_{0.85}Ni_{1+x}Sn_{0.975}Sb_{0.025}$ (HH(1-x)/FH(x)) , $S = [(8\pi^2(k_B)^2)/3eh^2]m^*T(\pi/3n)^{2/3}$ (k_B is the Boltzmann constant, e is the carrier charge, h is the Planck's constant, m^* is the effective mass of the charge carrier, T is the absolute temperature, n is the carrier concentration), assuming parabolic bands and an energy independent relaxation time (Fig. 4.11A) [177]. This analysis has been done with the assumption that the thermopower at a given temperature can be described by a unique value of the effective mass (m*). Fig. 4.11A shows the Pisarenko plots (S versus n) at 300K for various $Ti_{0.15}Hf_{0.85}Ni_{1+x}Sn_{0.975}Sb_{0.025}$ (HH(1-x)/FH(x)) nanocomposites. No single value of the effective mass that allows fitting of all the data could be obtained, suggesting that the embedded FH quantum dots, in addition to reducing the effective carrier density within the $Ti_{0.1}Zr_{0.9}NiSn$ (HH) matrix, also significantly alter its electronic band structure close to the Fermi level. This is confirmed by remarkable variations in the carrier effective mass (m*) values extracted from the fitting of S(n) curves under the approximation of the parabolic bands and an energy independent relaxation time for each $Ti_{0.15}Hf_{0.85}Ni_{1+x}Sn_{0.975}Sb_{0.025}$ (HH(1-x)/FH(x)) nanocomposite. At 300K, the values of the effective mass are m* = 2.2, 2.4, 2.6, 2.7 and 3.2 for $Ti_{0.15}Hf_{0.85}Ni_{1+x}Sn_{0.975}Sb_{0.025}$ (HH(1-x)/FH(x)) nanocomposite with x = 0, 0.005, 0.01, 0.04 and 0.08, respectively (**Fig. 11A**). The observed trend reflects that the carrier effective mass (m*) increases with increasing mole fraction of FH quantum dots in the $Ti_{0.15}Hf_{0.85}NiSn_{0.975}Sb_{0.025}$ (HH) matrix. According to the relationship between S and m*, the thermopower should increase with the increase in effective

mass, but the composite with x= 0.01, 0.04 shows a decrease in thermopower which is due to their increased carrier density.

Fig. 4.9D shows carrier mobility in all $Ti_{0.1}Zr_{0.9}Ni_{1+x}Sn$ (HH(1-x)/FH(x)) nanocomposites which decreases almost linearly with rising temperature. The mobility of charge carriers in a conventional semiconductor is related to the relaxation time, τ, between scattering events (phonon−electron, ionized-impurity and electron−electron scattering, etc.) and the carrier effective mass (m*) by the equation $\mu = e(\tau/m^*)$. An increase in the relaxation time within the $Ti_{0.15}Hf_{0.85}Ni_{1+x}Sn_{0.975}Sb_{0.025}$ (HH(1-x)/FH(x)) nanocomposites can be attributed to the drop in the effective carrier density arising from the trapping at 300K, of low energy carriers by the potential barrier, $\triangle E$ at the HH/FH interfaces (Fig. 4.10B). Such reduction in the effective carrier density implies a reduction in the frequency of electron-electron collisions leading to a larger relaxation time between scattering events. This event can be well explained for HH (92%)/FH(8%),which shows the highest effective mass of 3.2 and the least mobility. However, this reduction in the frequency of electron-electron collisions alone does not explain why the observed carrier mobility within the HH(99.5%)/FH(0.5%),HH(99%)/FH(1%) and HH (94%)/FH(6 %) nanocomposites are larger than the HH matrix values. This suggests that additional contributing factors such as charge carrier – ionized impurity scattering and charge carrier scattering by structural defects (dislocations, vacancies) play a significant role in the alteration of the relaxation time within $Ti_{0.15}Hf_{0.85}Ni_{1+x}Sn_{0.975}Sb_{0.02}$ (HH(1-x)/FH(x)) nanocomposites.

Figure 4.9C describes the temperature dependence of electrical conductivities of the $Ti_{0.15}Hf_{0.85}Ni_{1+x}Sn_{0.975}Sb_{0.02}$ (HH(1-x)/FH(x)) nanocomposites. A monotonic increase in electrical conductivity with the increase in the temperature has been observed for all the

nanocomposites. This is a typical semiconducting behavior. With the increase in FH content, the electrical conductivities have been increased. The observed trend in electrical conductivities contradicts the results of the previously reported results by Hohl et al, who suggested that the electrical conductivity should decrease with increase in FH content. As they prepared the samples via arc-melting and annealing, the sample suffered a high range of scattering events of charge carriers due to the large number of structural defects contributed by the process of arc melting. In our current study as the high temperature liquid state mediated solid state technique has been employed, sufficient time has been permitted to the product for the formation of well crystallized HH and FH phases. As both of the phases has structural similarities, the equivalence in lattice parameters favors the formation of coherent HH/FH interfaces which minimizes scattering of charge carriers in the composites. Although there is always an increase in the electrical conductivities of the HH/FH nanocomposites with respect to the HH matrix, but the trend is somewhat peculiar. At 300K, the sample HH (96%)/FH(4%) shows about 180% enhancement from the HH matrix ,whereas the sample HH (92%)/FH(8%) shows only 80% enhancement-which should be greater than the earlier as predicted. This can be explained by the lower carrier mobility as shown in Fig 4.9D.

The temperature dependence of the power factor of $Ti_{0.15}Hf_{0.85}Ni_{1+x}Sn_{0.975}Sb_{0.025}$ (HH(1-x)/FH(x)) nanocomposites is shown in Fig. 4.11B. The power factors of the composites seems to increase rapidly with the increase in temperature. At highest temperature 775K, the composition HH (92%)/FH(8%) showed highest power factor of about 69% increase from the HH matrix. Although the same sample showed somewhat laid back electronic properties in comparison to the other compositions (e.g 1% and 4%) which was not in favor of a good thermoelectric material, but the marginal decrease in the lattice thermal conductivities (Fig. 4.11C), helped it to

compensate for the rest of the drawbacks. Another important result in this study is the ability of the embedded FH nanostructures to scatter thermal phonons to reduce the thermal conductivity of the synthesized $Ti_{0.15}Hf_{0.85}Ni_{1+x}Sn_{0.975}Sb_{0.025}$ (HH(1-x)/FH(x)) nanocomposites. Fig. 4.11 C shows the temperature dependence of the lattice thermal conductivity (κ_L) obtained by subtracting the electronic component κ_e from the total thermal conductivity,κ. The electronic component was estimated by using the Wiedemann-Franz law ($\kappa_e = L_o\sigma T$) where the Lorenz number taken as its fully degenerate value of $L_o = 2.45 \times 10^{-8}$ $W\Omega K^{-2}$. The lattice thermal conductivities of the nanocomposites with 0.5 and 1 mole % FH were almost comparable to the matrix thermal conductivities throughout the temperature range . The sample with 4 and 8 mole % shows a marginal decrease at all temperatures. The lattice thermal conductivity of the 4 % nanocomposite shows almost the same value as of HH matrix at 300K which gradually decreases to 33% at 775 K. For the 8% the lattice thermal conductivity is almost 20% lower than that of the HH matrix at 300K and gradually decreases and shows up to 33% reduction upon reaching at 775K. The observed trend of reductions in the thermal conductivities of the $Ti_{0.15}Hf_{0.85}Ni_{1+x}Sn_{0.975}Sb_{0.025}$ (HH (1-x)/FH(x)) nanocomposites are due to the enhancement of thermal phonons scattering by the multiple nanometer scale HH/FH phase boundaries introduced by the insertion of FH quantum dots within the HH matrix, in addition to the mid- to long-wavelength phonons scattering at grains boundaries.

Finally, the simultaneous large enhancements in the power factor and the associated reductions in the lattice thermal conductivity of $Ti_{0.15}Hf_{0.85}Ni_{1+x}Sn_{0.975}Sb_{0.025}$ (HH(1-x)/FH(x)) nanocomposites, result in drastic improvements in their thermoelectric figure of merit ZT when compared to the $Ti_{0.15}Hf_{0.85}NiSn_{0.975}Sb_{0.025}$ (HH) matrix (Fig. 4.11D). As shown, the HH matrix is having the ZT ~ 0.32 at 775K, whereas it is found that presence of 8 mole% of FH as

nanoinclusion within the crystal lattice of the semiconducting HH matrix dramatically enhances the thermoelectric performance of the resulting HH(92%)/FH(8%) nanocomposite to ZT ~ 0.5 at 775K, a factor of 1.5 times higher ZT as compared to the $Ti_{0.15}Hf_{0.85}NiSn_{0.975}Sb_{0.025}$ (HH) matrix.

4.5 Conclusions

In summary, for the part of work on p-type nanocomposite,it has been demonstrated the effectiveness of coherently embedded FH nanoinclusions in boosting the thermopower and hole carrier mobility in a heavily doped p-type HH matrix, without increasing the total thermal conductivity. This results in a large enhancement in the thermoelectric figure of merit of the resulting HH(1-x)/FH(x) nanocomposites when compared to the nanostructure-free HH matrix. The observed large increase in the thermopower is associated with a large reduction in the effective carrier density and an increase in the carrier effective mass. This alteration of the electronic behavior of charge carriers in the p-type HH matrix is attributed to the formation of a type-II heterojunction at the interface between the HH matrix and FH nanoinclusions. The energy offset of the valence band maximum (VBM) of both the HH matrix and FH inclusions is believed to act as an energy filter for holes within the VB of the HH matrix. Within this band diagram picture, carriers with energy higher than the potential barrier heights (high energy carriers) are transmitted to the VB of FH nanoinclusions, whereas carriers with energy lower than the potential barrier are trapped at the HH/FH interfaces and require additional thermal energy to cross the potential barrier. The large enhancement in the carrier mobility ($\mu = e(\tau/m^*)$) is ascribed to an increase in the mean relaxation time (τ) resulting from a reduction in the frequency of carrier–carrier scattering events due to the reduction of the effective carrier density, and due to a decrease in ionized-impurity scattering of charge carriers arising from their spatial

separation by the FH nanoinclusions, and from the higher mobility of high energy carriers participating in the transport process. The above results clearly show that atomic-scale engineering of the crystal structure of a p-type semiconductor matrix using carefully selected nanostructures can boost the thermopower and carrier mobility without increasing the thermal conductivity and thus improve the figure of merit.

In the second part of study for the n type nanocomposite, we observed that the nanostructure coherently embedded within a semiconducting matrix, tune the electronic behavior of existing charge carriers within the matrix, leading to a spectacular increase in the thermopower as well as a large enhancement in the carrier mobility within the resulting bulk nanocomposite. This approach effectively helped to decrease the carrier density and the increase in the carrier effective mass within the HH/FH-QD nanocomposites which contributes towards a larger thermopower. These carriers also helped to build up dramatic increase in the electrical conductivities. The discovery of this atomic engineering on the nanoscale to enhance thermopower and carrier mobility is expected to give a boost to the figures of merit in thermoelectric materials intended for high performance energy conversion application.

Chapter 5

EFFECT OF MECHANICAL ALLOYING ON THE THERMOELECTRIC PROPERTIES OF HALF-HEUSLER NANOCOMPOSITES

5.1 Overview

In our previous studies on half-Heusler alloys, it has been observed that the in-situ nanostructures play a vital role in tuning its thermoelectric properties. These in-situ nanostructures were prepared within the bulk via high temperature liquid state mediated solid state diffusion. As mentioned earlier, this method could efficiently enhanced the material performances as compared to the melting processes[190] as the high temperature and time longevity allows the formation of well crystallized HH (bulk) and FH (nano) phases. However, solid-state diffusion does have its own sets of shortcomings. The kinetics of solid-solid reactions is much more complicated as the process moves through several stages where polycrystalline nature of the reactants, mismatch in reactant/product geometry, phase immiscibility and multiple products obtained at individual stages disrupt the reaction kinetics.[191,192] Therefore, it hardly obeys the homogeneous kinetics which is more controlled and predictable. Often the reaction ends up with compositionally inhomogeneous products, technically the "phase impurities". Besides, it might not give desired microstructure rather an incomplete reaction. Since

we need to, restore as well as optimize the solid state diffusion method, mechanical alloying proved to be a potential candidate to solve this issue.

Mechanical alloying is an extension of the liquid state mediated solid state diffusion method which is used to prepare various composite metal powders via both the equilibrium and metastable phases. It is a powder processing technique which proceeds through interdispersion of its participating components via repeated fracture of the free powder particle with successive cold welding of those fractured component [193] resulting in a wide range of equilibrium and non-equilibrium alloy phases. These non –equilibrium phases are mostly recognized as solid solutions, metastable crystalline and quasicrystalline phases ,and most importantly the "nanoinclusions" which is the motivation for the current study[194].

Since mid 1980s, several attempts have been made to synthesize a wide range of alloy phases using the mechanical alloying process.[195-201] It has the unique ability to initiate chemical reactions in powder mixtures at relatively low although most of metals have high melting points.In our previous efforts, we were able to synthesize the HH-FH system, but at times the solids state diffusion does not provide sufficient energy for the completion of the reaction. As a result, we could find some unreacted elements as well as metastable phases. To avoid the situation, repeated heat treatment could help, but this may take longer processing time. As we want to keep the nanostructure intact within the HH matrix, longer annealing could be detrimental for the desired thermoelectric properties due to the growth of nanostructures into microstructures, So mechanical alloying could be a suitable alternative, being a quick process (~ few hours) as well as assisting in the formation of uniformly size and well-dispersed nanostructures. To ensure the contribution of "mechanical alloying" into our traditional high temperature liquid state mediated solid state diffusion method, a comparative study has been

done with the n –type $Ti_{0.4}Hf_{0.6}Ni_{1+z}Sb_{0.975}Sn_{0.025}$ **(**HH(1-z)/FH(z)) bulk nanocomposites. Here part of the samples have undergone only high temperature liquid state mediated solid state diffusion process while the remaining parts have been mechanically alloyed in addition to the high temperature solid state diffusion.The respective thermoelectric measurements have performed and compared.

5.2 Experimental

5.2.1 Synthesis

Fabrication of bulk semiconducting HH alloys with integrated metallic FH nanostructures, several alloys with various excess of Ni calculated following the general formula $Ti_{0.4}Hf_{0.6}Ni_{1+z}Sb_{0.975}Sn_{0.025}$ (z = 0, 0.005, 0.01, 0.02, 0.03) were prepared by direct liquid state mediated solid state reaction of stoichiometric amounts (total mass = 10.0 g) of the constituent elements in fused silica ampoules as described in chapter 4.The recovered samples were thoroughly mixed using an agate mortar and pestle under an inert Ar-atmosphere and divided into two equal portions. One half of the sample were further underwent 2 hrs of high energy ball milling in SPEX shaker ball mill, whereas the other half were consolidated into pellets (without the ball-milling procedure) for further characterization. The ball milled samples were recovered and consolidated into pellets under similar conditions as the other half. For both halves of the bulk nanocomposites, samples containing various fractions of FH nanoinclusions embedded within the bulk HH matrix were formed accordingly with the chemical equation (1).

$0.4Ti + 0.6Hf + (1+z)\ Ni + 0.975Sn + 0.025\ Sb \rightarrow (1-z)\ Ti_{0.4}Hf_{0.6}NiSn_{0.975}Sb_{0.025}$ (HH) + z $Ti_{0.4}Hf_{0.6}Ni_2Sn_{0.975}Sb_{0.025}$ (FH) (1)

5.2.1 Characterization

The constituent phases of the as-prepared and the ball milled materials were evaluated by powder X-ray diffraction on a PANalytical X'pert Pro powder diffractometer operating under 40 kV and 40 mA using a Cu Kα radiation source. The transmission electron microscopy (TEM) study of selected specimens cut from pressed pellets was performed with JEOL JEM-3011 to probe the size and the distribution of FH nanoinclusions embedded within the HH matrix as well as the interface boundary between HH and FH phases. Details on TEM sample preparation are described in chapter-4 . Seebeck coefficient and electrical resistivity were measured simultaneously from room temperature to 500°C under a low pressure He atmosphere using a commercial ZEM-3 system from ULVAC-RIKO. The instrument precision on the electrical resistivity and Seebeck coefficient data is ±4%. The thermal conductivity was calculated from the thermal diffusivity data measured by the laser flash method (LINESIS-1000 from) from 30°C to 500°C under flowing N_2 gas (>30 mL/min). The instrument precision on the thermal diffusivity data is ±6%. .

5.3 Result and Discussion

In rest of this chapter, part of the sample that undergone the additional ball milling step would be suffixed as "–BM" to clearly differentiate between samples which underwent both liquid state mediated solid state and ball milling as opposed to those which were only processed through solid state.

5.3.1 Structural characterization

The powder X-ray diffraction (PXRD) patterns of the synthesized $Ti_{0.4}Hf_{0.6}Ni_{1+z}Sb_{0.975}Sn_{0.025}$ **(**HH (1-z)/FH(z)) are shown in Fig 5.1 where (A) represents the solid state only sample and (B) represents the sample processed via solid sate synthesis followed by 2 hours ball milling. All the peaks of the HH matrix pattern were indexed to cubic MgAgAs type structure. It does have few additional peaks which corresponds to the Ni_3Sn_4 phases (marked with *) which encourages the belief of incompletion of the liquid state mediated solid state reaction. But, Fig 5.1(B) shows no additional peaks suggesting the absence of the unreacted elements within the samples. The absence of the FH peaks, which was found in the earlier PXRD patterns, could be understood as the reduction in the size of the FH particles which made these phase to be undetectable from the PXRD measurements. This difference in the PXRD pattern for the similar batch of the sample strongly suggests that the introduction of the ball milling step necessarily helped to complete the reaction as well as provide the ambient condition for major production of nanostructures. The surface activation of the fine particles obtained due to high energy ball milling seems to be the key to facilitate the diffusion process and the formation of the single phase $Ti_{0.4}Hf_{0.6}Ni_{1+z}Sb_{0.975}Sn_{0.025}$ nanocomposites.

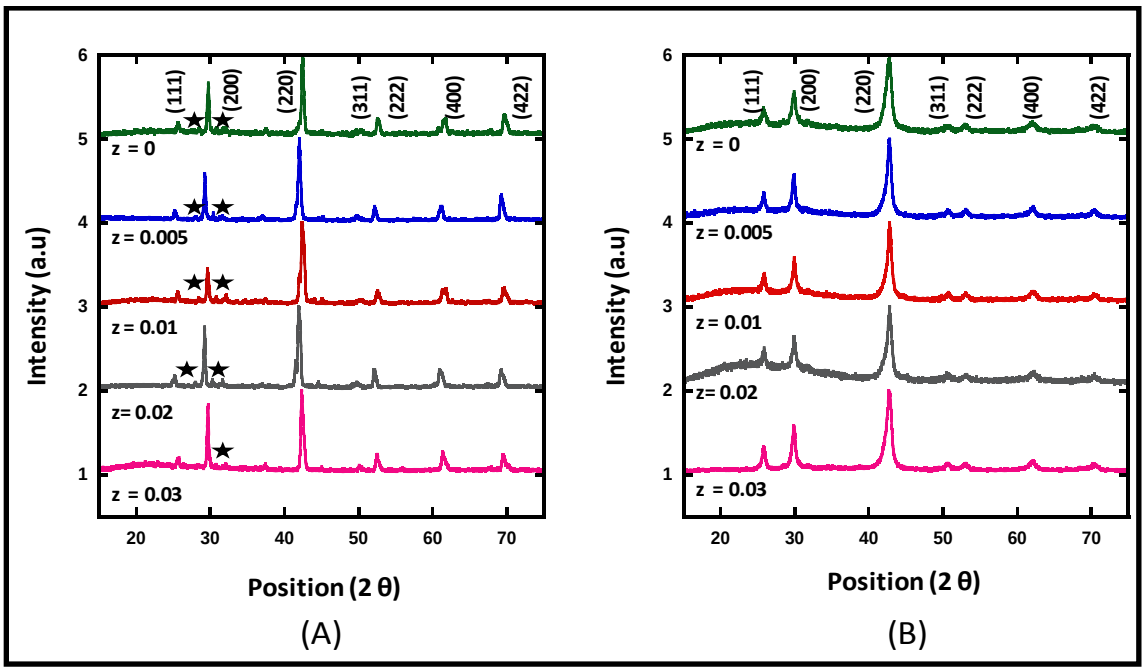

Figure 5.6 (A) X-ray powder diffraction patterns of solid state only $Ti_{0.4}Hf_{0.6}Ni_{1+z}Sb_{0.975}Sn_{0.025}$ ($0 \leq z \leq 0.03$) half-Heusler alloys with few tiny peaks of Ni_3Sn_4 (*) minority impurities.**(B)** Single phase sample obtained from the same series of samples with an additional ball milling step. The non-existence of any peaks from FH, for both of the samples, suggests the presence of sub-nanometer scale precipitates, which is not observed in the PXRD as these are too small to diffract..

Careful investigation of the low magnification (TEM) image revealed the presence of small spherical precipitates randomly dispersed within the HH matrix (Figure 5.2A) for the solid state sample, whereas high resolution image of ball milled sample showed a more uniform dispersion of nanometer-scale (~20 nm) grains of the of the HH matrix within which spherical particles of the FH inclusion can be observed (Figure 5.2B). These spherical particles are recognized as the FH particles whose formations were explained in chapter -4. This interesting difference in the

size of HH grains and the distribution of the FH component can be attributed to the milling process,

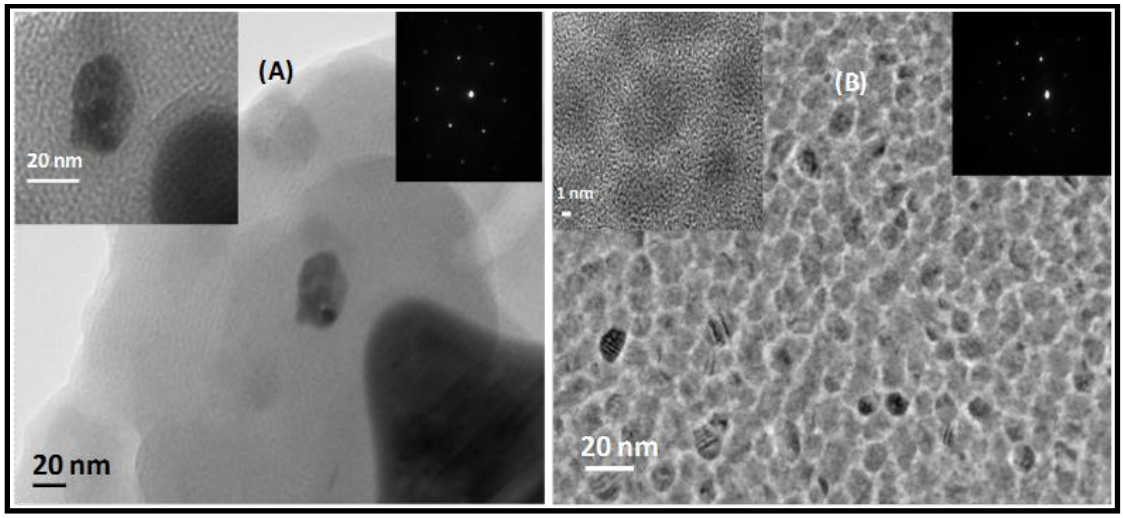

Figure 5.2: (A) TEM images of a hot pressed pellet of HH/FH(3%) bulk composite made by solid state only showing nanometer scale particles of FH in micrometer scale grains of HH matrix. The size of the spherical FH precipitates is around 18 nm and the electron diffraction pattern of the FH particle confirmed the FCC structure of FH (inset); **(B)** High resolution image of a sample with similar composition HH/FH(3%) but, with additional ball milling step showing the fine features revealed details of the grain boundary of the HH/FH grains. Each grain contains very small spherical FH precipitates with particles size around 5 nm. Electron diffraction pattern of the FH regions also showed the FCC (inset).

which is believed to control the kinetics of the reaction and resulting in the formation of small uniform grains of the HH matrix and well defined FH nanostructures. Inset in Fig 5.2(A) shows the low magnification image of a randomly selected single particle, which shows a FH particle size of 20 nm, while the inset in Fig 5.2(B) shows the ball milled sample has reduced the grains size of the HH matrix to the size range of about 15-30 nm, as well as decreasing the particle size of FH inclusion to about 5-8 nm. It helps to understand the fact that milling also contribute

toward reducing the particle size of bulk HH matrix. Selected area electron diffraction (SAED) patterns shown (as inset) for both of the samples confirm that the FH inclusions have face centered cubic lattice.

5.3.2 Thermoelectric properties

The temperature dependence of the total thermal conductivities of the HH(1-z)/FH(z) composites are shown in Fig 5.3(A) and (B) for the solid state and ball milled sample, respectively. The total thermal conductivity(κ_{total}) of the HH matrix for solid state sample at 300 K is ~ 4W/mK, which slightly increases with increasing temperature and gained a value of 4.3 W/mK at 775K. At the same time the total thermal conductivity value for the HH matrix after ball milling is comparatively higher at 300K with a value of 7.8W/mK. However, the κ_{total} of this sample, in contrary to the solid state sample, gradually decreases with rising temperature to 6.4W/mK at 775K.The lattice thermal conductivities of the matrices shown in Fig 5.3(C) and (D) are comparable at all temperatures. The higher value of the total thermal conductivity of the ball milled HH matrix results from the combination of the increased electronic thermal conductivity, κ_e (due to increased electrical conductivity) and comparable lattice thermal conductivity, $\kappa_{l.}$ generally, the thermal conductivity of a material in expected to decrease with the increase in nanostructuring due to the fact that nanostructuring enhances the phonon scattering. For the solid state samples, we can observe that the total thermal conductivity increases with increasing content of FH nanoinclusion, which is opposite to the predicted trend. Although the $\kappa_{l.}$ show similar trend, looking at the electrical conductivity data Fig 5.3(E) indicates that the electrical conductivity trend largely influences the total thermal conductivities. This effect gets even more evident with the ball milled sample. Here we can observe that the thermal conductivity decreases

with increasing percentage of FH nanoinclusions which leads us to believe that nanostructuring affects the thermal conductivity. However, the lattice thermal conductivities values which shows almost equal values irrespective of the % of FH inclusion, made the effect of nanostructuring questionable. To understand the mechanism behind this unusual trend, the electrical conductivity plot helps explain that for both systems the electronic thermal conductivity is actually contributing towards the total thermal conductivities with very less influence than that of nanostructuring.

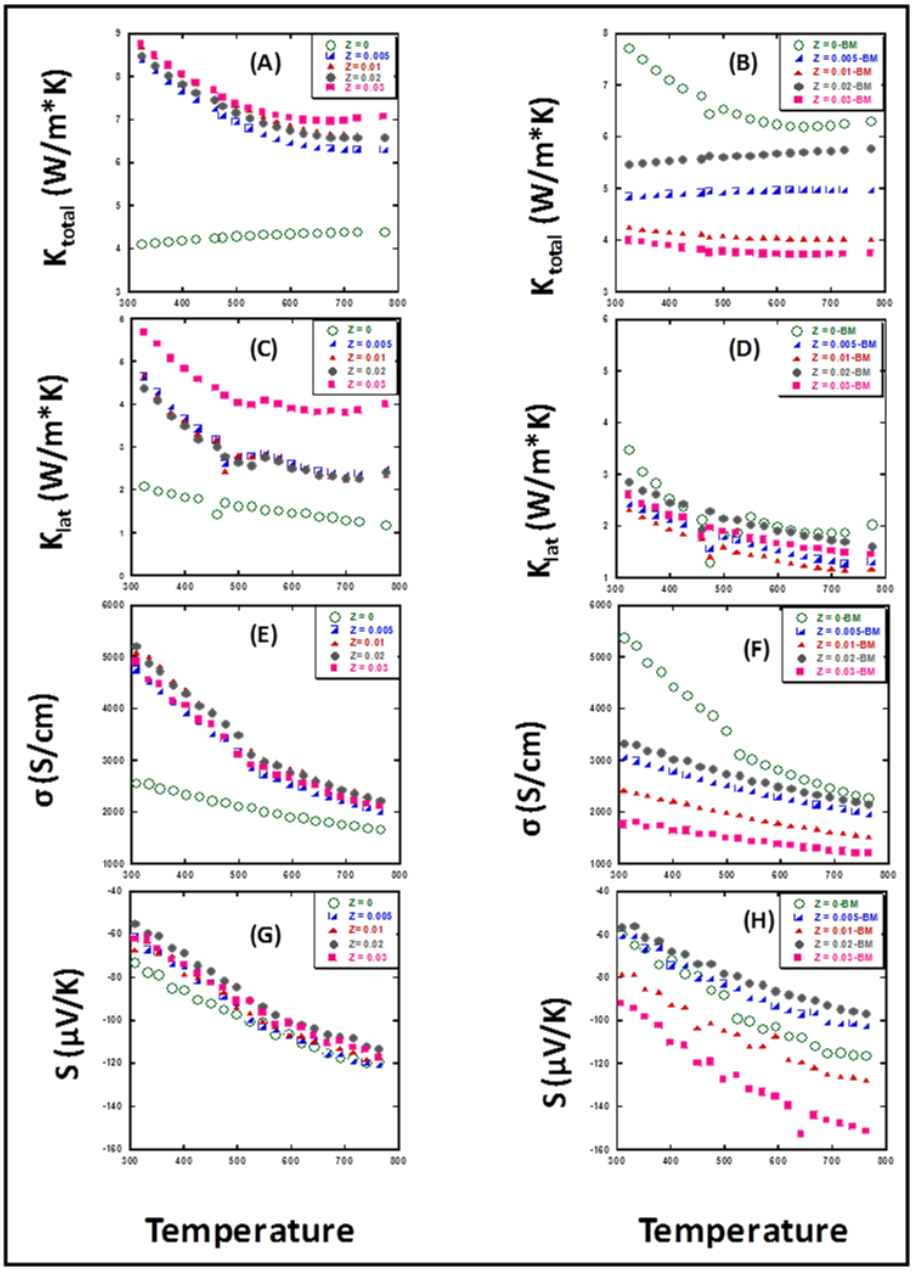

Figure 5.7 : Temperature dependence of the electronic properties of HH(1-z)/FH(z) bulk nanocomposites (z =0,0.005,0.01,0.02,0.03) of $Ti_{0.4}Hf_{0.6}Ni_{1+z}Sb_{0.975}Sn_{0.025}$ system synthesized by solid state only and ball milling respectively : (A,B) Total thermal conductivities ; (C,D) Lattice thermal conductivities ;(E,F) Electrical conductivity; (G,H) Thermopower.

Fig. 5.3 (E) shows the temperature dependence of the electrical conductivities of the solid state only sample where all the samples with excess Ni shows about 100% enhancement with respect to the matrix with no excess Ni. This effect can be explained by the fact that increased amount of metallic Ni provides more charge carriers to the system which in turn increases the electrical conductivity of the HH matrix. Fig. 5.3 (F) shows exactly the inverse trend for the ball milled samples, where the HH matrix shows the maximum electrical conductivities and the value further decreases with the addition of excess Ni. For such type of trend, the method of synthesis plays a pivotal role. As ball milling introduces more nanostructures, a quantum confinement effect arises which dominates the metallic behavior of excess Ni. According to the quantum confinement effect, the nanostrctures within a material always tends to increase the band gap of the material. Even though excess Ni provides more carriers to the system, the increase in the band gap can be wide enough to restrict the charge carriers to move from valence band to the conduction band results in decreased electrical conductivities. The behavior of charge carriers density under this circumstance can be further explained by observing the thermopower (Seebeck) of the material in Fig.5.3 (G) and (F). All samples showed negative value of thermopower indicating n-type conducting behavior in the measured temperature range Fig. 5.3(G) shows the thermopower for solid state only sample which increases with temperature regardless of the mole fraction of nanoinclusions However it remains almost the same for all the compositions including the matrix at all temperatures. As we know, thermopower greatly depends on the number of charge carriers (here electrons), Therefore similar values of thermopower signify that the density of charge carriers remained unaffected during addition of excess Ni (or increasing the mole fraction of FH nanoinclusion). However, the electrical conductivity of the matrix is different from than the rest of the composition. As the electrical

conductivity depends on both the density of charge carriers and carrier mobility, different electrical conductivities and fixed number of charge carriers implies that there is a difference in the carrier mobility between the matrix and HH-FH nanocomposites. This effect can be further confirmed by measuring the Hall Effect on the samples which will be done in the future work for this study. On the other hand,the ball mill samples show an increase in the with the increase in amount of FH nanoinclusions. Although the samples with HH(99.5%)/FH(0.5%) and HH(98%)/FH(2%) showed little ambiguity as their values are similar at 300K and decreases as the temperature increases, the rest of the samples shows an increased thermopower with increase in FH nanoinclusion with respect to the matrix. As these samples have lower electrical conductivities than the matrix and higher thermopower than the matrix, it is pretty straight forward from the relation (2) that the number of charge carrier has decreased with the increase in the concentration of FH inclusion.

$$\mathbf{S} = \frac{\mathbf{8\pi^2\kappa^2 T}}{\mathbf{3eh^2}}\ \mathbf{m}^*\ \left(\frac{\boldsymbol{\pi}}{\mathbf{3n}}\right)^{\frac{2}{3}} \quad \text{..... (2)}$$

where S is the thermopower and "n" stands for carrier concentration.

The temperature dependence of the power factor is shown in Fig.5.4 (A) for the solid state only samples, which reveals a gradual increase in the power factor with increasing temperature regardless the mole fraction of the FH inclusion. Similar trends have also been observed for the ball milled samples in Fig.5.4(B). For both series the power factor is mostly dominated by the electrical conductivity trend. The temperature dependence of figure of merit (ZT) for solid state only samples is shown in Fig.5.3 (C). At 300 K the matrix shows around ZT~0.1, which increases with the temperature and reaches a value around 0.41 at 775K. The rest of the

nanocomposites show almost the same ZT value of 0.07 at 300 K and 0.35 at 775 K. Fig.5.3 (D) shows the ZT values of the ball milled samples. Although the matrix showed higher electrical conductivities and power factor, the high thermal conductivity and intermediate Seebeck, reduce the final ZT to 0.08 at 300K and 0.38 at 775K. However, the HH(97%)/FH(3%) nanocomposite showed the highest ZT value of about 0.12 at 300K, which gradually increased up to 0.6 at 775K. This corresponds to around 58% enhancement in ZT compared to that of matrix. The large ZT for the HH(97%)/FH(3%) nanocomposite is mainly contributed by lower thermal conductivity and higher Seebeck.

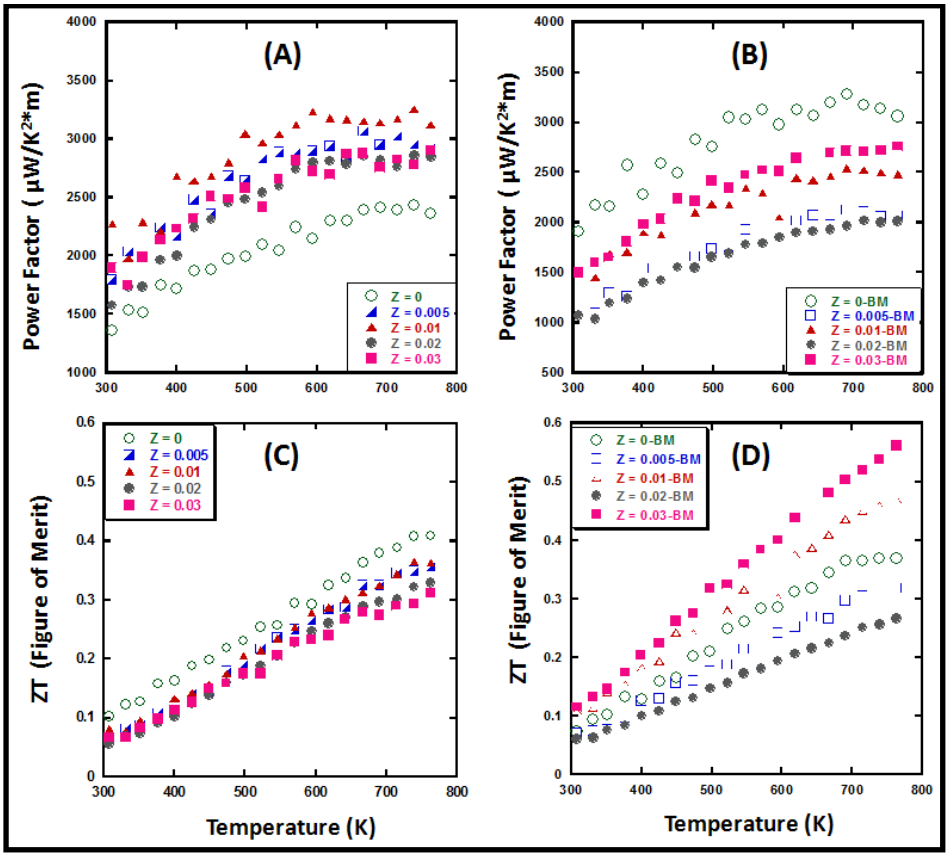

Figure 5. 8 : Temperature dependence of the Power Factor (A and B) and Figure of Merit (C and D) of HH(1-z)/FH(z) bulk nanocomposites (z= 0, 0.005, 0.01, 0.02, 0.03) of $Ti_{0.4}Hf_{0.6}Ni_{1+z}Sb_{0.975}Sn_{0.025}$ after solid state only and after solid state followed by ball milling, respectively.

5.4 Conclusions

In the current chapter comparisons have been done for the n –type $Ti_{0.4}Hf_{0.6}Ni_{1+x}Sb_{0.975}Sn_{0.025}$ **(**HH(1-x)/FH(x)) bulk nanocomposites synthesized by two different techniques (i,e.liquid state mediated solid state reaction and liquid state mediated solid state along with the mechanical alloying) starting with the same batch of material. This study reveals that introduction of mechanical alloying enhances the thermoelectric properties to a greater extent. This additional step of alloying not only enables the completion of the reaction process, it also produces more uniform and well dispersed nanostructures within the material. These nanostructures play a vital role in tuning the thermoelectric properties of the material by changing the band gap, which in turn alters the concentration of charge carrier as well as their mobility. Future investigations on Hall Effect, is expected to shed more light on the electron transport mechanism. Transmission electron microscopy also reveals the uniform nanostructures produced within the matrix, which controlled the properties of the material. Finally the ball milled sample HH(97%)/FH(3%) nanocomposites has shown the highest ZT of about 0.6 at 775K, which is about 58% enhancement in comparison to the highest ZT obtained via solid state only samples.

Chapter 6

STUDIES ON THERMOELECTRIC PROPERTIES OF COPPER SELENIDE SYSTEM

6.1 Overview

In recent years, several concepts have been proposed to understand different factors that are responsible for the enhancement of the thermoelectric energy conversion efficiency of different classes of materials. The PGEC (Phonon Glass Electron Crystal) concept is one of the exciting approaches amongst all. For a good thermoelectric material, one should have good electronic property as well as low thermal conductivities [202]. So with this approach, a crystalline semiconductor has the ability to combine good electronic properties with low thermal conductivity due to heavily disordered atomic arrangement. As a result, it has a great potential to be a good thermoelectric material. Skutterudites [29] and clathrates [203] are excellent examples. Besides the PGEC concept, other approaches such as nanostructuring[204-207], introduction of resonant impurities[167] and electron-phonon coupling [208] have been proved as path breaking innovations. Another important example of such approach is the use of lamella crystals as a thermoelectric material which usually bears a high lattice thermal conductivity. Studies have revealed that by reducing the thickness in case of the crystalline layers and creating disorders at

the interface of these layers can effectively reduce the lattice thermal conductivity[208]. Based on this concept, studies on the structure and properties of Cu_2Se are gaining wide attention as it has proven to be an ideal thermoelectric material [1,209]. Since the β-phase Cu_2Se crystallizes as a lamellar structure (Fig 6.1), the monoatomic Se layers act as ordered lamella and Cu atoms are randomly distributed t creating disorder lamella, which eventually helps in a greater reduction in the thermal conductivities. In the current chapter, effort has been made to explore various routes to synthesize and characterize the Cu_2Se phases.

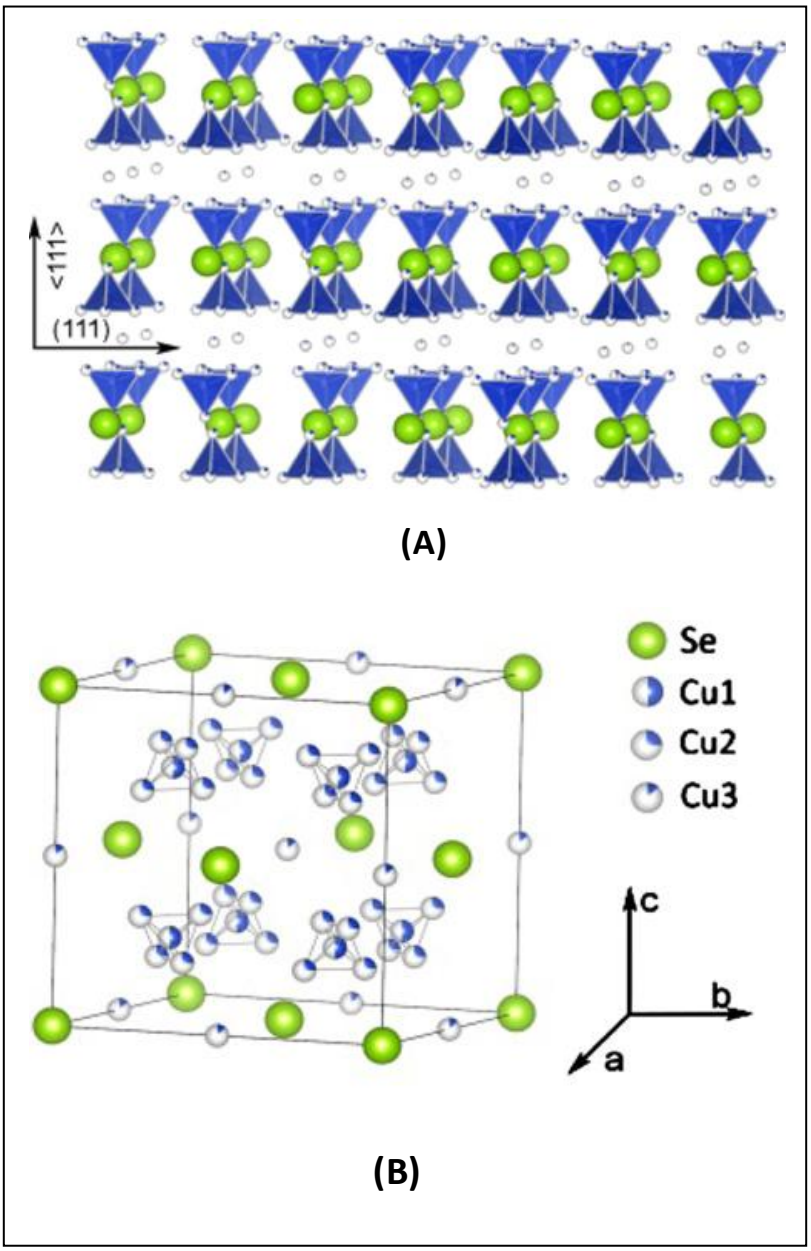

Figure 6.1 : Crystal structure of cubic β-phase Cu_2Se. (A) View of (111) plane. (B) Face Centered Cubic unit cell showing the positions of Cu atoms at (0.25,0.25,0.25), (0.315,0.315,0.315) and (0.5,0.5,0.5) along <1 1 1 > direction[1].

6.2 Thermoelectric properties of $Cu_{1+x}Se_2$ (x = 2.45, 2.5, 2.75, 2.80, 2.90, 2.95, 3.0) synthesized via high temperature liquid state mediated solid state reaction

6.2.1: Synthesis

Various amount of elemental Cu and Se were used to produce a series of $CuSe_2/Cu_4Se_2$ composites with general formula $Cu_{1+x}Se_2$ (x = 2.45, 2.5, 2.75, 2.80, 2.90, 2.95, 3.0). In the synthesis, Cu powder (Alfa Aesar, 99.5%) and Selenium powder (Strem chemicals, 99.9%) elements with different compositions were weighed stiochiometrically, ground under inert atmosphere and sealed in a quartz tube under vacuum. Then the vacuum sealed samples were melted at 1150 ^oC for 2 hours and then annealed at 800 ^oC for 8 days and cooled down to room temperature using a vertical high temperature furnace. The resulting ingots were ground into powders and further consolidated at 437 ^oC via spark plasma sintering.

Similar amount of elemental Cu and Se were used to produce a series of $CuSe_2/Cu_4Se_2$ composites with general formula $Cu_{1+x}Se_2$ (x = 2.45, 2.5, 2.75, 2.80, 2.90,3.0) as used for the solid-state method. In the synthesis, Cu powder (Alfa Aesar, 99.5%) and Selenium powder (Strem chemicals, 99.9%) elements with different compositions were weighed stiochiometrically and loaded in stainless steel jars under inert atmosphere and sealed in a glove box. Then the powder loaded jars were taken out of the glove box and placed in a planetary ball mill for 12 hours. After 12 hours, the jars were taken out of the mill and opened under inert atmosphere . The aim was to activate the powders well, which can initiate a uniform reaction. The resulting ingots were further consolidated at 437 ^oC via spark plasma sintering.

Another batch of $CuSe_2/Cu_4Se_2$ composites with general formula $Cu_{1+x}Se_2$ (x = 2.45, 2.5, 2.75, 2.80, 2.90,3.0) were synthesized from $CuSe_2$ and addition of elemental Cu rather than using

elemental Cu and Se individually as earlier. In the first step, the $CuSe_2$ was made by using elemental Cu and Se via ball milling for 74 hours in a planetary ball mill. In the next step, additional Cu was added to the $CuSe_2$ stiochiometrically to form the final composition via subsequent 12 hours ball milling in planetary ball mill. The reaction follows the following mechanism.

Step 1 : $Cu + 2\ Se = CuSe_2$

Step 2 : $CuSe_2 + x\ Cu = Cu_{1+x}Se_2$

The products were recovered and processed further for characterizations.

6.2.2: Characterizations

The structures of the synthesized $Cu_{1+x}Se_2$ (x = 2.45, 2.5, 2.75, 2.80, 2.90, 2.95, 3.0) were investigated using a monochromated CuKα radiation on a Rigaku rotating anode powder X-ray diffractometer. The $Cu_{1+x}Se_2$ powders were characterized by differential scanning calorimeter (Netzsch DSC 404F3) to verify the phase purity. Seebeck coefficient and electrical resistivity were measured from room temperature to 500°C under a low pressure He atmosphere using a commercial ZEM-3 system from ULVAC-RIKO. The instrument precision for the electrical resistivity and Seebeck coefficient data is ±4%. The thermal conductivity was calculated from the thermal diffusivity data measured by the laser flash method (LINSEIS 1000) from room temperature to 500°C under flowing N_2 gas .The instrument precision for the thermal diffusivity data is ±6%. A Pyroceram reference material was measured alongside each sample and C_p values for thermal conductivity calculations were extracted from the laser flash data.

6.2.3: Results and discussions

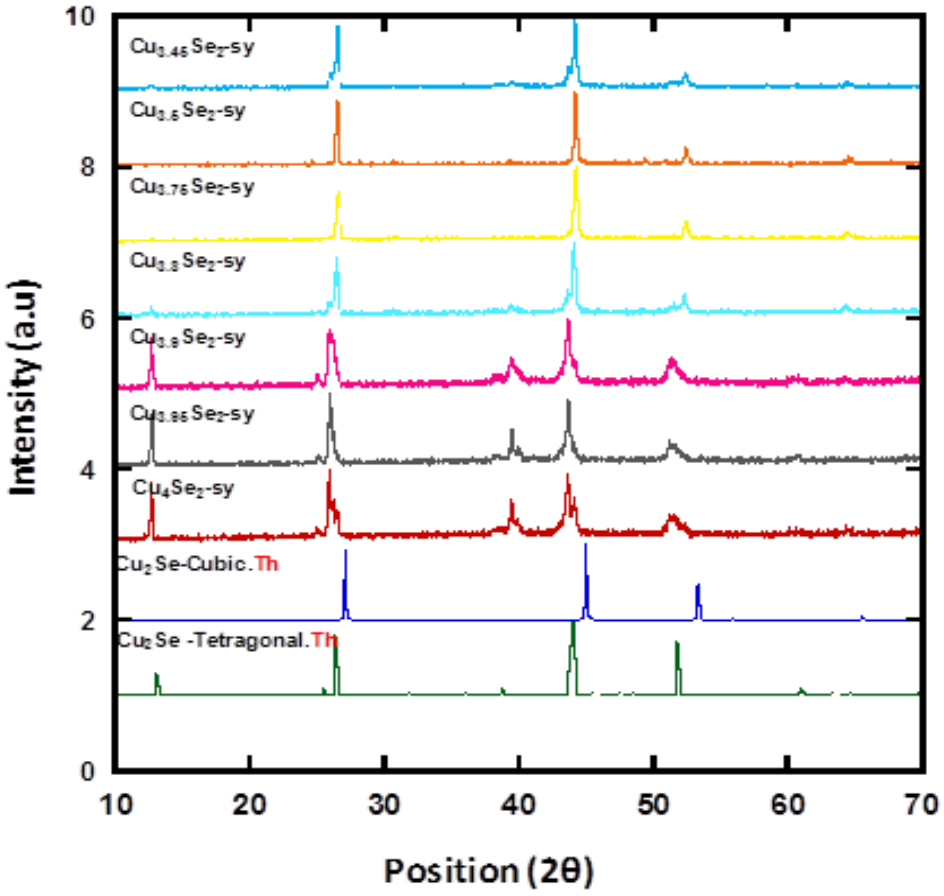

Figure 6. 2 : X-ray powder diffraction patterns of the synthesized $Cu_{1+x}Se_2$ (x = 0, 2.45, 2.5, 2.75, 2.80, 2.90, 3.0) via high temperature solid state reveals the presence of both high temperature cubic phase (β) and low temperature tetragonal phase(α).

Studies on phase composition and transformation

Figure 6.2 shows the powder XRD patterns for the all $Cu_{1+x}Se_2$ (x = 2.45, 2.5, 2.75, 2.80, 2.90, 2.95, 3.0) samples synthesized by high temperature liquid state mediated solid state reactions. Depending on the concentration of Cu (x value) the XRD patterns show either peaks of the high temperature cubic structure of Cu_2Se (Cu_4Se_2) or a mixture of peaks belonging to both the high temperature cubic and the low temperature tetragonal polymorphs of Cu_2Se. According to Fig

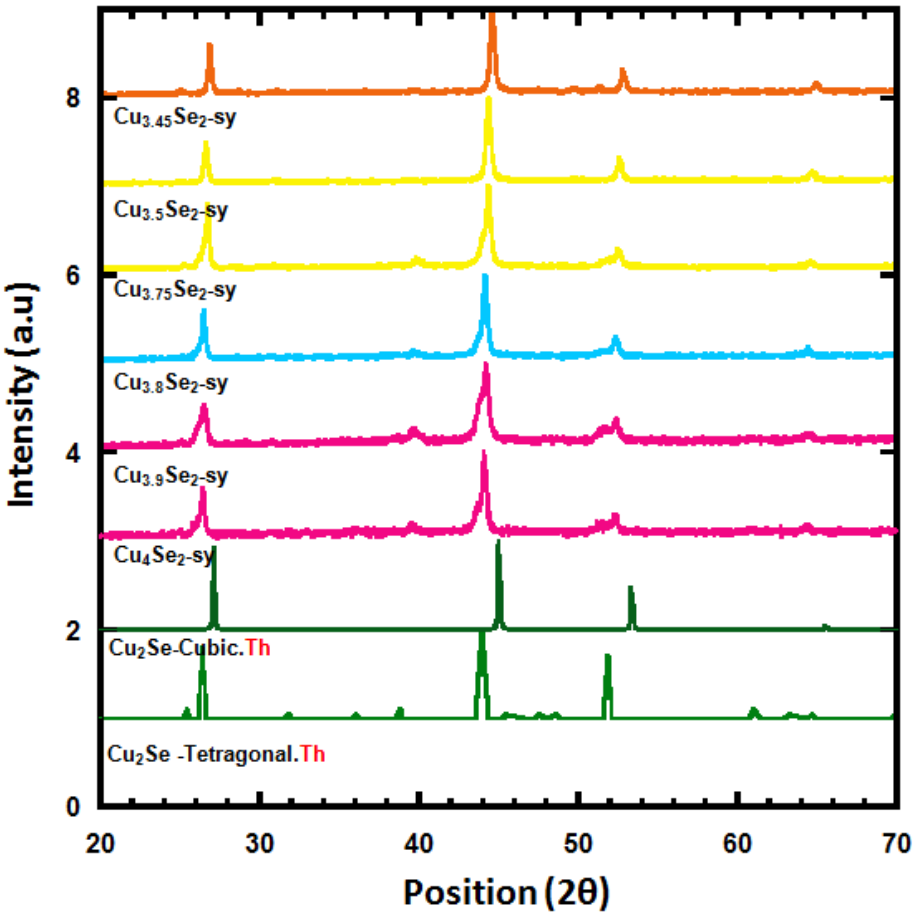

Figure 6.3 : X-ray powder diffraction patterns of the elemental ball milled $Cu_{1+x}Se_2$ (x = 2.45, 2.5, 2.75, 2.80, 2.90, 2.95 and 3.0) samples revealing the presence of both high temperature cubic phase (β) and low temperature tetragonal phase (α).

6.2, we can observe that the initial compositions $Cu_{3.45}Se_2$, $Cu_{3.5}Se_2$ and $Cu_{3.75}Se_2$ only showed the peaks for stable cubic phase, but as the composition neared to $Cu_{3.8}Se_2$, the XRD patterns revealed the presence of a mixture of tetragonal phase (α) and cubic phase (β) for the rest of the samples [64,210].

Figure 6. 3 shows the powder XRD pattern for the all $Cu_{1+x}Se_2$ (x = 2.45, 2.5, 2.75, 2.80, 2.90, 3.0) samples synthesized by elemental ball milling reactions. Similar observations were found in comparisons to Fig 6.2 where compositions like $Cu_{3.45}Se_2$ and $Cu_{3.5}Se_2$ were pure cubic (β phase), whereas the rest of the samples showed a mixture of α and β phases. Figure 6.4 presents the X-ray diffraction (XRD) patterns taken for the $Cu_{1+x}Se_2$ (x = 0,2.45, 2.5, 2.75, 2.80, 2.90, 3.0) compounds at room temperature synthesized via compositional ball milling. Because the samples were synthesized from the transformation of $CuSe_2$ as precursor, XRD pattern has been recorded for the starting material $CuSe_2$ in order to measure the progress of transformation reaction. The $CuSe_2$ has a cubic and an orthorhombic structure and both phases seems to be stable at room temperature after mechanical alloying. Then, the XRD patterns of the rest of the compositions show the cubic (β) phase for the compositions $Cu_{3.45}Se_2$, $Cu_{3.5}Se_2$ and $Cu_{3.75}Se_2$ after, which gradually the tetragonal (σ) phase started to appear. For all the three synthesis methods, it has been observed that as the stoichiometry of the sample differs from the composition Cu_4Se_2 (Cu_2Se), the high angle peaks gradually shift to higher angle, which indicates that the absence of sufficient Cu leads to decrease the lattice parameter of β-Cu_2Se.

To support the XRD data, the samples were further subjected to a heating cycle from room temperature to 800 ^oC to understand its phase transition behavior. As per the previously reported phase diagram[211], Fig 6.5 (A), Cu-Se system has several phase stabilities. The most stable phase of this system is Cu_2Se, which is cubic at high temperature. The exact composition shows a low

temperature transition of tetragonal/monoclinic phase around 120-140^{o}C. This phase transition is mostly reversible as reported earlier[212]. From the DSC curves shown in Fig. 6.5(B)-(E), the$Cu_{1+x}Se_2$ samples does not show any thermal event at low temperature. But when the composition approaches the Cu_2Se stoichiometry ($Cu_{3.9}Se_2$ and Cu_4Se_2), a peak at low temperature around 131^{o}C (as indicated) is observed, which reconfirms the presence of a low temperature α phase in the sample. This phase transition temperature has already been predicted in the reported phase diagram Fig.6.5 (A).

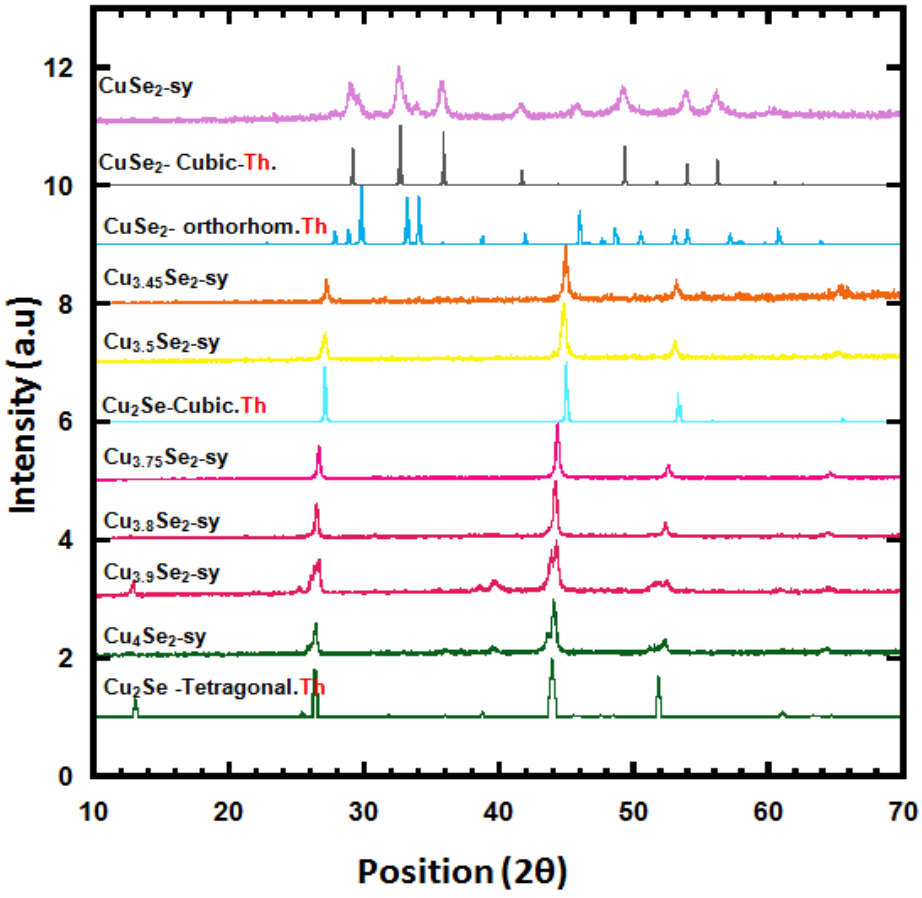

Figure 6.4 : X-ray powder diffraction patterns of the synthesized (x = 2.45, 2.5, 2.75, 2.80, 2.90, 3.0) via compositional ball milling. $Cu_{1+x}Se_2$ reveals the presence of both high temperature cubic phase (β) and low temperature tetragonal phase(α).

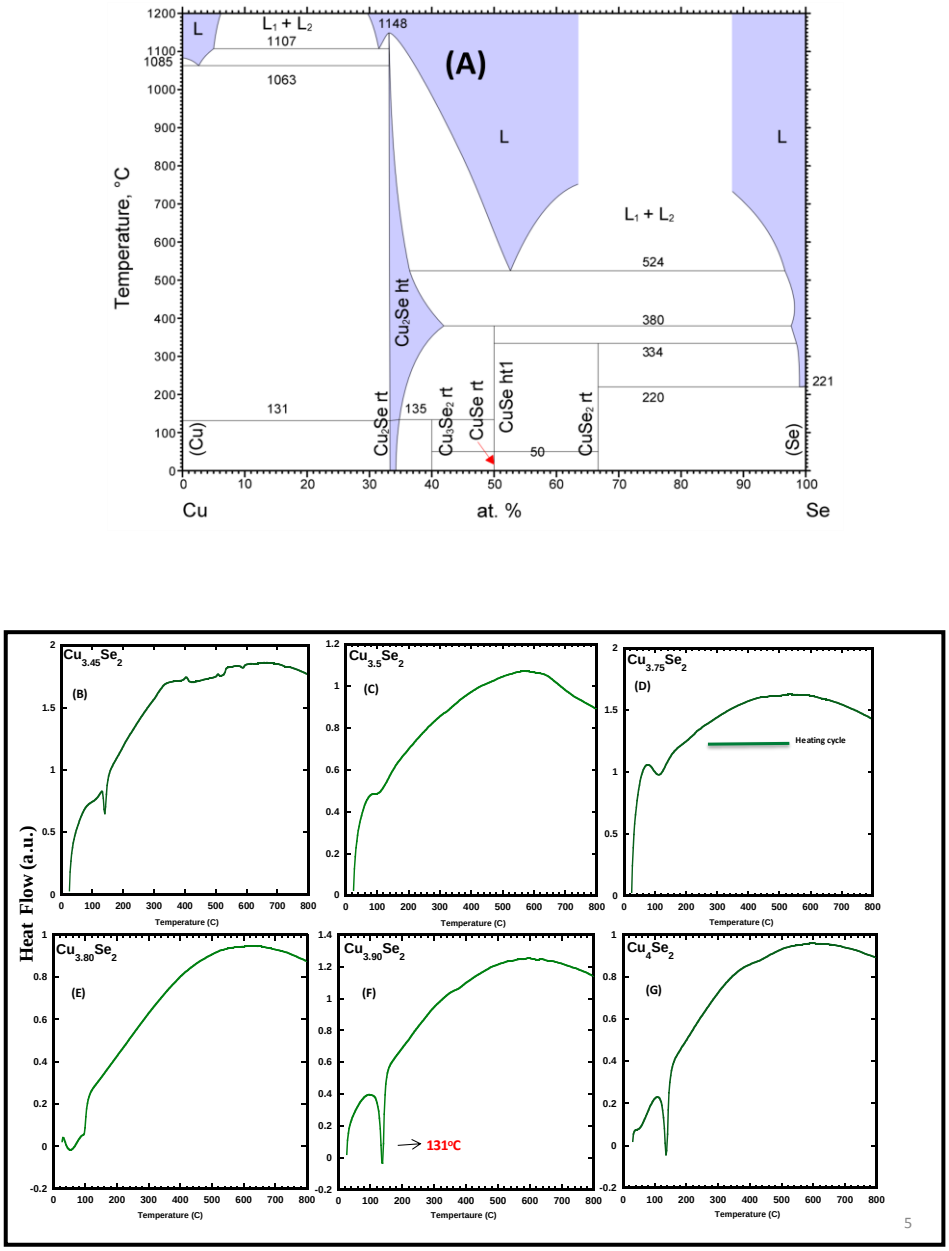

Figure 6.5 : (A) Phase diagram for Cu-Se system showing stability of various phases with respect to temperature; (B)-(G) DSC curves for $Cu_{1+x}Se_2$ (x = 2.75, 2.80, 2.90, 2.95 and 3.0) synthesized via high temperature solid state method. Thermal event for sample $Cu_{3.9}Se_2$ (F) and Cu_4Se_2 (G) shows the presence of the low temperature α phase.

Similar, DSC curves shown for selected samples of $Cu_{1+x}Se_2$ (x = 2.45, 2.5, 2.75, 3.0) in Fig 6.6 revealed no phase transitions for the samples x = 2.45, 2.5, 2.75, but a strong transition at 122^{o}C for the sample with excess Cu content of x = 3 Fig 6.6(D).

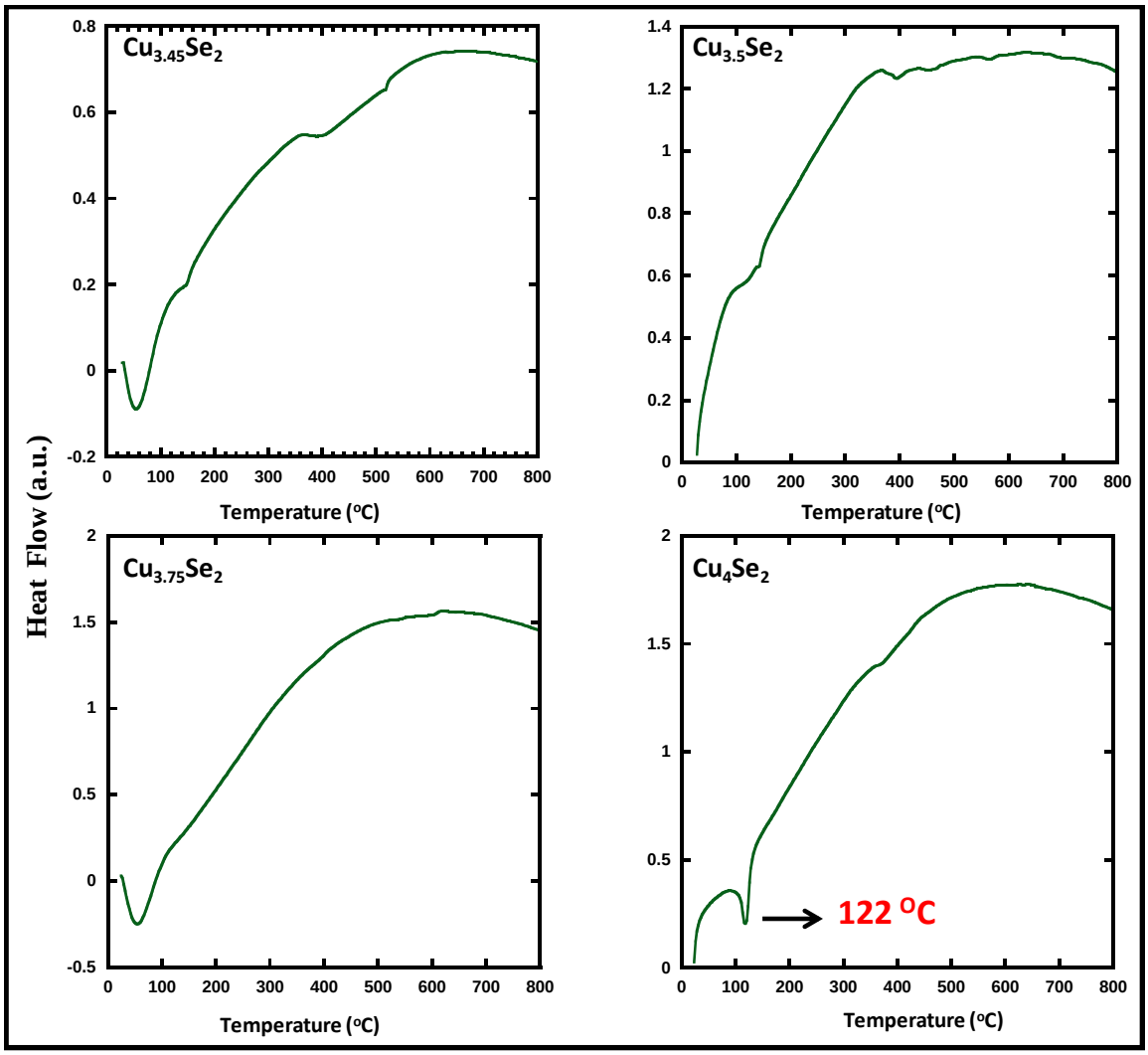

Figure 6.6 : (A-D): DSC curves for selected compositions of $Cu_{1+x}Se_2$ (x = 2.45, 2.5, 2.75, 3.0) synthesized via elemental ball milling. Thermal event for sample Cu_4Se_2 (D) shows the presence of the low temperature α phase below 122^{o}C.

In order to check the phase transitions of the $Cu_{1+x}Se_2$ (x = 0, 2.45, 2.5, 2.75, 2.80, 2.90, 3.0), DSC measurements have been done on few of the samples like $CuSe_2$, ,$Cu_{3.45}Se_2$,$Cu_{3.75}Se_2$ and Cu_4Se_2 (Figure 6.7). The thermal events observed through DSC are in good agreement with those of XRD and the standard phase diagram Fig. 6. 7(A). The DSC curves for $CuSe_2$ (Fig 6.7A) shows multiple transition phases at 334°C , 380°C and 528°C respectively. After the addition of Cu the products formed like $Cu_{3.45}Se_2$ (Fig 6.7B) ,$Cu_{3.75}Se_2$ (Fig 6.7C) did not show any thermal event, whereas the sample Cu_4Se_2 (Fig 6.7D) showed a transition at 122°C which is exactly the same as observed previously in samples synthesized by elemental ball milling method.

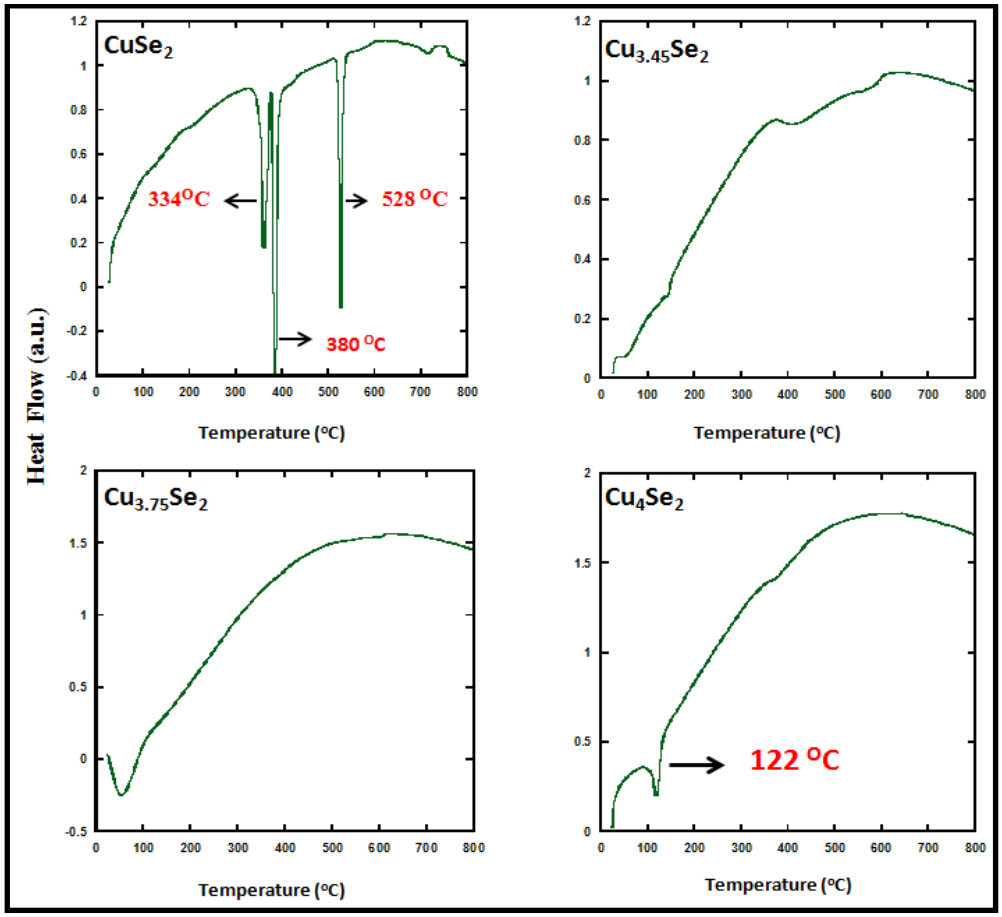

Figure 6. 7 : (A-D): DSC curves for selected compositions of $Cu_{1+x}Se_2$ (x = 0, 2.45, 2.75, 3.0) synthesized via compositional ball milling. Thermal event for sample Cu_4Se_2 (D) shows the presence of low temperature α phase at 122°C

Studies on thermoelectric properties

Thermoelectric properties of $Cu_{1+x}Se_2$ (x = 2.45, 2.5, 2.75, 2.80, 2.90, 2.95, 3.0) synthesized via high temperature solid- state reaction

Temperature dependence of the thermal conductivities of selected compositions of $Cu_{1+x}Se_2$ (x = 2.75, 2.80, 2.90, 2.95 and 3.0) are shown in Figure 6. 8(A)-(B).The total thermal conductivity for the samples decreases gradually with increasing temperature and increasing Cu content. As all samples are fairly a mixture of α and β phases below 400 K, anomaly in the behavior has been observed due to α – β transition and it is also consistent with the lattice thermal conductivity shown in Fig. 6.8(B).The total thermal conductivity is expressed as the sum of the electronic component (κ_e) and the lattice component (κ_L). κ_e can be calculated by the Wiedemann-Franz relationship, $\kappa_e = L\sigma T$, where L = Lorentz Number (2×10^{-8} $V^2.K^{-2}$), σ is the electrical conductivity and T is the absolute temperature. The lattice thermal conductivity can be calculated by the relationship, $\kappa_{total} = \kappa_L + \kappa_e$ .With increasing Cu content, we are introducing more disorder to the $Cu_{1+x}Se_2$ lattice, which can cause strong scattering of short-wavelength phonons by short range disorders resulting in the decrease in the lattice thermal conductivities. As discussed earlier, at lower temperatures the $Cu_{1+x}Se_2$ compositions adopt the α- phase structure, in which all Cu and Se atoms are well ordered leading to lower symmetry crystal structure [213]. With the increase in temperatures, the entire structure becomes superionic and kinetically disordered throughout the structure[214].This high degree of disorder eventually enhances the phonon scattering and reduces the lattice thermal conductivity. Fig. 6. 8 (C) shows the temperature dependence of the electrical conductivities of $Cu_{1+x}Se_2$ (x = 2.75, 2.80, 2.90, 2.95 and 3.0).The electrical conductivities seems to increase gradually untill the temperature range of 350 - 400 K

is reached and then it shows a fast decrease with further increase in temperature up to 600K. The relationship between electrical conductivity and mobility can be termed as

$$\sigma = \mu\ n\ e\ ;$$

where σ = electrical conductivity; μ = electron mobility and e = charge on an electron. At low temperature, the least disordered α phase is more stable. Upon increasing the temperature, the promotion of electrons from the valence band (VB) to the conduction band (CB) results in an increase in the carrier concentration, which explain very well the observed increase in the electrical conductivity with increasing temperatures. However, after the transition temperature, the new β phase is comparatively more disordered and the electronic band structure presumablY changes from semiconducting to a heavily doped semiconducting behavior.Therefore, the observed gradual decrease in the electrical conductivity with increasing temperature likely originates from a drastic decrease in the mobility due to enhance carrier scattering by the disordered Cu atoms in the lattice. We can also observe that with the increase in Cu concentration, there is a decrease in electrical conductivity. This is presumably due to the formation, upon varying the concentration of Cu in $Cu_{1+x}Se_2$, of composite materials containing various fractions of Cu_xSe_y phases such as Cu_2Se and $CuSe_2$. As the Cu content increases, the composition of the resulting materials gradually evolves from the predominantly metallic copper-poor composition, $CuSe_2$, to the predominantly semiconducting Cu-rich phase, Cu_2Se. This mixing of various fractions of metallic and semiconducting phases can lead to the observed gradual decrease in the electrical conductivity as the fraction of the semiconducting phase increases. A similar trend was also observed on the electrical conductivity of $Cu_{1+x}Se_2$, samples prepared via elemental ball milling (Figure 6. 9) and compositional ball milling ($CuSe_2$ + xCu) (Figure 6.10).

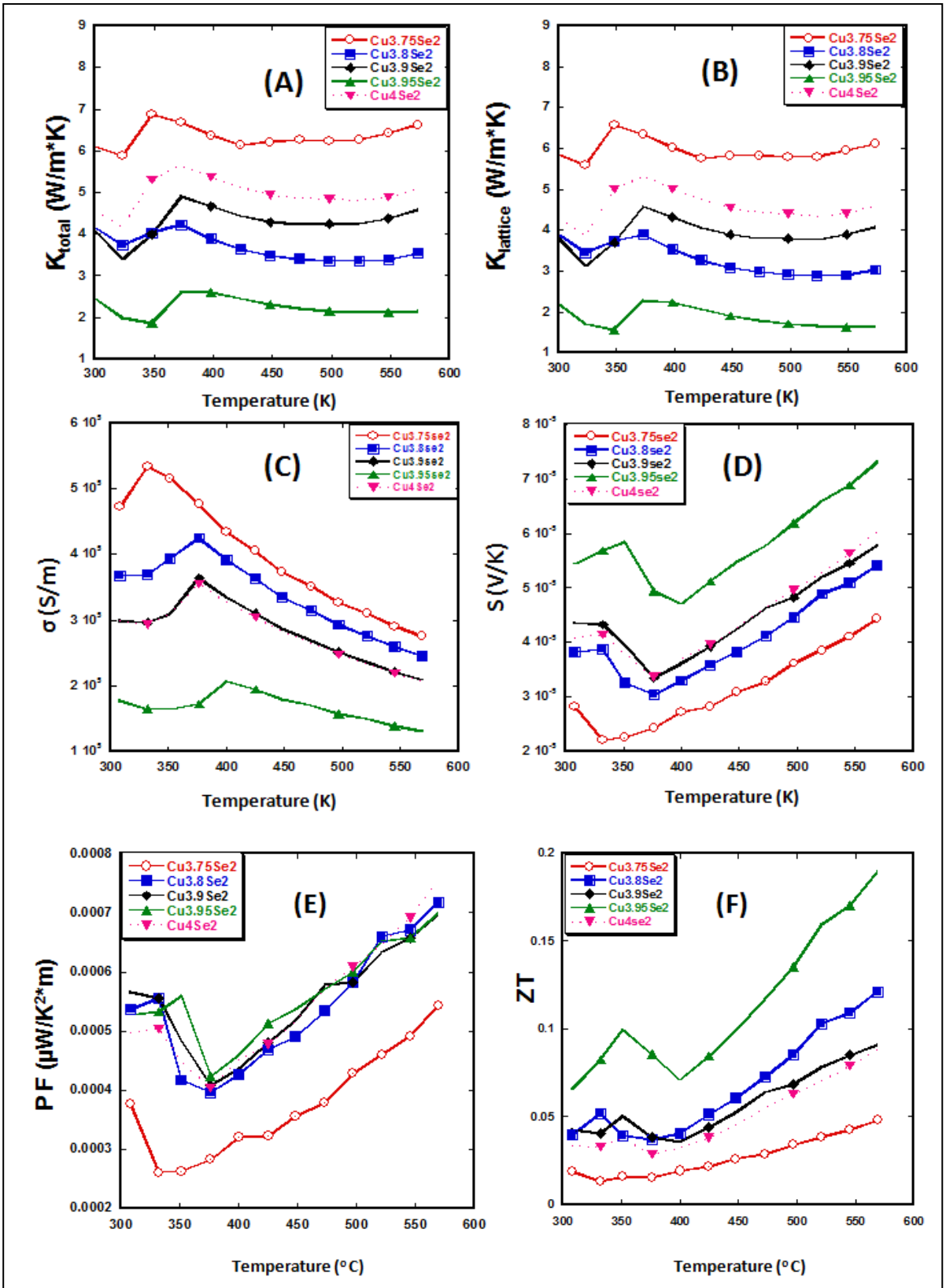

Figure 6.8 : Temperature dependence of the thermal and electronic properties of $Cu_{1+x}Se_2$ (x = 2.75, 2.80, 2.90, 2.95 and 3.0) synthesized by solid state reaction. (A) total thermal conductivity; (B) Lattice thermal conductivity; (C) Electrical conductivity; (D) Seebeck; (E) Power Factor; (F) Figure of merit (ZT).

Fig. 6.8 (D) depicts the temperature dependence of the Seebeck coefficient of the $Cu_{1+x}Se_2$ compositions. The positive Seebeck coefficient indicates that the $Cu_{1+x}Se_2$ (x = 2.75, 2.80, 2.90, 2.95 and 3.0) shows p-type conduction (holes are the majority charge carriers). Seebeck value seems to increase with the increase in Cu content at a given temperature. This is consistent with the above described decrease in the electrical conductivity with increasing Cu content. As per the earlier explanation, addition of more Cu induces the formation of more semiconducting Cu_2Se phase and less of the semimetallic $CuSe_2$ phase resulting in a decrease in the carrier density at a given temperature. Since the Seebeck coefficient is inversely proportional to the carrier concentration, it increases with the decrease in carrier concentration. After the transition temperature of the Cu_2Se phase from the semiconducting α-phase to the metallic β-phase, the Seebeck coefficient increase linearly with increasing temperature, which is consistent with the metallic behavior of the samples. A similar behavior of the Seebeck coefficient was also observed on $Cu_{1+x}Se_2$ composition prepared by elemental and compositional ball milling (Fig 6.9 and 6.10). Fig. 6.8(E) shows the temperature dependence of the power factor of the $Cu_{1+x}Se_2$ compositions. Due to the low Seebeck coefficient, the Cu-poor compositions show lower power factor. The power factor slightly increases with increase in the Cu content and remain almost constant at high temperature for the rest of the samples. The composition $Cu_{3.9}Se_2$ shows almost a 31 % increase in the power factor compared to the composition $Cu_{3.75}Se_2$. Combining all the results, the dimensionless thermoelectric figure of merit has been calculated using the formula $ZT = \alpha^2\sigma T/\kappa$ (Fig. 6.8 F).The ZT increases with increasing Cu content. The Cu-poor sample $Cu_{3.75}Se_2$ shows ZT around 0.05 at 575K, while the sample $Cu_{3.95}Se_2$ shows the highest ZT around 0.18 at 575K (260% enhancement). Although a remarkable enhancement in the thermoelectric properties has been achieved by tuning the Cu content in $Cu_{1+x}Se_2$ compositions

the ZT values obtained are drastically lower compared to the previous work by Liu[215] and Yu[1]. To achieve further improvement, efforts were made by altering the synthetic procedure. For example, similar compositions were synthesized by mechanical alloying of the elements and by mechanical alloying of a mixture of $CuSe_2$ and additional Cu. The thermoelectric properties of these samples are presented below in comparison to the data discussed above.

Thermoelectric properties of Cu_{1+x} Se_2 (x = 2.45, 2.5, 2.75, 2.80, 2.90, 3.0) synthesized via elemental ball milling

Figure 6.9 (A) reflects the temperature dependence of the thermal conductivity of selected $Cu_{1+x}Se_2$ (x = 2.75, 2.80, 2.90,3.0) samples, whereas Fig. 6.9(B) shows the temperature dependence of the lattice thermal conductivity. All the samples show a similar transition described above for $Cu_{1+x}Se_2$ samples prepared by solid -state reaction of the elements. Interestingly, we observe a reduction of the thermal conductivities compared to the high temperature liquid state mediated solid state method. In the high temperature liquid state mediated solid state method, we found that the thermal conductivity for the sample $Cu_{3.75}Se_2$ was about 7 W/m*K at 575 K, whereas for the elemental ball milling process, the thermal conductivity could be decreased to 2.5 W/m*K at 575K,which is about 64% of reduction. This minimization might corresponds to the nanostructuring of the $Cu_{3.75}Se_2$ sample by the mechanical alloying process. As discussed in **chapter-5**, the ball milling process can enhance the ease of completion of the reaction as well as the formation of nanostructures. Due to the decrease in the dimension of the powder grain size, the phonon scattering is enhanced, which results in reduction of the thermal conductivity. Temperature dependence of the electrical conductivity is shown in Figure 6. 9(C), where we can observe the similar transition. However the conductivity values have been substantially decreased compared to the liquid state mediated solid state

method (Fig.6.8 C). The composition $Cu_{3.75}Se_2$ has electrical conductivity values of about 3000 S/m whereas the same composition made via ball milling showed conductivity value less than 2000 S/m at 575K. As the Seebeck Fig 6.9(D) for the $Cu_{3.75}Se_2$ made by ball milling has almost similar value of 48μV/K at 775 K, it suggests that the carrier mobility might have decreased largely in the case of ball milled samples due to larger point defects caused by nanostructures. The carrier concentrations might not have changed largely. So the decrease in the mobility of the ball milled sample decreased the overall electrical conductivity of the sample to that of the solid state samples. Hall Effect measurements would be the best method to provide a strong evidence for our speculations. Based on the electrical conductivity and Seebeck coefficient and the power factor of all the samples have been calculated and plotted as Figure 6.8 (E), where sample $Cu_{3.75}Se_2$ showed the lowest value due to smallest Seebeck whereas, the $Cu_4 Se_2$ sample exhibit the highest power factor due to the highest Seebeck coefficient. Another factor affecting the power factor is the electrical conductivity, which seems to be comparable for both of these samples. The power factor of the samples synthesized via ball milling is almost similar to that of the samples made by liquid state mediated solid state method. As a result of the similar power factors and reduced thermal conductivity, the ZT of the sample $Cu_{3.75}Se_2$ was increased to ~ 0.15, which is only slightly lower than the value obtained for the sample prepared by liquid state mediated solid state reaction, where the highest ZT found was 0.18 at 575K. Although the ball milling method reduced the thermal conductivity effectively, the larger reduction in electrical conductivity almost nullifies its effect and no improvement has been observed in the figure of merit values. To further optimize the synthesis process, efforts were made to slightly change the starting reactants keeping the ball milling conditions identical. The thermoelectric behavior of

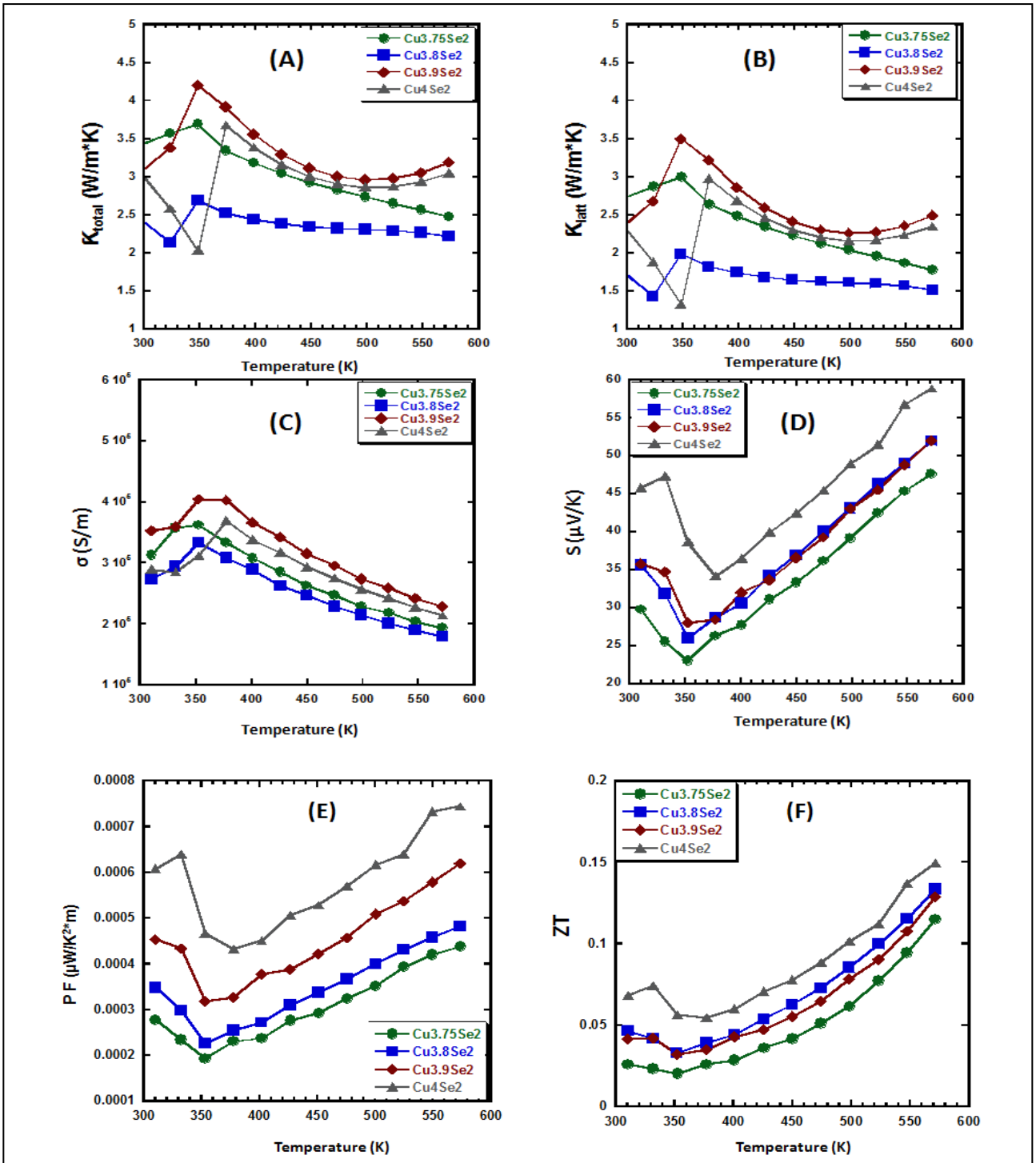

Figure 6.9 : Temperature dependence of the thermal and electronic properties of $Cu_{1+x}Se_2$ (x = 2.75, 2.80, 2.90, 3.0) synthesized via ball milling of the elements. (A) total thermal conductivity; (B) Lattice thermal conductivity; (C) Electrical conductivity; (D) Seebeck. (E) Power factor; (F) Figure of merit (ZT)

the new samples obtained by mechanical alloying of a mixture of $CuSe_2$ and additional Cu is discussed below.

Thermoelectric properties of Cu_{1+x} Se_2 (x = 2.45, 2.5, 2.75, 2.80, 2.90, 3.0) synthesized via compositional ball milling

Figure 6.10 (A) reflects the temperature dependence of thermal conductivity of samples $Cu_{1+x}Se_2$ (x = 2.5, 2.75, 2.80, 2.90, 3.0) and Fig. 6.10(B) shows the temperature dependence of the lattice thermal conductivity. All the samples show a similar transition as discussed for the liquid state mediated solid state and elemental ball milled samples and we can observe almost similar values of the thermal conductivities compared to that of the elemental ball milling samples. Fig 6.10 (C) shows the electrical conductivity, which also has the similar value to that of elemental ball milling, but interestingly we could see a trend in the electrical conductivity values. It seems to decrease with the increase in Cu content. The Seebeck in Fig 6.10 (D) also seems to follow a trend where it increases with the increase in the Cu content, which suggest that the carrier concentration might be varying here too. This change in the Seebeck coefficient was not observed in the elemental ball milling procedure. The Seebeck showed up to 33% enhancement when moving from $Cu_{3.5}Se_2$ to Cu_4Se_2.Due to high Seebeck, the sample Cu_4Se_2 showed the highest power factor in spite having low electrical conductivity. Because all the samples showed comparable electrical conductivities and Seebeck, the power factor also seems to be fairly similar for all the composition Fig 6.10(E). Finally, the figure merit (ZT) of the sample with maximum Cu content Cu_4Se_2 is the highest (ZT of about 0.14 at 575K) although the magnitude is still lower than the reported one and the previously discussed liquid state mediated solid state and elemental ball milling. This is ~55% enhancement compared to the $Cu_{3.5}Se_2$, which has ZT around ~ 0.09.Figure 6. 10(F).

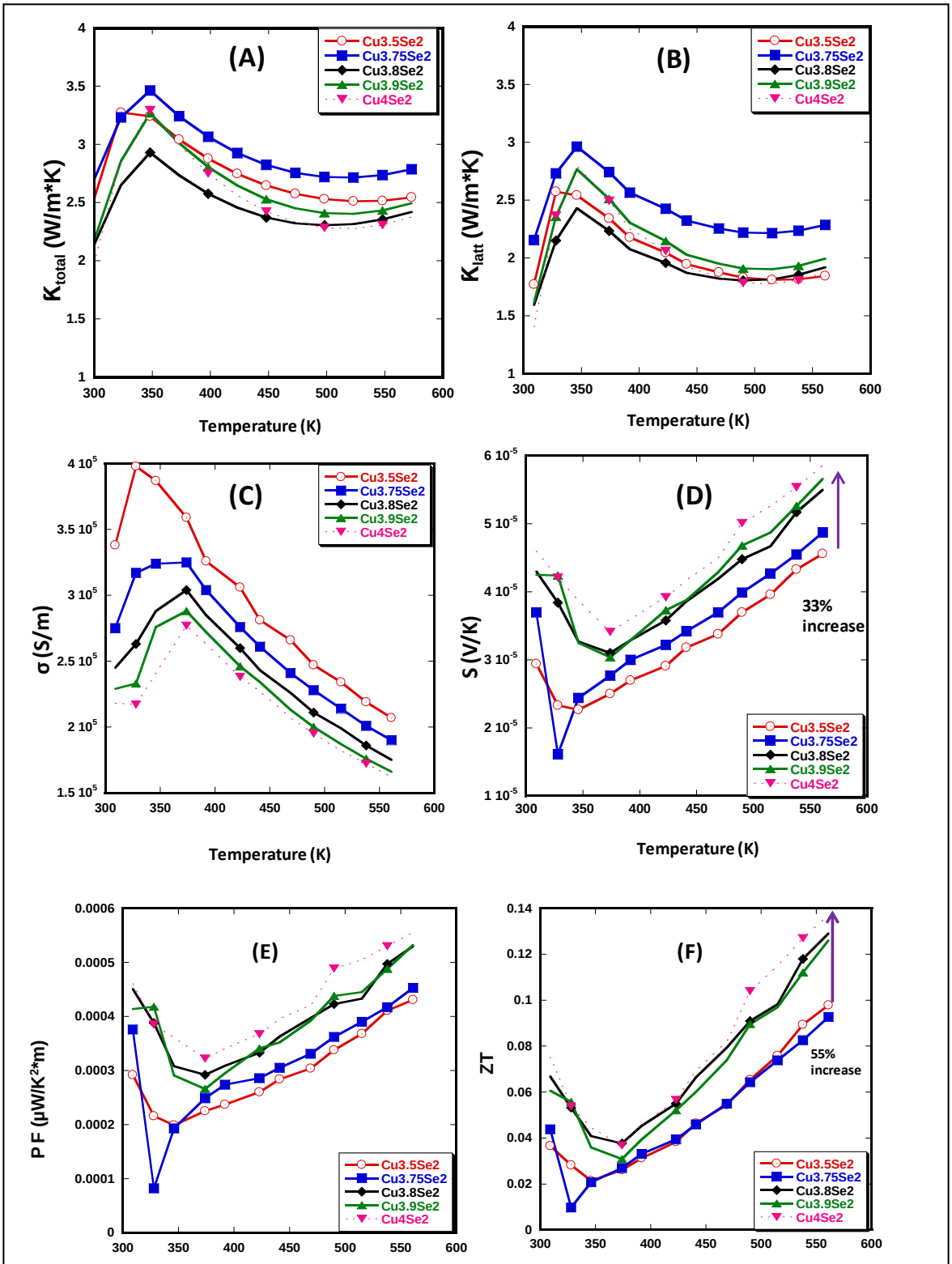

Figure 6.10 : Temperature dependence of the thermal and electronic properties of $Cu_{1+x}Se_2$ (x = 2.5, 2.75, 2.80, 2.90, 3.0) synthesized by ball milling $CuSe_2$ and elemental Cu. (A) total thermal conductivity; (B) Lattice thermal conductivity; (C) Electrical conductivity; (D) Seebeck; (E) Power factor; (F) Figure of merit (ZT).

Despite our multiple attempts to synthesize the $Cu_{1+x}Se_2$ phases, improvement in the figure of merit could not be achieved. However, we demonstrated from the study, that it is possible to control different synthesis factors to produce materials with similar thermal and electronic properties. Since, the best ZT value of 1.5 at 1000K reported for the Cu_2Se could not be achieved; we have decided to focus our attention first on the development of simple method for the fabrication of Cu_2Se. .

6.3 Synthesis of copper selenide (Cu_2Se) system via different methods

6.3.1: Synthesis

In the current attempt, Cu_4Se_2 powder samples have been prepared by using high energy shaker ball mill contrary to the planetary ball mill, which was used for previous ball milling studies. Calculated stoichiometric amount of elemental Cu and Se were used to produce three batches of samples. In the synthesis, Cu powder (Alfa Aesar, 99.5%) and Selenium powder (Strem chemicals, 99.9%) elements with different compositions were weighed stiochiometrically and ground well under inert atmosphere. In the first step, 10 grams of $CuSe_2$ samples were prepared by shaker mill for 10 hrs by milling the elemental Cu and Se. In the next step, calculated amounts of Cu were added to the synthesized $CuSe_2$ powder to produce Cu_4Se_2 (or Cu_2Se) via shaker ball mill for 6 hours. After the completion of the reaction, part of the sample was recovered and hot pressed in the form of pellets for further characterization (1^{st} Batch). Rest part of the sample was annealed for two days at 700^oC and hot pressed (2^{nd} Batch). The 3^{rd} batch of the sample was made by ball milling the elemental Cu and Se for 6 hours followed by two days of annealing at 700^oC. All the samples were ball milled using high energy ball milling (SPEX

8000M Mixer). For consolidation, samples were hot pressed by ramping up to 600 ^{o}C in two hours, held there for 3 hour and ramped down in two hours under vacuum.

6.3.2: Characterizations

The Cu_4Se_2 prepared by various synthetic routes were characterized by the methods as described earlier. Additionally the XRD patterns were also taken at higher temperatures (200^{o}C) to track the phase transitions of the samples. The microstructure of the annealed and ball milled samples were determined by using high-resolution transmission electron microscopy (HRTEM JEM3100F). The high temperature stage was used to determine the electron diffraction patterns of the sample at room temperature and at 200^{o}C to ensure the phase transition.

6.3.3: Results and discussions

Figure 6.11 represents the X-ray diffraction (XRD) patterns taken at room temperature for the Cu_4Se_2 compounds synthesized via elemental and compositional ball milling. To track down the phase transformation, which occurs around 120-140 ^{o}C, XRD patterns were taken both at room temperature and high temperature (200^{o}C). In previous results as described earlier in this chapter, most of the samples contain a mixture of cubic and tetragonal phases. However, here the samples seem to have a mixture of cubic and monoclinic phases at room temperature. To guide the eyes, the cubic theoretical pattern has been included in the XRD comparison plot. Apart from the peaks due to the cubic phase, all other peaks belong to the monoclinic phase of Cu_4Se_2. All samples show only cubic phases at higher temperatures irrespective of the method of synthesis.

The high magnification transmission electron microscopy image has been taken for a portion of the sample (compositional ball milled and annealed) which showed excellent crystallinity (Fig 6.12(A)). The electron diffraction pattern has been recorded for the same sample both at room

temperature and high temperature (200^{o}C).The room temperature SAED pattern (Fig.6.12(B)) showed a monoclinic diffraction pattern, whereas the high temperature SAED pattern clearly showed the cubic electron diffraction pattern(Fig.6.12(B)). This further supports the PXRD results, which showed the presence of different phases.

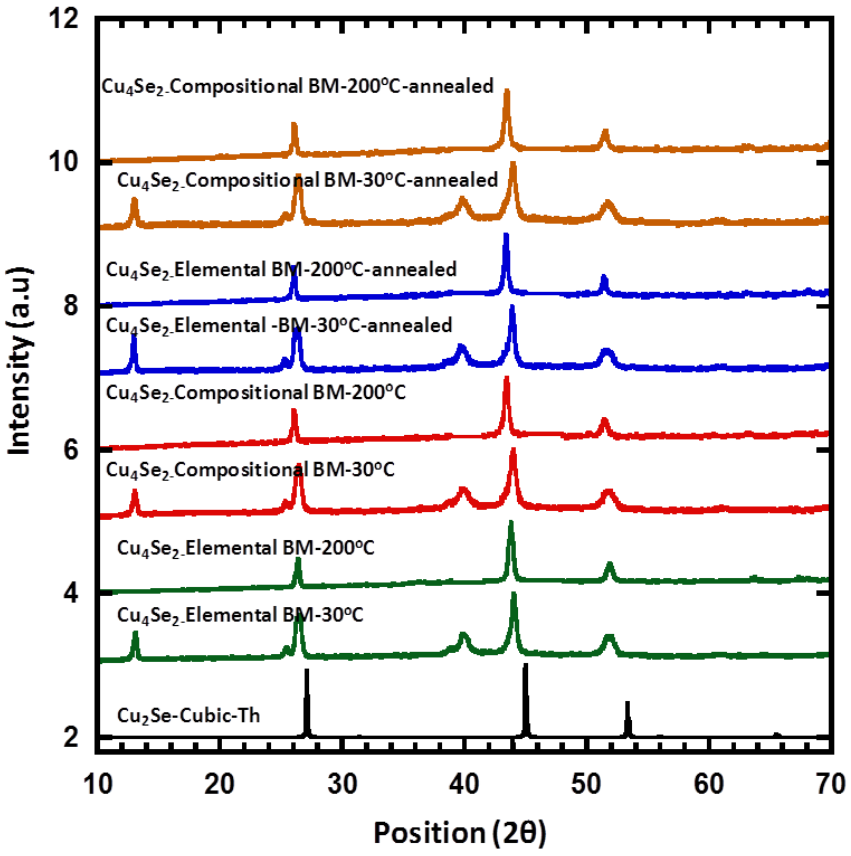

Figure 6.9 : X-ray powder diffraction patterns of as-synthesized Cu_4Se_2 via elemental and compositional ball milling taken at 200 °C and at room temperature to probe the phase transition. All the samples showed a mixture of cubic (β) and tetragonal peaks (α) at room temperature, whereas only cubic peaks are observed at high temperatures (200^{o}C).

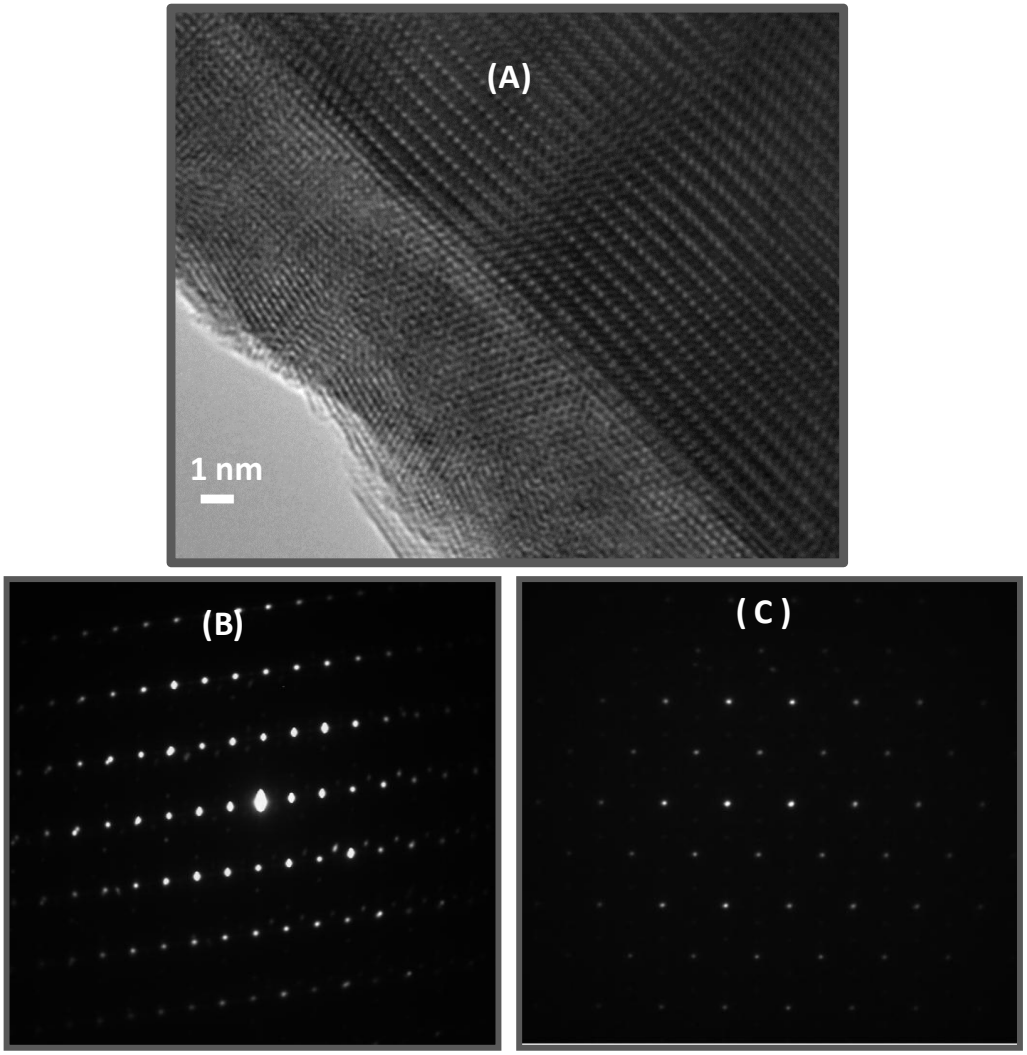

Figure 6.10 : (A) HRTEM image of annealed and hot pressed Cu_4Se_2 synthesized via compositional ball milling showing its excellent crystallinity. (B) SAED pattern for the same sample at room temperature showing its monoclinic behavior and (C) SAED pattern at high temperature (200^oC) showing the transition to the cubic phase**.**

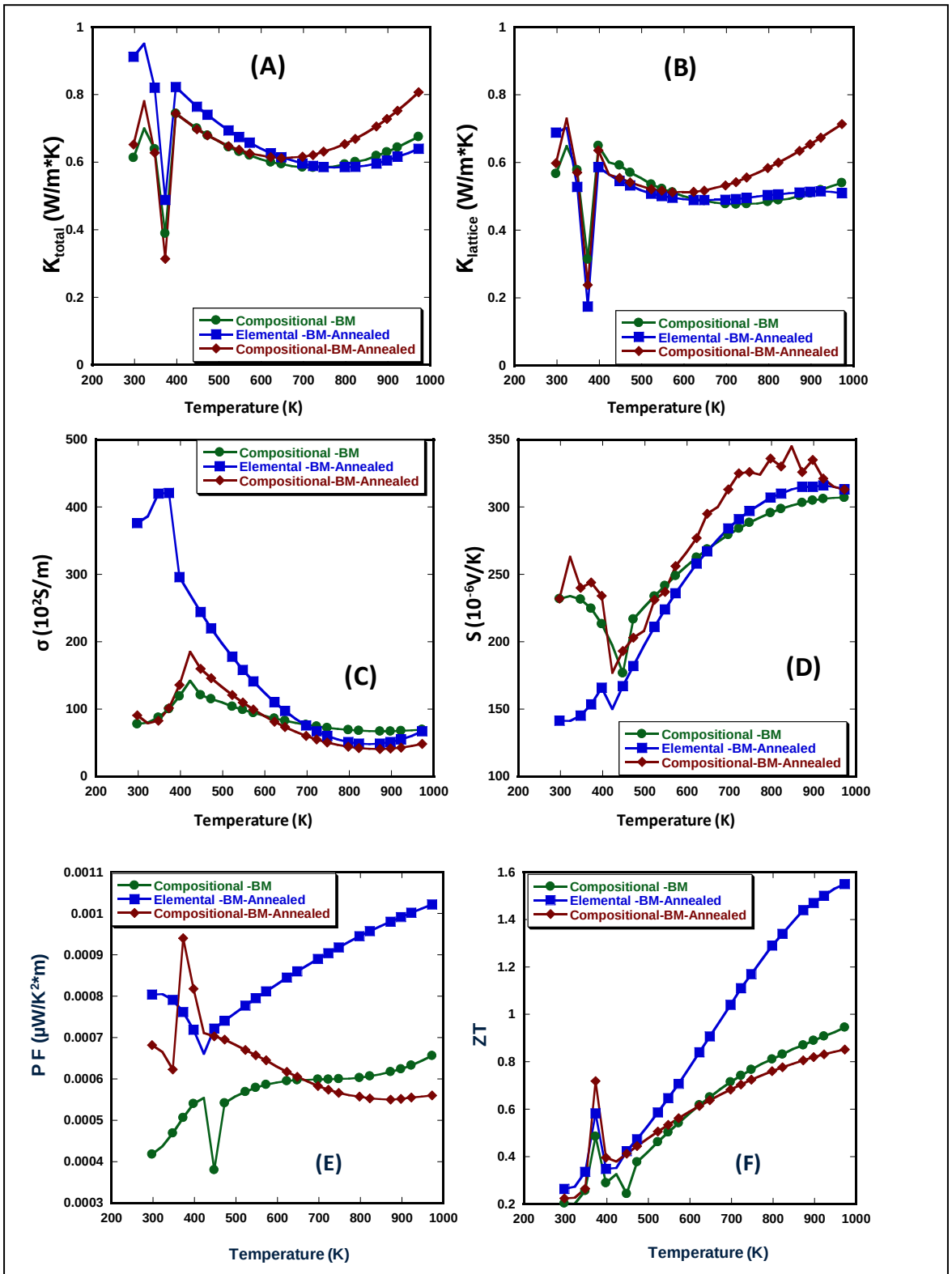

Figure 6.13 : Temperature dependence of the thermal and electronic properties of Cu4Se2 (A) total thermal conductivity; (B) Lattice thermal conductivity; (C) Electrical conductivity; (D) Seebeck. (E) Power factor; (F) Figure of merit (ZT).

Figure 6.13 (A) depicts the temperature dependence of thermal conductivities of Cu_4Se_2 prepared by compositional ball milling, the annealed elemental ball milled and the annealed compositional ball milled samples. All samples show similar phase transitions as explained earlier. Interestingly, all of these samples showed a large reduction in their thermal conductivities compared to the $Cu_{1+x}Se_2$ samples discussed in the previous sections. For example, at 700 K the Cu_4Se_2 made by liquid state mediated solid state technique showed a thermal conductivity of 5 w/mK, whereas in elemental ball milling with planetary ball mill it decreased down to 3 w/mK. For compositional planetary ball mill, the thermal conductivity was around 2.3 w/mK. However, the sample which is ball milled via a shaker ball mill show the thermal conductivity as low as 0.8w/mK. Similar trend has been also observed for lattice thermal conductivities in Fig 6.13 (B). The nanostructuring as well as the geometric defects are more prominent in shaker ball mill compared to the planetary ball mill due to the higher energy provided by the former technique. This could be a larger contributor for the reduction in the thermal conductivities.

Fig 6.13 (C) represents the electrical conductivities of all the samples, which also shows almost 10 times enhancement from the previous attempts. All of the sample show similar phase transitions as explained earlier. Among the current series of samples the annealed elemental ball milled sample showed very high electrical conductivity compared to the compositional ones. We speculate that the elemental ball milling might be producing more ordered structure compared to the compositional one where filling of Cu atoms into the vacancy is more random. Therefore, small randomness in elemental ball milling samples might be contributing towards fewer defects, which is associated with high mobility of the charge carriers. Due to marginal decrease in mobility, the electrical conductivity of elemental ball milled sample was higher compared to the

compositional ball milled sample. The Seebeck coefficient remains almost comparable for all the samples, which suggest comparable amount of charge carriers. However, the Seebeck coefficient is substantially higher than values obtained for the $Cu_{1+x}Se_2$ samples discussed above. Using the above results of electrical conductivities, the Seebeck coefficient, the thermal conductivity the dimensionless thermoelectric figure of merit can be calculated using the formula $ZT = \alpha 2\sigma T/\kappa$, as shown in Fig. 6.13 (F). It can be seen that the ZT value of all samples increases with increasing temperature with the annealed elemental ball milled sample showing the highest ZT of around 1.58 at 1000K, which is comparable to the reported results[1]. The highest ZT obtained for this sample is due to its largest power factor (Fig.6.13 (F)), which was mostly contributed by the largest electrical conductivity. At high temperatures, nearly 163% improvement of the power factor over the annealed compositional ball milled sample is observed.

6.4 Conclusions

The p-type $Cu_{1+x}Se_2$ compounds were prepared by the high temperature liquid state mediated solid state and ball milling method combined with the SPS and hot press techniques. The phase structures, thermal transport and electronic properties of different compositions were investigated in a wide range of temperatures. It has been observed that the compositions of $Cu_{1+x}Se_2$ can exist in two different phases, tetragonal/monoclinic (α-) and cubic (β-) phases at room temperature. Due to the presence of these two phases the $Cu_{1+x}Se_2$ system displays anomalous changes in the electrical and thermal transport properties accompanying the α–β phase transformation around 400 K. Different synthetic procedures for samples with similar composition showed different thermoelectric properties at a given temperature. During these attempts, high energy shaker ball milling proved to be the most optimized method by which the

composition Cu_4Se_2 with highest ZT (~ 1.58 at 1000K) was made. With the solid -state method, higher electrical conductivity was achieved whereas with ball milling thermal conductivity was reduced drastically. In the future work, the thermoelectric efficiency of the $Cu_{1+x}Se_2$ with variation in Cu content would be investigated starting with the optimized method of shaker ball milling. Due to this addition, essential doping and nanostructuring would be possible which could tune both electronic and thermal transport properties to enhance the figure of merit of the material.

Chapter 7

CONCLUSION

7.1. Summary

This research includes a broad spectrum of materials, studied starting from the nanoscale to the bulk. A novel method for the synthesis of various oxide nanostructures with controllable parameters was designed. The methodology is very rapid, low cost and apt for various industrial high temperature applications. The structure-properties relations were also justified for all these nanostructures.

The remarkable achievement for the Nickel oxide nanostructure was that the oxidation state of the materials can be controlled by the synthesis conditions. Another remarkable contribution was the retention of the lower thermal conductivities of the nanostructures even at high temperatures, which is not possible with its bulk counterpart. These results opened new opportunities for these nanostructures to have a wider application. For Cobalt oxide nanostructures, the major finding was its magnetic behavior. It shows an inversion of structure from spinel to inverse spinel with the increase in its synthesis temperature. Thermal and electronic transport studies indicated a gradual reduction in the thermal conductivity of various Co_3O_4 samples upon decreasing the reaction ignition temperature. A strong variation in the electrical conductivity and thermopower

of various Co_3O_4 samples was also observed. Changes in the electronic properties were associated with alterations in the electronic band gap due to various degrees of Co^{2+}/Co^{3+} disorder in the structure of Co_3O_4, which in turn depends on the reaction ignition temperature.

For the half-Heusler system, we have observed the enhancement of thermoelectric figure of merit of p-type HH/FH nanocomposites by varying the percentages of FH nanoinclusion. The liquid state mediated solid state synthetic method and the excess cobalt concentration introduces nanoinclusions of FH into the bulk HH matrix, which in turn effectively boost the carrier (hole) mobility in the composites. This carrier mobility affects the Seebeck coefficient as well as the electron conductivities. The large increase in the Seebeck coefficient results from the filtering of low energy holes at nanometer scale HH/FH phase boundaries leading to a decrease in the carrier density around room temperature. This reduction in carrier density results in a large increase in the carrier mobility, which minimizes the loss in the electrical conductivity. At high temperatures, the electrical conductivity remarkably increases due to increase in carrier density that compensates for the decreasing carrier mobility. For the n-type system, we observed that the nanostructures coherently embedded within a semiconducting matrix tune the electronic behavior of existing charge carriers within the matrix, leading to a spectacular increase in the thermopower as well as a large enhancement in the carrier mobility within the resulting bulk nanocomposite. This approach substantially reduces the carrier density and increases the carrier effective mass within the HH/FH-QD nanocomposites, which contributes towards a larger thermopower. These samples also exhibited a dramatic increase in the electrical conductivities. The atomic -scale engineering at the nanoscale helped to magnify the thermopower and carrier mobility which in turn provides greater thrust to the figures of merit in thermoelectric materials intended for high performance energy conversion application.

For the p-type $Cu_{1+x}Se_2$ compounds, an extensive study on the synthetic routes revealed the optimized reaction condition to control its structural as well as the charge carriers transport properties. The high energy mechanical alloying made a revolutionary alteration in thermoelectrical behavior of the material by reducing its thermal conductivity and enhancing the power factor. All the compositions exhibited a strong phase transition. The structural disorder due to this phase transition increases the randomness to the system, which eventually manipulated the behavior of the charge carriers as well as the phonon. This manipulation led to a very high ZT compared to other p-type material.

7.2. Future Studies

From current research efforts, it has been revealed that inclusion phases with full-Heusler (FH) crystal structure can be grown conveniently within the half-Heusler matrix to form a HH (1-x)/FH(x) nanocomposites that are stable at moderate to high temperatures. This formation mostly walks through two different schemes. In the very first and conventional scheme the pre-synthesized HH matrix is subjected to a further addition of excess elemental metal which depends on the nature of starting HH matrix (p-type /n-type) below the melting point of both components. Due to the heat treatment, a solid state diffusion of the excess elemental metal atom into the vacant crystallographically independent atomic sites of the existing HH structure occurs. In this process of filling in the vacancy results in a solid state phase transformation of unit cells with HH structures into unit cells with FH structures which are typically in nanometer scales. However, as this process is not kinetically controlled, the composite grains obtained through this mechanism (Fig.7.1B) generally lead to large agglomerates of FH particles interconnected into

networks during material processing. This agglomeration often alters the predicted and desired properties of the material.

Another scheme to the formation of a HH/FH composite is achieved via direct combination of high purity elemental powders with desired stoichiometry at temperatures below the melting point of both HH and FH phases. With this approach the formation of HH and FH structures becomes quite easy due to the compatibility in composition and atomic arrangement of both the phases. As it started with the elements, the composition and structure (FH or HH) of seed crystals nucleating at various locations within the reaction mixture depend on the local stoichiometry. The formation of large composite grains of the HH/FH (Fig. 7.1F) largely arises from the merging of several neighboring seed crystals with HH or FH composition and structure. This growth mechanism is facilitated by the three dimensional structural similarity between the FH and HH structure (both crystallize with face-centered cubic structures with a small lattice mismatch of ~2.5%) which, in turn favors the endotaxial growth of spherically shaped FH inclusions within the HH matrix leading to the formation of coherent HH/FH interfaces within the composites. However the average size and distribution of these FH inclusions within individual grain are still not predictable as it strongly depends on population density of FH seed crystals as well as their proximity within the reaction mixture.

To ensure the homogeneity in the particle size and the dispersion of FH inclusions within the HH matrix, scheme 3 would be adopted which is the future goal of the present research. This scheme will follow multiple steps by starting with the complete melting of the stoichiometric elemental mixture above the melting point of each component with a fast quenching at room temperature. In the subsequent step the glass- like ingot obtained from the melt will be subjected to either mechanical alloying or liquid state mediated solid state diffusion for the formation of the FH/HH

composite. In the third step, the resulting product will be treated at various temperatures and duration. Alternately, the glass -like ingot can be also treated at different temperature and duration, skipping the alloying/solid state diffusion step would greatly use the concept of liquid state miscibility avoiding the issues raised in the previous schemes due to solid state immiscibility between the FH and HH phases. With this fabrication method, the melting process controls the ingots with small FH nuclei to be spaced more uniformly compared to the conventional slow cooling process. During the last step of temperature dependent ageing the

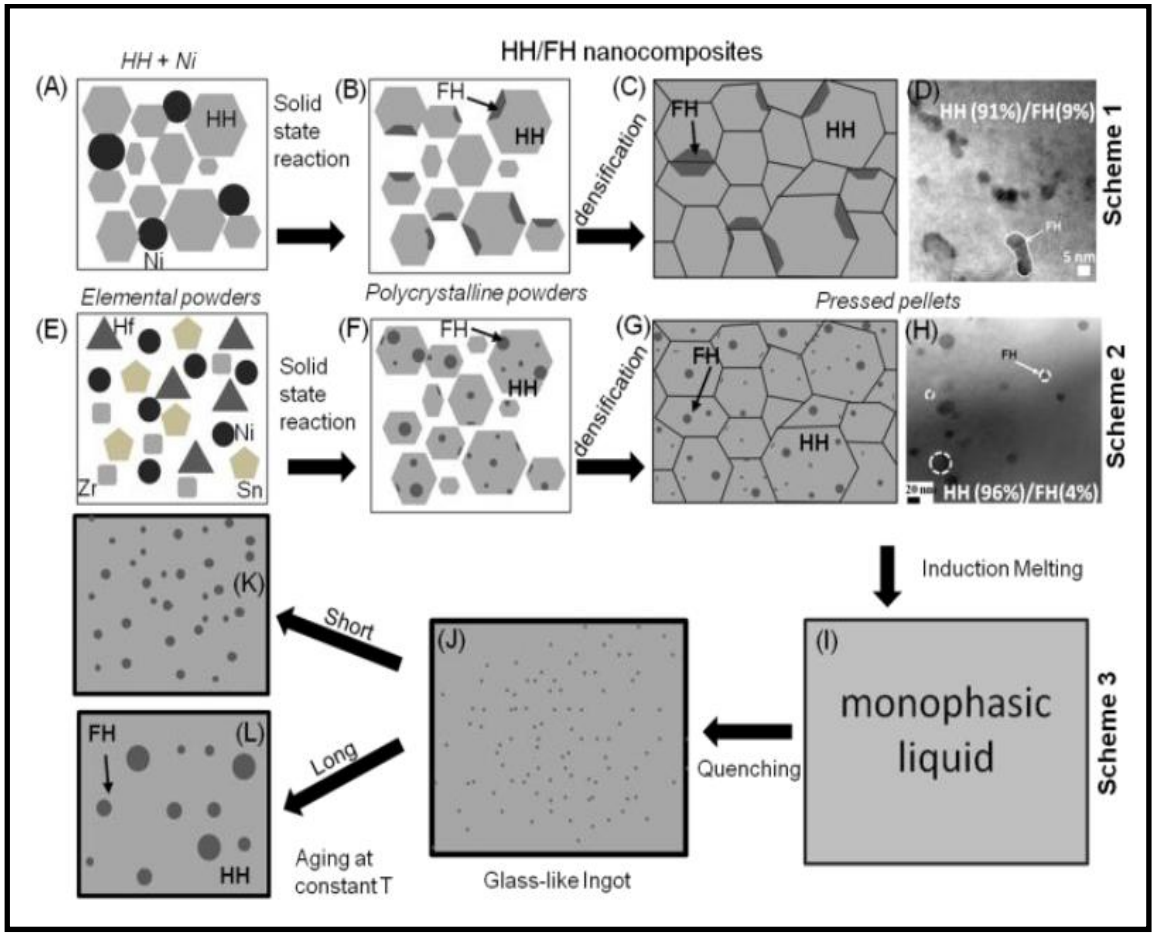

Figure 7.11 : Various strategies for formation of bulk HH/FH nanocomposites by varying the aging temperature-ageing time and microstructure evolution.

composite would show a complete and uniform segregation between HH and FH phases at high temperatures. Another effort would be time-dependent ageing by keeping the ageing temperature fixed and changing the time. This study is really important since the "ageing time" controls the pathway of the non-equilibrium monophasic HH(1-x)/FH(x) ingot which undergoes short range atomic ordering leading to the transition from non-crystalline disordered structure to finally a metastable crystalline ingot consisting of disordered small crystallites with HH or FH structure. After the appropriate aging time at the selected temperature profile, the thermal and electronic properties would be studied for the resulting equilibrated HH(1-x)/FH(x) composite.

REFERENCES

(1) Yu, B.; Liu, W.; Chen, S.; Wang, H.; Wang, H.; Chen, G.; Ren, Z. Nano Energy **2012**, 1, 472.

(2) Snyder, G. J.; Toberer, E. S. Nat Mater **2008**, 7, 105.

(3) Ward, E. M.; Schulte, P. A.; Straif, K.; Hopf, N. B.; Caldwell, J. C.; Carreón, T.; DeMarini, D. M.; Fowler, B. A.; Goldstein, B. D.; Hemminki, K. Environ Health Persp **2010**, 118, 1355.

(4) Biswas, K.; He, J. Q.; Zhang, Q. C.; Wang, G. Y.; Uher, C.; Dravid, V. P.; Kanatzidis, M. G. Nat Chem **2011**, 3, 160.

(5) Kanatzidis, M. G. Chem Mater **2010**, 22, 648.

(6) Vineis, C. J.; Shakouri, A.; Majumdar, A.; Kanatzidis, M. G. Adv Mater **2010**, 22, 3970.

(7) Ponnambalam, V.; Alboni, P. N.; Edwards, J.; Tritt, T. M.; Culp, S. R.; Poon, S. J. J Appl Phys **2008**, 103.

(8) Culp, S. R.; Simonson, J. W.; Poon, S. J.; Ponnambalam, V.; Edwards, J.; Tritt, T. M. Appl Phys Lett **2008**, 93.

(9) Sekimoto, T.; Kurosaki, K.; Muta, H.; Yamanaka, S. J Alloy Compd **2006**, 407, 326.

(10) Sekimoto, T.; Kurosaki, K.; Muta, H.; Yamanaka, S. Mater Trans **2006**, 47, 1445.

(11) Poudeu, P. F. R.; D'Angelo, J.; Downey, A. D.; Short, J. L.; Hogan, T. P.; Kanatzidis, M. G. Angew Chem Int Edit **2006**, 45, 3835.

(12) Culp, S. R.; Poon, S. J.; Hickman, N.; Tritt, T. M.; Blumm, J. Appl Phys Lett **2006**, 88.

(13) Kawaharada, Y.; Kurosaki, K.; Muta, H.; Uno, M.; Yamanaka, S. J Alloy Compd **2004**, 377, 312.

(14) Xia, Y.; Bhattacharya, S.; Ponnambalam, V.; Pope, A. L.; Poon, S. J.; Tritt, T. M. J Appl Phys **2000**, 88, 1952.

(15) Uher, C.; Yang, J.; Hu, S.; Morelli, D. T.; Meisner, G. P. Phys Rev B **1999**, 59, 8615.

(16) Saqr, K. M.; Mansour, M. K.; Musa, M. N. Int J Automot Techn **2008**, 9, 155.

(17) Fleurial, J. P.; Borshchevsky, A.; Caillat, T.; Ewell, R. Iecec-97 - Proceedings of the Thirty-Second Intersociety Energy Conversion Engineering Conference, Vols 1-4 **1997**, 1080.

(18) Vorobiev, Y.; Gonzalez-Hernandez, J.; Vorobiev, P.; Bulat, L. Sol Energy **2006**, 80, 170.

(19) Boukai, A. I.; Bunimovich, Y.; Tahir-Kheli, J.; Yu, J. K.; Goddard, W. A.; Heath, J. R. Nature **2008**, 451, 168.

(20) Harman, T. C.; Taylor, P. J.; Walsh, M. P.; LaForge, B. E. Science **2002**, 297, 2229.

(21) Rhyee, J. S.; Lee, K. H.; Lee, S. M.; Cho, E.; Il Kim, S.; Lee, E.; Kwon, Y. S.; Shim, J. H.; Kotliar, G. Nature **2009**, 459, 965.

(22) Sootsman, J. R.; Chung, D. Y.; Kanatzidis, M. G. Angew Chem Int Edit **2009**, 48, 8616.

(23) Lan, Y. C.; Minnich, A. J.; Chen, G.; Ren, Z. F. Adv Funct Mater **2010**, 20, 357.

(24) Dresselhaus, M. S.; Chen, G.; Tang, M. Y.; Yang, R. G.; Lee, H.; Wang, D. Z.; Ren, Z. F.; Fleurial, J. P.; Gogna, P. Adv Mater **2007**, 19, 1043.

(25) Minnich, A. J.; Dresselhaus, M. S.; Ren, Z. F.; Chen, G. Energ Environ Sci **2009**, 2, 466.

(26) Hicks, L. D.; Dresselhaus, M. S. Phys Rev B **1993**, 47, 16631.

(27) Hicks, L. D.; Dresselhaus, M. S. Phys Rev B **1993**, 47, 12727.

(28) Hicks, L. D.; Harman, T. C.; Dresselhaus, M. S. Appl Phys Lett **1993**, 63, 3230.

(29) Sales, B.; Mandrus, D.; Williams, R. K. Science **1996**, 272, 1325.

(30) Li, H.; Tang, X.; Zhang, Q.; Uher, C. Appl Phys Lett **2009**, 94, 102114.

(31) Nolas, G.; Morelli, D.; Tritt, T. M. Annual Review of Materials Science **1999**, 29, 89.

(32) Nolas, G.; Cohn, J.; Slack, G.; Schujman, S. Appl Phys Lett **1998**, 73, 178.

(33) Iversen, B. B.; Palmqvist, A. E.; Cox, D. E.; Nolas, G. S.; Stucky, G. D.; Blake, N. P.; Metiu, H. J Solid State Chem **2000**, 149, 455.

(34) Chung, D.-Y.; Iordanidis, L.; Choi, K.-S.; Kanatzidis, M. G. BULLETIN-KOREAN CHEMICAL SOCIETY **1998**, 19, 1283.

(35) Hsu, K. F.; Loo, S.; Guo, F.; Chen, W.; Dyck, J. S.; Uher, C.; Hogan, T.; Polychroniadis, E.; Kanatzidis, M. G. Science **2004**, 303, 818.

(36) Lin, H.; Wray, L. A.; Xia, Y.; Xu, S.; Jia, S.; Cava, R. J.; Bansil, A.; Hasan, M. Z. Nat Mater **2010**, 9, 546.

(37) Uher, C.; Yang, J.; Hu, S.; Morelli, D.; Meisner, G. Phys Rev B **1999**, 59, 8615.

(38) Poon, G. J. Semiconductors and Semimetals **2001**, 70, 37.

(39) Jeitschko, W. Metall. Trans. **1970**, 1, 3159.

(40) Webster, P. J.; Ziebeck, K. R. A. Landolt-Börnstein-group III condensed matter; Berlin: Springer, 1988; Vol. 19C.

(41) Makongo, J. P. A.; Misra, D. K.; Salvador, J. R.; Takas, N. J.; Wang, G.; Shabetai, M. R.; Pant, A.; Paudel, P.; Uher, C.; Stokes, K. L.; Poudeu, P. F. P. J. Solid State Chem. **2011**, 184 2948

(42) Makongo, J. P. A.; Misra, D. K.; Zhou, X. Y.; Pant, A.; Shabetai, M. R.; Su, X. L.; Uher, C.; Stokes, K. L.; Poudeu, P. F. P. J Am Chem Soc **2011**, 133, 18843.

(43) Misra, D. K.; Makongo, J. P. A.; Sahoo, P.; Shabetai, M. R.; Paudel, P.; Stokes, K. L.; Poudeu, P. F. P. Sci Adv Mater **2011**, 3, 607.

(44) Takas, N. J.; Sahoo, P.; Misra, D.; Zhao, H. F.; Henderson, N. L.; Stokes, K.; Poudeu, P. F. P. J Electron Mater **2011**, 40, 662.

(45) Yaqub, R.; Sahoo, P.; Makongo, J. P. A.; Takas, N.; Poudeu, P. F. P.; Stokes, K. L. Sci Adv Mater **2011**, 3, 633.

(46) Culp, S. R.; Simonson, J. W.; Poon, S. J.; Ponnambalam, V.; Edwards, J.; Tritt, T. M. Appl Phys Lett **2008**, 93, 022105.

(47) Poon, S. J. In Semiconductor and Semimetals; Tritt, T. M., Ed.; Academic: New York, 2001; Vol. 70, p 37.

(48) Aliev, F. G.; Brandt, N. B.; Moshchalkov, V. V.; Kozyrkov, V. V.; Skolozdra, R. V.; Belogorokhov, A. I. Z Phys B Con Mat **1989**, 75, 167.

(49) Aliev, F. G.; Kozyrkov, V. V.; Moshchalkov, V. V.; Scolozdra, R. V.; Durczewski, K. Z Phys B Con Mat **1990**, 80, 353.

(50) Simonson, J. W.; Poon, S. J. J. Phys.: Condens. Matter **2008**, 20, 255220.

(51) Barth, J.; Balke, B.; Fecher, G. H.; Stryhanyuk, H.; Gloskovskii, A.; Naghavi, S.; Felser, C. J Phys D Appl Phys **2009**, 42, 185401.

(52) Chaput, L.; Tobola, J.; Pecheur, P.; Scherrer, H. Phys Rev B **2006**, 73, 045121.

(53) Sakurada, S.; Shutoh, N. Appl Phys Lett **2005**, 86, 082105.

(54) Uher, C.; Yang, J.; Hu, S.; Morelli, D. T.; Meisner, G. P. Physical Review B **1999**, 59, 8615.

(55) Nanda, B. R. K.; Dasgupta, I. J Phys-Condens Mat **2005**, 17, 5037.

(56) Kroth, K.; Balke, B.; Fecher, G. H.; Ksenofontov, V.; Felser, C.; Lin, H. J. Appl Phys Lett **2006**, 89, 202509.

(57) Ouardi, S.; Fecher, G. H.; Balke, B.; Kozina, X.; Stryganyuk, G.; Felser, C.; Lowitzer, S.; Kodderitzsch, D.; Ebert, H.; Ikenaga, E. Phys Rev B **2010**, 82, 085108.

(58) Sanyal, B.; Eriksson, O.; Suresh, K. G.; Dasgupta, I.; Nigam, A. K.; Nordblad, P. Appl Phys Lett **2006**, 89, 212502.

(59) Lin, H.; Wray, L. A.; Xia, Y. Q.; Xu, S. Y.; Jia, S. A.; Cava, R. J.; Bansil, A.; Hasan, M. Z. Nat Mater **2010**, 9, 546.

(60) Chadov, S.; Qi, X. L.; Kubler, J.; Fecher, G. H.; Felser, C.; Zhang, S. C. Nat Mater **2010**, 9, 541.

(61) Xiao, D.; Yao, Y. G.; Feng, W. X.; Wen, J.; Zhu, W. G.; Chen, X. Q.; Stocks, G. M.; Zhang, Z. Y. Phys Rev Lett **2010**, 105, 096404.

(62) Graf, T.; Felser, C.; Parkin, S. S. P. Prog Solid State Ch **2011**, 39, 1.(63) Chrissafis, K.; Paraskevopoulos, K.; Manolikas, C. J Therm Anal Calorim **2006**, 84, 195.

(64) Skomorokhov, A.; Trots, D.; Knapp, M.; Bickulova, N.; Fuess, H. J Alloy Compd **2006**, 421, 64.

(65) Heyding, R. D.; Murray, R. M. Canadian Journal of Chemistry **1976**, 54, 841.

(66) Okada, Y.; Ohtani, T.; Yokota, Y.; Tachibana, Y.; Morishige, K. Journal of electron microscopy **2000**, 49, 25.

(67) Cao, Y. Q.; Zhu, T. J.; Zhao, X. B. J. Alloy Compd. **2008**, 449, 109.

(68) Poudel, B.; Wang, W. Z.; Wang, D. Z.; Huang, J. Y.; Ren, Z. F. J. Nanosci. Nanotechno. **2006**, 6, 1050.

(69) Wang, W. Z.; Poudel, B.; Wang, D. Z.; Ren, Z. F. Adv. Mater. **2005**, 17, 2110.

(70) Wang, W. Z.; Poudel, B.; Yang, J.; Wang, D. Z.; Ren, Z. F. J. Am. Chem. Soc. **2005**, 127, 13792.

(71) Zhu, T. J.; Liu, Y. Q.; Zhao, X. B. Mater. Res. Bull. **2008**, 43, 2850.

(72) Martin, J.; Nolas, G. S.; Zhang, W.; Chen, L. Appl. Phys. Lett. **2007**, 90, 222112.

(73) Bertini, L.; Stiewe, C.; Toprak, M.; Williams, S.; Platzek, D.; Mrotzek, A.; Zhang, Y.; Gatti, C.; Muller, E.; Muhammed, M.; Rowe, M. J. Appl. Phys. **2003**, 93, 438.

(74) Joraide, A. A. J. Mater. Sci. **1995**, 30, 744.

(75) Joshi, G.; Lee, H.; Lan, Y. C.; Wang, X. W.; Zhu, G. H.; Wang, D. Z.; Gould, R. W.; Cuff, D. C.; Tang, M. Y.; Dresselhaus, M. S.; Chen, G.; Ren, Z. F. Nano Lett. **2008**, 8, 4670.

(76) Kim, S. S.; Yamamoto, S.; Aizawa, T. J. Alloy Compd. **2004**, 375, 107.

(77) Kishimoto, K.; Koyanagi, T. J. Appl. Phys. **2002**, 92, 2544.

(78) Ma, Y.; Hao, Q.; Poudel, B.; Lan, Y. C.; Yu, B.; Wang, D. Z.; Chen, G.; Ren, Z. F. Nano Lett. **2008**, 8, 2580.

(79) Poudel, B.; Hao, Q.; Ma, Y.; Lan, Y. C.; Minnich, A.; Yu, B.; Yan, X.; Wang, D. Z.; Muto, A.; Vashaee, D.; Chen, X. Y.; Liu, J. M.; Dresselhaus, M. S.; Chen, G.; Ren, Z. Science **2008**, 320, 634.

(80) Rowe, D. M.; Shukla, V. S.; Savvides, N. Nature **1981**, 290, 765.

(81) Wang, H.; Li, J. F.; Nan, C. W.; Zhou, M.; Liu, W. S.; Zhang, B. P.; Kita, T. Appl Phys Lett **2006**, 88, 092104.

(82) Wang, X. W.; Lee, H.; Lan, Y. C.; Zhu, G. H.; Joshi, G.; Wang, D. Z.; Yang, J.; Muto, A. J.; Tang, M. Y.; Klatsky, J.; Song, S.; Dresselhaus, M. S.; Chen, G.; Ren, Z. F. Appl. Phys. Lett. **2008**, 93, 193121.

(83) Yang, J. Y.; Chen, R. G.; Fan, X. A.; Bao, S. Q.; Zhu, W. J. Alloy Compd. **2006**, 407, 330.

(84) Yang, J. Y.; Fan, X. A.; Chen, R. G.; Zhu, W.; Bao, S. Q.; Duan, X. K. J. Alloy Compd. **2006**, 416, 270.

(85) Zhu, G. H.; Lee, H.; Lan, Y. C.; Wang, X. W.; Joshi, G.; Wang, D. Z.; Yang, J.; Vashaee, D.; Guilbert, H.; Pillitteri, A.; Dresselhaus, M. S.; Chen, G.; Ren, Z. F. Phys. Rev. Lett. **2009**, 102, 196803.

(86) Androulakis, J.; Hsu, K. F.; Pcionek, R.; Kong, H.; Uher, C.; DAngelo, J. J.; Downey, A.; Hogan, T.; Kanatzidis, M. G. Adv. Mater. **2006**, 18, 1170.

(87) Gueguen, A.; Poudeu, P. F. P.; Li, C. P.; Moses, S.; Uher, C.; He, J. Q.; Dravid, V.; Paraskevopoulos, K. A.; Kanatzidis, M. G. Chem Mater **2009**, 21, 1683.

(88) Hsu, K. F.; Loo, S.; Guo, F.; Chen, W.; Dyck, J. S.; Uher, C.; Hogan, T.; Polychroniadis, E. K.; Kanatzidis, M. G. Science **2004**, 303, 818.

(89) Poudeu, P. F. P.; D'Angelo, J.; Kong, H. J.; Downey, A.; Short, J. L.; Pcionek, R.; Hogan, T. P.; Uher, C.; Kanatzidis, M. G. J. Am. Chem. Soc. **2006**, 128, 14347.

(90) Maji, P.; Takas, N. J.; Misra, D. K.; Gabrisch, H.; Stokes, K.; Poudeu, P. F. P. J. Solid State Chem. **2010**, 183, 1120.

(91) Poudeu, P. F. P.; D'Angelo, J.; Downey, A. D.; Short, J. L.; Hogan, T. P.; Kanatzidis, M. G. Angew Chem Int Edit **2006**, 45, 3835.

(92) Sootsman, J. R.; He, J. Q.; Dravid, V. P.; Ballikaya, S.; Vermeulen, D.; Uher, C.; Kanatzidis, M. G. Chem. Mater. **2010**, 22, 869.

(93) Sootsman, J. R.; He, J. Q.; Dravid, V. P.; Li, C. P.; Uher, C.; Kanatzidis, M. G. J. Appl. Phys. **2009**, 105, 083718.

(94) Sootsman, J. R.; Kong, H.; Uher, C.; D'Angelo, J. J.; Wu, C. I.; Hogan, T. P.; Caillat, T.; Kanatzidis, M. G. Angew Chem Int Edit **2008**, 47, 8618.

(95) Sootsman, J. R.; Pcionek, R. J.; Kong, H. J.; Uher, C.; Kanatzidis, M. G. Chem. Mater. **2006**, 18, 4993.

(96) Chen, L. D.; Huang, X. Y.; Zhou, M.; Shi, X.; Zhang, W. B. J. Appl. Phys. **2006**, 99, 064305

(97) Huang, X. Y.; Xu, Z.; Chen, L. D. Solid State Commun. **2004**, 130, 181.

(98) Wang, Y.; Zhang, Y. F.; Liu, H. R.; Yu, S. J.; Qin, Q. Z. Electrochim Acta **2003**, 48, 4253.

(99) Magana, C. R.; Acosta, D. R.; Martinez, A. I.; Ortega, J. M. Sol Energy **2006**, 80, 161.

(100) Hotovy, I.; Huran, J.; Spiess, L.; Romanus, H.; Capone, S.; Rehacek, V.; Taurino, A. M.; Donoval, D.; Siciliano, P. J Phys: Conf. Series **2007**, 61, 435

(101) Kodama, R. H.; Berkowitz, A. E. Phys Rev B **1999**, 59, 6321.

(102) Vining, C. B.; Laskow, W.; Hanson, J. O.; der Beck, R. R. V.; Gorsuch, P. D. J Appl Phys **1991**, 69, 4333.

(103) Dessombz, A.; Chiche, D.; Davidson, P.; Panine, P.; Chaneac, C.; Jolivet, J. P. J Am Chem Soc **2007**, 129, 5904.

(104) Jolivet, J. P.; Froidefond, C.; Pottier, A.; Chaneac, C.; Cassaignon, S.; Tronc, E.; Euzen, P. J Mater Chem **2004**, 14, 3281.

(105) Matijevic, E. Annu Rev Mater Sci **1985**, 15, 483.

(106) Matijevic, E. Chem Mater **1993**, 5, 412.

(107) Portehault, D.; Cassaignon, S.; Baudrin, E.; Jolivet, J. P. Chem Mater **2007**, 19, 5410.

(108) Rao, K. V.; Sunandana, C. S. J Nanosci Nanotechno **2008**, 8, 4247.

(109) Sietsma, J. R. A.; Meeldijk, J. D.; den Breejen, J. P.; Versluijs-Helder, M.; van Dillen, A. J.; de Jongh, P. E.; de Jong, K. P. Angew Chem Int Edit **2007**, 46, 4547.

(110) Mukasyan, A. S.; Epstein, P.; Dinka, P. In Proceedings of the Combustion Institute 2007; Vol. 31, p 1789.

(111) Kingsley, J. J.; Patil, K. C. Mater Lett **1988**, 6, 427.

(112) Keem, J. E.; Honig, J. M. , CINDAS 1978.

(113) Prasad, M.; Tendulkar, M. G. Journal of Chemical Society **1931**, 1, 1403.

(114) Niklasson, G. A.; Granqvist, C. G. Journal of Material Chemistry **2007**, 17, 127.

(115) Sasaki, S.; Fujino, K.; Takeuchi, Y. Proceedings of The Japan Academy **1979**, 55, 43.

(116) Cairns, R. W.; Ott, E. J Am Chem Soc **1933**, 55, 527.

(117) Greenwood, N. N.; Earnshaw, A. In Chemistry of the Elements; 2 ed. Butterworth, UK, 1997.

(118) Rowe, D. M.; Fu, L. W.; Williams, S. G. K. J Appl Phys **1993**, 73, 4683.

(119) Lewis, F. B.; Saunders, N. H. J Phys C: Solid State Phys **1973**, 6, 2525.

(120) Stern, H. Journal of Physical Chemistry Solids **1965**, 26, 153.

(121) Sahoo, P.; Misra, D. K.; Salvador, J.; Makongo, J. P. A.; Chaubey, G. S.; Takas, N. J.; Wiley, J. B.; Poudeu, P. F. P. J Solid State Chem **2012**, 190, 29.

(122) Kundu, S.; Nelson, A. J.; McCall, S. K.; van Buuren, T.; Liang, H. J Nanopart Res **2013**, 15, 1587.

(123) Yang, C.; Wu, J. J.; Hou, Y. L. Chem Commun **2011**, 47, 5130.

(124) Prasad, K. P. S.; Dhawale, D. S.; Joseph, S.; Anand, C.; Wahab, M. A.; Mano, A.; Sathish, C. I.; Balasubramanian, V. V.; Sivakumar, T.; Vinu, A. Micropor Mesopor Mat **2013**, 172, 77.

(125) Schladt, T. D.; Schneider, K.; Shukoor, M. I.; Natalio, F.; Bauer, H.; Tahir, M. N.; Weber, S.; Schreiber, L. M.; Schroder, H. C.; Muller, W. E. G.; Tremel, W. J Mater Chem **2010**, 20, 8297.

(126) Azizian-Kalandaragh, Y.; Khodayari, A.; Zeng, Z. P.; Garoufalis, C. S.; Baskoutas, S.; Gontard, L. C. J Nanopart Res **2013**, 15, 1388

(127) Ma, M. X.; Pan, Z. Y.; Wang, W. J.; Guo, L.; Li, J. H.; Wu, Z. Y.; Yang, S. H. J Nanosci Nanotechnlogy **2013**, 13, 864.

(128) Grzelczak, M.; Zhang, J. S.; Pfrommer, J.; Hartmann, J.; Driess, M.; Antonietti, M.; Wang, X. C. Acs Catal **2013**, 3, 383.

(129) Yamada, Y.; Yano, K.; Fukuzumi, S. Energ Environ Sci **2012**, 5, 5356.

(130) Liao, M. J.; Feng, J. Y.; Luo, W. J.; Wang, Z. Q.; Zhang, J. Y.; Li, Z. S.; Yu, T.; Zou, Z. G. Adv Funct Mater **2012**, 22, 3066.

(131) Choi, B. G.; Chang, S. J.; Lee, Y. B.; Bae, J. S.; Kim, H. J.; Huh, Y. S. Nanoscale **2012**, 4, 5924.

(132) Zhan, L.; Wang, Y. L.; Qiao, W. M.; Ling, L. C.; Yang, S. B. Electrochim Acta **2012**, 78, 440.

(133) Liu, B.; Zhang, X. B.; Shioyama, H.; Mukai, T.; Sakai, T.; Xu, Q. J Power Sources **2010**, 195, 857.

(134) Tao, F. F.; Gao, C. L.; Wen, Z. H.; Wang, Q.; Li, J. H.; Xu, Z. J Solid State Chem **2009**, 182, 1055.

(135) Hu, J. Q.; Wen, Z. H.; Wang, Q.; Yao, X.; Zhang, Q.; Zhou, J. H.; Li, J. H. J Phys Chem B **2006**, 110, 24305.

(136) Zhan, F. M.; Geng, B. Y.; Guo, Y. J. Chem-Eur J **2009**, 15, 6169.

(137) Zhang, H.; Wu, J. B.; Zhai, C. X.; Ma, X. Y.; Du, N.; Tu, J. P.; Yang, D. R. Nanotechnology **2008**, 19, 035711.

(138) Li, Y. G.; Tan, B.; Wu, Y. Y. Nano Lett **2008**, 8, 265.

(139) Lou, X. W.; Deng, D.; Lee, J. Y.; Archer, L. A. J Mater Chem **2008**, 18, 4397.

(140) Lou, X. W.; Deng, D.; Lee, J. Y.; Feng, J.; Archer, L. A. Adv Mater **2008**, 20, 258.

(141) Du, N.; Zhang, H.; Chen, B.; Wu, J. B.; Ma, X. Y.; Liu, Z. H.; Zhang, Y. Q.; Yang, D.; Huang, X. H.; Tu, J. P. Adv Mater **2007**, 19, 4505.

(142) Thota, S.; Kumar, A.; Kumar, J. Mater Sci Eng B-Adv **2009**, 164, 30.

(143) Teng, Y. H.; Yamamoto, S.; Kusano, Y.; Azuma, M.; Shimakawa, Y. Mater Lett **2010**, 64, 239.

(144) Ren, L.; Wang, P. P.; Han, Y. S.; Hu, C. W.; Wei, B. Q. Chem Phys Lett **2009**, 476, 78.

(145) Groven, L. J.; Pfeil, T. L.; Pourpoint, T. L. Int J Hydrogen Energ **2013**, 38, 6377.

(146) Wen, W.; Wu, J. M.; Tu, J. P. J Alloy Compd **2012**, 513, 592.

(147) Toniolo, J. C.; Takimi, A. S.; Bergmann, C. P. Mater Res Bull **2010**, 45, 672.

(148) Resnick, D. A.; Gilmore, K.; Idzerda, Y. U.; Klem, M. T.; Allen, M.; Douglas, T.; Arenholz, E.; Young, M. J Appl Phys **2006**, 99, 08Q501.

(149) Zhang, R. J.; Willis, R. F. Phys Rev Lett **2001**, 86, 2665.

(150) Dutta, P.; Seehra, M. S.; Thota, S.; Kumar, J. J Phys-Condens Mat **2008**, 20, 015218.

(151) Roth, W. L. J Phys Chem Solids **1964**, 25, 1.

(152) Ramirez, A. P. J Appl Phys **1991**, 70, 5952.

(153) Ramirez, A. P. Annu Rev Mater Sci **1994**, 24, 453.

(154) Chen, W. M.; Chen, C. P.; Guo, L. J Appl Phys **2010**, 108, 073907.

(155) Bai, L. G.; Pravica, M.; Zhao, Y. S.; Park, C.; Meng, Y.; Sinogeikin, S. V.; Shen, G. Y. J Phys-Condens Mat **2012**, 24, 435401.

(156) Salem, A. M.; Selim, M. S. J Phys D Appl Phys **2001**, 34, 12.

(157) Gu, F.; Li, C. Z.; Hu, Y. J.; Zhang, L. J Cryst Growth **2007**, 304, 369.

(158) Barreca, D.; Massignan, C.; Daolio, S.; Fabrizio, M.; Piccirillo, C.; Armelao, L.; Tondello, E. Chem Mater **2001**, 13, 588.

(159) Xu, R.; Zeng, H. C. Langmuir **2004**, 20, 9780.

(160) He, T.; Chen, D. R.; Jiao, X. L.; Wang, Y. L.; Duan, Y. Z. Chem Mater **2005**, 17, 4023.

(161) Liu, S. L.; Hu, H. Z.; Zhou, J. P.; Zhang, L. N. Cellulose **2011**, 18, 1273.

(162) Pal, J.; Chauhan, P. Mater Charact **2010**, 61, 575.

(163) Keng, P. Y.; Kim, B. Y.; Shim, I. B.; Sahoo, R.; Veneman, P. E.; Armstrong, N. R.; Yoo, H.; Pemberton, J. E.; Bull, M. M.; Griebel, J. J.; Ratcliff, E. L.; Nebesny, K. G.; Pyun, J. Acs Nano **2009**, 3, 3143.

(164) Mocala, K.; Navrotsky, A.; Sherman, D. M. Phys Chem Miner **1992**, 19, 88.

(165) Poudeu, P. F. P.; Gueguen, A.; Wu, C. I.; Hogan, T.; Kanatzidis, M. G. Chem Mater **2010**, 22, 1046.

(166) Yan, X.; Joshi, G.; Liu, W.; Lan, Y.; Wang, H.; Lee, S.; Simonson, J. W.; Poon, S. J.; Tritt, T. M.; Chen, G.; Ren, Z. F. Nano Lett **2011**, 11, 556.

(167) Heremans, J. P.; Jovovic, V.; Toberer, E. S.; Saramat, A.; Kurosaki, K.; Charoenphakdee, A.; Yamanaka, S.; Snyder, G. J. Science **2008**, 321, 554.

(168) Pei, Y. Z.; Shi, X. Y.; LaLonde, A.; Wang, H.; Chen, L. D.; Snyder, G. J. Nature **2011**, 473, 66.

(169) He, J. Q.; Sootsman, J. R.; Xu, L. Q.; Girard, S. N.; Zheng, J. C.; Kanatzidis, M. G.; Dravid, V. P. J Am Chem Soc **2011**, 133, 8786.

(170) Johnsen, S.; He, J. Q.; Androulakis, J.; Dravid, V. P.; Todorov, I.; Chung, D. Y.; Kanatzidis, M. G. J Am Chem Soc **2011**, 133, 3460.

(171) Poudeu, P. F.; Salvador, J.; Sakamoto, J. Sci Adv Mater **2011**, 3, 515.

(172) Tritt, T. M.; Bottner, H. J Mater Res **2011**, 26, 1743.

(173) Androulakis, J.; Lin, C. H.; Kong, H. J.; Uher, C.; Wu, C. I.; Hogan, T.; Cook, B. A.; Caillat, T.; Paraskevopoulos, K. M.; Kanatzidis, M. G. J Am Chem Soc **2007**, 129, 9780.

(174) Venkatasubramanian, R.; Siivola, E.; Colpitts, T.; O'Quinn, B. Nature **2001**, 413, 597.

(175) Mi, J. L.; Zhao, X. B.; Zhu, T. J.; Tu, J. P. Appl Phys Lett **2007**, 91, 172116.

(176) Zide, J. M. O.; Vashaee, D.; Bian, Z. X.; Zeng, G.; Bowers, J. E.; Shakouri, A.; Gossard, A. C. Phys Rev B **2006**, 74, 205335.

(177) Heavily Doped Semiconductors Fistul, V. I., Ed.; Plenum: New York, 1969.

(178) Makongo, J. P. A.; Misra, D. K.; Zhou, X.; Pant, A.; Shabetai, M. R.; Su, X.; Uher, C.; Stokes, K. L.; Poudeu, P. F. P. Journal of the American Chememical Society **2011**, 133, 18843.

(179) Liu, Y.; Sahoo, P.; Makongo, J. P. A.; Zhou, X.; Kim, S.-J.; Chi, H.; Uher, C.; Pan, X.; Poudeu, P. F. P. Journal of the American Chemical Society **2013**, 135, 7486.

(180) Chai, Y. W.; Kimura, Y. Appl Phys Lett **2012**, 100, 033114.

(181) Populoh, S.; Aguirre, M. H.; Brunko, O. C.; Galazka, K.; Lu, Y.; Weidenkaff, A. Scripta Materialia **2012**, 66, 1073.

(182) Sumithra, S.; Takas, N. J.; Nolting, W. M.; Sapkota, S.; Poudeu, P. F. P.; Stokes, K. L. J. Electronic Mater. **2012**, 41, 1401.

(183) Zhao, L.-D.; He, J.; Hao, S.; Wu, C.-I.; Hogan, T. P.; Wolverton, C.; Dravid, V. P.; Kanatzidis, M. G. J Am Chem Soc **2012**, 134, doi.org/10.1021/ja306527n.

(184) Biswas, K.; He, J.; Blum, I. D.; Wu, C.-I.; Hogan, T. P.; Seidman, D. N.; Dravid, V. P.; Kanatzidis, M. G. Nature **2012**, 489, 414.

(185) Hazama, H.; Matsubara, M.; Asahi, R.; Takeuchi, T. Journal of Applied Physics **2011**, 110, 063710.

(186) Douglas, J. E.; Birkel, C. S.; Miao, M. S.; Torbet, C. J.; Stucky, G. D.; Pollock, T. M.; Seshadri, R. Applied Physics Letters **2012**, 101, 183902.

(187) Xie, W. J.; Yan, Y. G.; Zhu, S.; Zhou, M.; Populoh, S.; Gałazka, K.; Poon, S. J.; Weidenkaff, A.; He, J.; Tang, X. F.; Tritt, T. M. Acta Materialia **2013**, 61, 2087.

(188) Xie, W. J.; He, J.; Zhu, S.; Su, X. L.; Wang, S. Y.; Holgate, T.; Graff, J. W.; Ponnambalam, V.; Poon, S. J.; Tang, X. F.; Zhang, Q. J.; Tritt, T. M. Acta Materialia **2010**, 58, 4705.

(189) Xie, W.; Weidenkaff, A.; Tang, X.; Zhang, Q. C.; Poon, J.; Tritt, T. M. Nanomaterials **2012**, 2, 379.

(190) Hohl, H.; Ramirez, A. P.; Goldmann, C.; Ernst, G.; Wolfing, B.; Bucher, E. J Phys-Condens Mat **1999**, 11, 1697.

(191) Huang, P. K.; Yeh, J. W.; Shun, T. T.; Chen, S. K. Adv Eng Mater **2004**, 6, 74.

(192) Wang, X. F.; Zhang, Y.; Qiao, Y.; Chen, G. L. Intermetallics **2007**, 15, 357.

(193) Benjamin, J. S. Sci Am **1976**, 234, 40.

(194) Suryanarayana, C.; Ivanov, E.; Boldyrev, V. V. Mat Sci Eng a-Struct **2001**, 304, 151.

(195) Schwarz, R. B.; Petrich, R. R.; Saw, C. K. J Non-Cryst Solids **1985**, 76, 281.

(196) Sriharitha, R.; Murty, B. S.; Kottada, R. S. Intermetallics **2013**, 32, 119.

(197) Koch, C. C.; Cavin, O. B.; Mckamey, C. G.; Scarbrough, J. O. Appl Phys Lett **1983**, 43, 1017.

(198) Politis, C.; Johnson, W. L. J Appl Phys **1986**, 60, 1147.

(199) Antolak-Dudka, A.; Krasnowski, M.; Kulik, T. Intermetallics **2013**, 42, 41.

(200) Krasnowski, M.; Gierlotka, S.; Kulik, T. Intermetallics **2013**, 42, 35.

(201) Ipus, J. J.; Blazquez, J. S.; Franco, V.; Conde, A. J Appl Phys **2013**, 113.

(202) Slack, G. Boca Raton **1995**, 407.

(203) Christensen, M.; Abrahamsen, A. B.; Christensen, N. B.; Juranyi, F.; Andersen, N. H.; Lefmann, K.; Andreasson, J.; Bahl, C. R.; Iversen, B. B. Nat Mater **2008**, 7, 811.

(204) Yuanfeng, L.; Sahoo, P.; Makongo, J. P.; Zhou, X.; Kim, S.-J.; Chi, H.; Uher, C.; Pan, X.; Poudeu, P. F. P. J Am Chem Soc **2013**.

(205) Sahoo, P.; Liu, Y.; Makongo, J. P.; Su, X.-l.; Kim, S. J.; Takas, N.; Chi, H.; Uher, C.; Pan, X.; Poudeu, P. F. Nanoscale **2013**.

(206) Makongo, J. P.; Misra, D. K.; Zhou, X.; Pant, A.; Shabetai, M. R.; Su, X.; Uher, C.; Stokes, K. L.; Poudeu, P. F. J Am Chem Soc **2011**, 133, 18843.

(207) Poudel, B.; Hao, Q.; Ma, Y.; Lan, Y.; Minnich, A.; Yu, B.; Yan, X.; Wang, D.; Muto, A.; Vashaee, D. Science **2008**, 320, 634.

(208) Rhyee, J.-S.; Lee, K. H.; Lee, S. M.; Cho, E.; Kim, S. I.; Lee, E.; Kwon, Y. S.; Shim, J. H.; Kotliar, G. Nature **2009**, 459, 965.

(209) Liu, H.; Shi, X.; Xu, F.; Zhang, L.; Zhang, W.; Chen, L.; Li, Q.; Uher, C.; Day, T.; Snyder, G. J. Nat Mater **2012**, 11, 422.

(210) Tonejc, A.; Ogorelec, Z.; Mestnik, B. Journal of Applied Crystallography **1975**, 8, 375.

(211) Chakrabarti, D.; Laughlin, D. Journal of Phase Equilibria **1981**, 2, 305.

(212) Glazov, V.; Pashinkin, A.; Fedorov, V. Inorganic materials **2000**, 36, 641.

(213) Murray, R.; Heyding, R. Can. J. Chem **1976**, 54, 841.

(214) Oliveria, M.; Mcmullan, R. K.; Wuensch, B. J. Solid State Ionics **1988**, 28, 1332.

(215) Liu, H. L.; Shi, X.; Xu, F. F.; Zhang, L. L.; Zhang, W. Q.; Chen, L. D.; Li, Q.; Uher, C.; Day, T.; Snyder, G. J. Nat Mater **2012**, 11, 422.